LEABHARLANN CHOLÁISTE NA TRÍONÓIDE, BAILE ÁTHA CLIATH | TRINITY COLLEGE LIBRARY DUBLIN
Ollscoil Átha Cliath | The University of Dublin

Terms and Conditions of Use of Digitised Theses from Trinity College Library Dublin

Copyright statement

All material supplied by Trinity College Library is protected by copyright (under the Copyright and Related Rights Act, 2000 as amended) and other relevant Intellectual Property Rights. By accessing and using a Digitised Thesis from Trinity College Library you acknowledge that all Intellectual Property Rights in any Works supplied are the sole and exclusive property of the copyright and/or other IPR holder. Specific copyright holders may not be explicitly identified. Use of materials from other sources within a thesis should not be construed as a claim over them.

A non-exclusive, non-transferable licence is hereby granted to those using or reproducing, in whole or in part, the material for valid purposes, providing the copyright owners are acknowledged using the normal conventions. Where specific permission to use material is required, this is identified and such permission must be sought from the copyright holder or agency cited.

Liability statement

By using a Digitised Thesis, I accept that Trinity College Dublin bears no legal responsibility for the accuracy, legality or comprehensiveness of materials contained within the thesis, and that Trinity College Dublin accepts no liability for indirect, consequential, or incidental, damages or losses arising from use of the thesis for whatever reason. Information located in a thesis may be subject to specific use constraints, details of which may not be explicitly described. It is the responsibility of potential and actual users to be aware of such constraints and to abide by them. By making use of material from a digitised thesis, you accept these copyright and disclaimer provisions. Where it is brought to the attention of Trinity College Library that there may be a breach of copyright or other restraint, it is the policy to withdraw or take down access to a thesis while the issue is being resolved.

Access Agreement

By using a Digitised Thesis from Trinity College Library you are bound by the following Terms & Conditions. Please read them carefully.

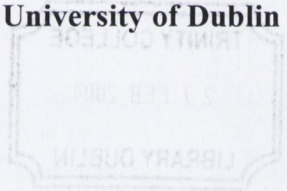
I have read and I understand the following statement: All material supplied via a Digitised Thesis from Trinity College Library is protected by copyright and other intellectual property rights, and duplication or sale of all or part of any of a thesis is not permitted, except that material may be duplicated by you for your research use or for educational purposes in electronic or print form providing the copyright owners are acknowledged using the normal conventions. You must obtain permission for any other use. Electronic or print copies may not be offered, whether for sale or otherwise to anyone. This copy has been supplied on the understanding that it is copyright material and that no quotation from the thesis may be published without proper acknowledgement.

Numerical Investigation of Self-Pulsation for Narrow Stripe AlGaAs/GaAs and InGaAsP/InP Semiconductor Laser Diodes

by

Canice G. O'Brien

A thesis submitted for the degree of
Doctor of Philosophy
in the University of Dublin



under the supervision of

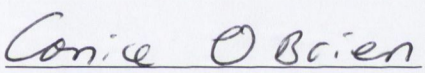
Prof. John Donegan
Department of Physics
Trinity College Dublin

October 2003

TRINITY COLLEGE
27 FEB 2004
LIBRARY DUBLIN
THESIS
7751

Declaration

This thesis has not been submitted as an exercise for a degree in this or any other university. The work described is entirely my own, with exception of assistance and the collaborative work mentioned in the acknowledgements. I agree that Trinity College Library may lend or copy this thesis upon request.



Canice G. O'Brien

Numerical Investigation of Self-Pulsation for Narrow Stripe AlGaAs/GaAs and InGaAsP/InP Semiconductor Laser Diodes

By Canice G. O'Brien October 2003

Summary

Self-pulsation in laser diodes is the process by which pulsed light is emitted from the laser while under direct current injection. As a result of their low relative intensity noise under feedback conditions, and high frequency pulsed emission, they are of great interest due to their current and potential future applications in telecommunications systems as well as optical data storage applications.

This thesis is primarily concerned with the theoretical investigation of the dynamics of these self-pulsating lasers emitting at 780nm in AlGaAs/GaAs and 1.55μm in InGaAsP/InP material systems. Both the spatial and temporal dynamics are studied using a method of solution of the Helmholtz equation based on the effective index method. The carrier transport in the active layer and current spreading cladding layers has been incorporated through the numerical sectioning of the lateral dimension of the device. A self-consistent method for the determination of lasing wavelength, material gain and spontaneous emission has been utilised to explain some of the key experimental findings. The fundamental limitations of the use of the effective index method for weakly guided waveguides are presented.

In response to these limitations, the development of a fully two-dimensional non-uniform finite difference technique requiring the solution of the resulting large sparse non-hermitian problem leads to an understanding of the role of self-focusing as an enhancement of the self-pulsation mechanism. Probable causes for the transition between self-pulsation into relaxation oscillations and continuous wave (CW) emission at high currents were also identified.

The insights gained at 780nm prompted the exploration of self-pulsation at the commercially important 1.55μm wavelength. Important effects in this wide bandgap material such as Auger recombination and intervalence band absorption presented new challenges in the laser design. With the incorporation of these effects into the laser model, the optical waveguide and active layer gain design could be optimised.

The first known theoretical evidence of self-pulsation at 1.55um was demonstrated for a single section, narrow stripe, complex refractive index guided structure, where the self-pulsation mechanism is based on saturable absorption, enhanced by self-focussing effects.

Acknowledgements

I would like to begin by expressing my gratitude to those people who have acted in a supervisory role over the course of my PhD. To Professor John Hegarty who accepted me into the group and for introducing me to Dr James O'Gorman, from whom the motivation for this research came initially. I would also like to thank Dr. Fred Logue for this advice and support and for introducing me to Aikido. But easily, the greatest workload fell on the shoulders of Professor John Donegan, after his inheritance of the group. Without his patience and encouragement this thesis would not have been possible. Without the initial correspondence with Professor Danny Sorensen Rice University, Austin, Texas and collaboration with Heidi Thornquist of Sandia National Laboratories Albaquerque, I would still be waiting for my programs to finish. Truly altruistic by nature, Heidi gave of here time and expertise without question and whom I owe a debt of gratitude.

I would like to thank Dr. Woon-Ho Seo for providing the gain and spontaneous emission data that is used within this thesis and, along with Dr Stephen Lynch, for providing fruitful discussions and proof reading this thesis. I am grateful to Dr Dewi Jones and Dr John Patchell for useful discussions over the years. I'd like to express my appreciation to all the past members of the group, especially John, Alan, Daire and Karl who provided light relief in the earlier days and of course the present lunchtime crew with whom I have celebrated college cuisine. They can be found beatin each other with sticks around a field, in the dark, underground, under water, in a particular pub, taking a disliking to wing mirrors, applying logic to everything. They have provided the key component to any successful group, humour. To the phenotype specialists, and Frank and Lar, who put up with the moaning and for not wanting to talk about physics. To Melanie whose kindness and friendship I will always be grateful. To the members of the Haverty road club who provided the most laughter over the four years Donal, Niall, Stan, Vinnie, Mick, Mary, Stan and Alex. To Marie, who is an inspiration and has helped me to begin to discover the important things in life.

Finally I would like to thank my parents Helen and Martin, for their love, support and belief in me, which has enabled me to come this far.

Table of Contents

1. Introduction 1

1.1 History of the self-pulsating laser 1
1.2 Suppression of feedback induced noise 3
1.3 Thesis Overview 5
References 7

2. Theoretical Background 10

2.1 Semiconductor Band Structure: Effective Mass Theory 10
2.1.1 Strain Effects on Band Structure 12
2.2 Optical Processes in Semiconductors 15
2.2.1 Density of States 16
2.2.2 Bernard-Duraffourg Inversion Condition 19
2.2.3 Spontaneous Emission 20
2.2.4 Intervalence Band Absorption 22
2.2.5 Differential Index 23
2.2.6 Burnstein-Moss Effect 23
2.2.7 Bandgap Renormalisation 24
2.2.8 Free-Carrier Absorption 24
2.3 Non-Radiative Processes 25
2.3.1 Defect and Surface Recombination 25
2.3.2 Auger Recombination 27
2.4 Carrier Recombination Rates 29
2.5 Double-Heterostructure Design 31
2.6 Optical Waveguiding 32
2.6.1 Scalar Wave Equation 32
2.6.2 Optical Confinement Factor and Modal Gain 34
2.6.3 Effective Index Method 36
2.7 One Dimensional Waveguide Analysis 37
2.7.1 Galerkin's Formalism in One Dimension 38
2.7.2 Sine series Basis Function 38
2.7.3 Hermite-Gauss Basis 41
2.74 Finite Difference Method 41
2.8 Two Dimensional Methods 44
2.8.1 Sine Series Expansion 44
2.8.2 Finite Difference Method 45
2.9 Conclusions 47
References 49

3. Self-Pulsation Dynamics 53
3.1 Introduction 53
3.2 Current Spreading 54
3.3 Ambipolar Diffusion 57
3.4 Threshold Current Determination 62
3.5 Self-Pulsation by Design 68
3.6 Self-Pulsation Dynamics 78
3.7 Conclusions 86
References 87

4. Two-Dimensional Self-Pulsation *89*
4.1 Introduction 89
4.2 The Advantages of Two-Dimensional Waveguiding 89
4.2.1 Use of the Inherent Symmetry of the Structure *90*
4.3 Numerical Solution of the Non-Hermitian Eigenvalue Problem 92
4.4 Eigenvalue and Eigenvector Computation 93
4.5 The Arnoldi Method 94
4.6 A Two-Dimensional Perspective 96
4.7 Temporal Dynamics 99
4.8 Spatial Dynamics 103
4.9 Self-Pulsation Variation with Current 107
References 114

5. Self-Pulsation at 1.55μm *116*
5.1 Motivation for Self-Pulsation at 1.55μm 116
5.2 Consideration Factors for 1.55μm Self-Pulsation Laser Design 118
5.2.1 Material Properties of the InGaAsP/InP system *118*
5.3 Optimisation of the Active Region 121
5.4 Optimisation of the Transverse Waveguide 122
5.5 Design Parameters for the Triple Quantum Well Active Region 127
5.5.1 Transverse Waveguiding *127*
5.6 Temporal and Spatial Dynamics 131
5.6.1 Consideration of Loss Mechanisms (IVBA and Auger Recombination) *131*
5.7 Validity of the Effective Index Method 132
5.8 Results and discussion 135
References 139

6. Conclusions *143*
6.1 General Overview 143
6.2. Future Work 146
References 149

Chapter 1 Introduction

1.1 History of the self-pulsating laser

Self-pulsating lasers are of great interest due to their potential applications in telecommunications systems as well as optical data storage applications. They have been studied since the diode lasers became available in the 1960's [1]. The first semiconductor lasers exhibited self-pulsation behaviour, although they were designed to operate in constant wave mode. The generation of pulsations in the light intensity was regarded as detrimental to the development of semiconductor injection lasers. It was found that devices containing large defect densities as a result of poor quality materials or degraded devices, exhibited self-pulsation. The self-pulsation mechanism was later attributed to saturable absorption, where these dark-line defects acted as absorption centres within the laser [2]. The advances in the technology of material growth and fabrication in subsequent years, led to great improvements in material and device quality. The absence of dark-line defects within the laser diode prompted Joyce and Dixon in 1979 [3] to develop a new model for the explanation of the origins of self-pulsation. Their model relied upon the idea of saturable absorber Q-switching, where the saturable absorbers were considered to be located near the ends of the laser in regions where it was believed the injected carrier density was reduced due to surface recombination. From the modelling perspective, the device active region was divided into an "end" region, close to the facets and a "bulk" region with a separate carrier density rate equation in each. Perhaps the most important conclusion from their calculations and one that formed the basis of later models was that the larger differential peak absorption compared to that of the differential peak gain was necessary to achieve pulsations. With the discovery that self-pulsating lasers had low relative intensity noise (RIN) behaviour under optical feedback conditions there was a shift towards designing lasers that would exhibit stable self-pulsation for the use in optical disk systems [4].

The first evidence of the effect of self-focussing contributing to the self-pulsation effect, was given in [5] where Chinone et al. have shown that the deformation of the lateral mode in lasers without built-in mode confinement greatly enhances the

amplitude of relaxation oscillations indicating a reduction in the damping of the solutions of the carrier and photon rate equations. Following on from this Lang [6] theoretically predicted the enhancement of the pulsation phenomena by self-focussing. The effect of self-focussing was shown experimentally by Van der Ziel [7], when the decrease of the full with at half intensity (FWHM) with the emission of a pulse was measured. Between this period and 1995 the carrier and time dependent waveguide modifications were largely ignored in favour of an understanding based on saturable absorption alone. It was, perhaps, the success of the two section models of Yamada [8] and others in predicting the broad temporal features of the self-pulsation behaviour that hampered the understanding of the quantitative temporal and spatial behaviour. The move from a two-section model to one in which the spatial and temporal carrier density profiles across the lateral dimension of the active region could be determined was first carried out by Buss [9]. Using a similar model Takayama et al. [10] showed that based on the results of the model, important parameters such as the active layer thickness and choice of blocking layer material and its influence on the static optical field helped tremendously in the design of lasers with lower threshold values and a wide operating current range. Through the development of a time varying two-dimensional model, the same group showed that their earlier assumptions that the optical field was invariant in time and that self-pulsation was a result of the saturable absorption effect meant that a quantitative description of the self-pulsation mechanism was not possible.

During this time, advances had been made in the application of self-pulsation at 650nm for use in the digital versatile disc (DVD) systems. Recently 780nm band and 650nm-band self-pulsation lasers have been monolithically integrated for the first time [11]. Very high frequency self-pulsation has been achieved based on a mechanism of beating between modes in a distributive feedback laser (DFB) with reported self-pulsation frequencies of 80 GHz [12]. Other mechanisms have been suggested to explain the appearance of self-pulsation in DFB lasers without saturable absorbers. It has been proposed by Duan et al. [13] that the optical grating introduces a structure-dependent differential gain. When the differential gain becomes negative positive feedback occurs, which leads to self-pulsation within the device. The first instance of self-pulsation in vertical cavity surface emitting lasers (VCSEL) as a result of a saturable absorption was demonstrated in [14]. It has also been possible to control

the self-pulsation mechanism in VCSEL through the incorporation a voltage controlled quantum well saturable absorber [15].

1.2 Suppression of feedback induced noise

Reduction of the feedback-induced noise in semiconductor lasers is an important subject for the application of this device as a source for optical disc and optical fibre systems.

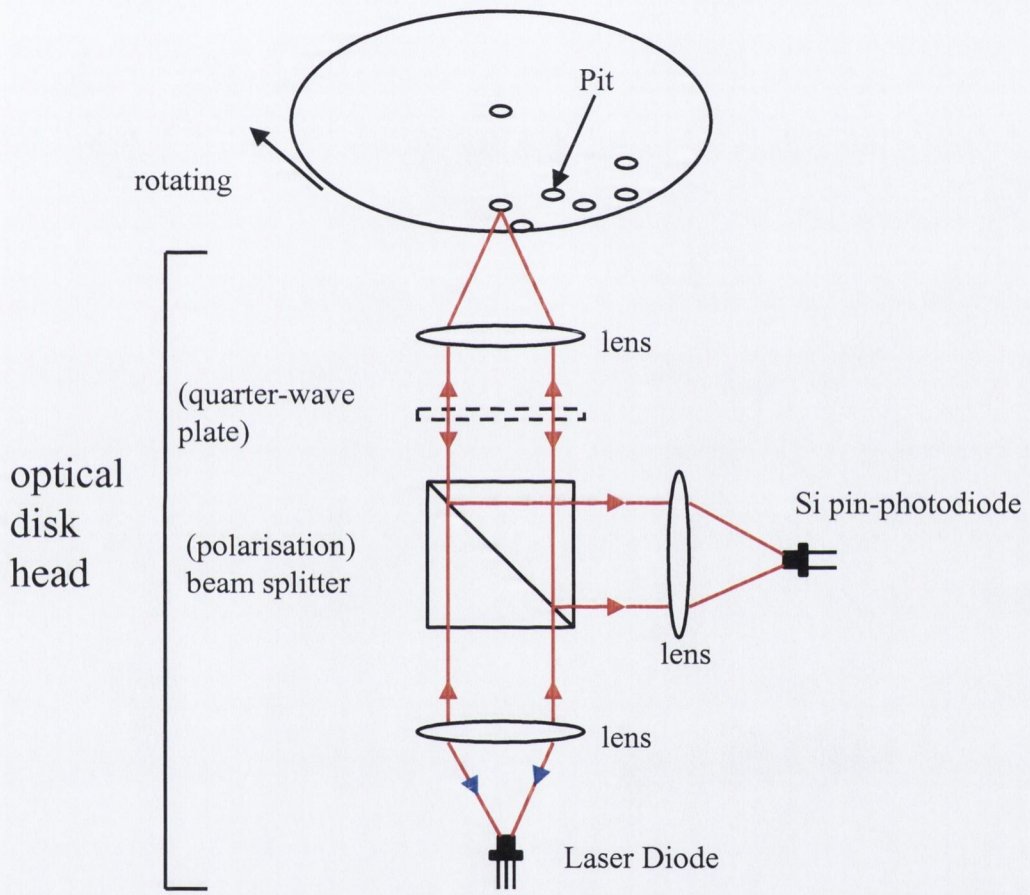


Figure 1-1 Diagram of the optical disk head system employed in standard compact disc laser. The use of superposition circuitry or the quarter wave plate and polarisation beam splitter may be used if the laser does not self-pulsate.

An illustration of the optical disk head for the use in compact disc systems is shown in figure1-1. The 780nm light from the AlGaAs/GaAs laser diode is collimated by a lens and is focused to a diameter of approximately 1μm onto the disc. The reflected light arrives at the photodiode after reflection from the beam splitter. The electrical signal emitted from the photodiode is dependent on whether the light was incident on a pit

on the disc or not. The use of the quarter wave plate and polarisation beam splitter shown in brackets in the figure is one method of reducing the amount of feedback entering the diode laser, shown here by the blue arrows. The need for mass production of laser diodes at low cost means that the inclusion of quarter wave plates with polarising beam splitters or high frequency superposition circuitry is an expensive method of reducing the effects of feedback noise on the laser. Laser diodes under feedback contain quantum shot noise, longitudinal mode-hopping noise, mode partition noise, and optical feedback noise. The advantage that self-pulsating laser diodes offer, is that the mode hopping noise and optical feedback noise can, in the main, be effectively suppressed. As has been mentioned earlier, a high frequency modulation can be applied to a laser diode biased around threshold, resulting in the pulsed emission at the driving frequency with multi-longitudinal mode oscillation. It was found for the case of driving current modulated pulsation [16] that some modes oscillated more strongly when they are subject to optical feedback. This suggests that mode competition noise is induced by optical feedback. Modulation frequencies in excess of 600MHz were required for sufficient noise reduction. It was also found that the number of longitudinal modes increased significantly above this modulation frequency. Therefore broad multi-longitudinal mode pulsation reduces mode competition noise and also reduces the coherence length of the laser.

Theoretical analysis based on mode competition theory of the noise reduction effect of self-pulsation was given by Yamada [17]. Two different types of mode competition phenomena were represented as the noise generating mechanisms with different effects on the noise spectra. One is the competition among the internal cavity modes (intrinsic modes of the solitary laser), where the noise spectrum gives a Lorentzian shape, which is enhanced in the lower frequency (several MHz) region of the spectrum. Excess noise due to mode competition among internal cavity modes is well suppressed by the self-sustained pulsation. Another type of phenomenon is the competition among external cavity modes, which occurs in the presence of optical feedback. The noise spectrum is flat over a wide frequency regime. This type of excess noise is mostly suppressed by self-pulsation but remains under some operating conditions. An example of the effect that competition among external cavity modes can have is shown in figure 1-2. As described in [18] and similarly in [19], when the feedback distance l is small enough, the pulsation frequency is almost equal to or

lower than the solitary laser pulsation frequency f_{po} without optical feedback. When the feedback distance becomes longer the pulsation frequencies are pulled to or locked into the frequency separation given by the external cavity modes $c/2l$. The method of the locking effect is illustrated in figure 1-2. Here $1/f_{po}$ is the period of the pulsation without optical feedback. The delay time of the feedback optical pulse is represented by $2l/c$. This effect is similar to the mode locking effect by an external cavity. Since the timing of the pulse generation is shortened, the phase relationship between the photon and carrier variations will be modified.

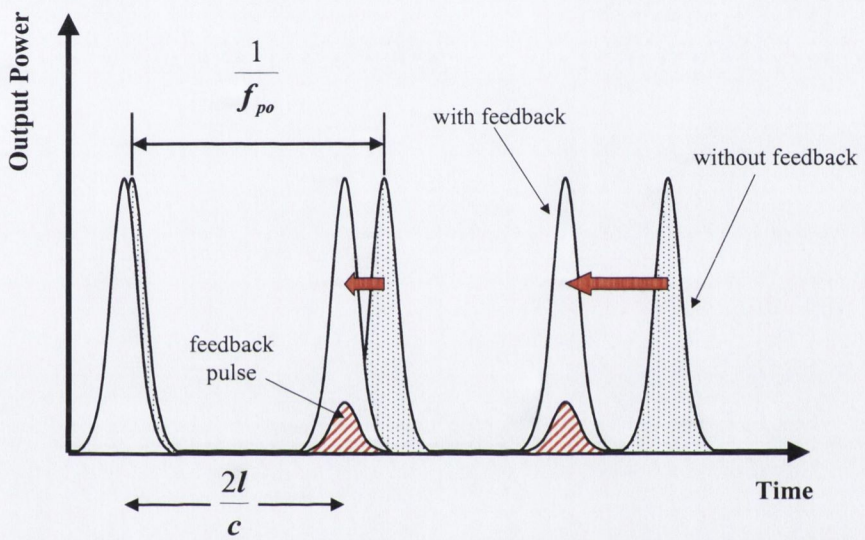


Figure 1-2 Illustration of the mechanism of the pulling of the pulsation frequency into the external cavity mode

1.3 Thesis Overview

Chapter 2, presents much of the most relevant background physics upon which the work in the subsequent chapters is based. The main topics covered include semiconductor band structure, optical processes in semiconductors, non-radiative processes, double-heterostructure design and optical waveguiding. A discussion of the various numerical techniques that have been used in the solution of the two-dimension wave equation is subsequently presented.

In Chapter 3, the self-pulsation laser model is outlined, concentrating on the key areas of current spreading, ambipolar diffusion and the threshold current determination.

Based on the outlined model the important factors that need to be considered in the design of an AlGaAs/GaAs diode operating at 780nm are outlined. A description of the self-pulsation dynamics in which the optical field is solved using the effective index approximation completes the chapter.

In Chapter 4, the advantage of the use of a two-dimensional solution of the wave equation illustrates some of the shortcomings of the use of the effective index methods for weakly guided structures. In order to achieve the solution of the two-dimensional system, the numerical solution of the non-hermitian eigenvalue problem is presented. Based on the use of the implicitly restarted Arnoldi method, the two dimensional field profiles are detailed. The possibility of performing simulations far in excess of the threshold current is made possible. Some conclusions are drawn as to the possible factors that lead to the termination of the self-pulsation process at high currents.

Chapter 5, details the motivation for the achievement of a self-pulsating laser diode at a wavelength of 1.55μm. The important processes, such as Auger recombination, that are specific to wide bandgap materials are incorporated into the model. The design of a new type of laser requires the optimisation of key parameters. The optimisation of the active layer gain material and the design of the waveguiding aspects of the laser are presented here. The temporal and spatial dynamics of the model show the advantage of the device optimisation and the steps that can be taken for future improvements.

The key results of the previous chapters are presented in chapter 6. Possible directions that could be taken in future work, including the approach to the realisation of a 1.55μm laser are proposed.

References

1 "Dynamics of injection lasers", N. G. Basov, IEEE J. Quant. Electron. **4,** p 855, 1968.

2 "Degradation of CW GaAs double heterojunction lasers at 300K", B. C. DeLoach, B. W. Hakki, R.L. Hartman, and L. D'Asaro, Proc. IEEE. **61,** p1042, 1973.

3 "A Possible Model for Sustained Oscillations (Pulsations) in (Al,Ga)As Double-Heterostructure Lasers", R. W. Dixon, and W. B. Joyce, IEEE J. Quant. Electron. **15,** (6), 1979.

4 "Suppression of feedback-induced noise in short-cavity V-channeled substrate inner stripe lasers with self-oscillation", S. Matsui, H. Takiguchi, H. Hayashi, S. Yamamoto, S.Yano, and T. Hijikata, Appl. Phys. Lett. **43,** (3), p 219, 1983.

5 "Effects of lateral mode and carrier density profile on dynamic behaviour of semiconductor lasers", N. Chinone, K. Aiki, M. Nakamura, R. Ito, IEEE J. Quant. Electron. **14,** p 625, 1978.

6 "Intensity pulsation enhancement by self-focussing in semiconductor Lasers", R. Lang, Jpn. J. Appl. Phys. **19,** p 93, 1980.

7 "Self-Focussing Effects in Pulsating $Al_xGa_{1-x}As$ Double-Heterostructure Lasers", J. P. Van Der Ziel, IEEE J. Quant. Electron. **17,** (1), 1981.

8 "A Theoretical Analysis of Self-Sustained Pulsation Phenomena in Narrow-Stripe Semiconductor Laser", M. Yamada, IEEE J. Quant. Electron. **29,** (5), 1993.

9 "Models of the Static and Dynamic Behaviour of Stripe Geometry Lasers", J. Buus, IEEE J. Quantum Electron, **19,** (6), p 953, 1983.

10 "Low-Noise and High Power GaAlAs Laser Diodes with a New Real Refractive Index Guided Structure", T. Takayama, O. Imafuji, H. Sugiura, M. Yuri, H. Naito, M. Kume and K. Itoh, Jpn. J. Appl. Phys. **34,** p 3533, 1995.

11 "Monolihically Integrated Dual-Wavelength Self-Sustained Pulsation Laser Diodes with Real Refractive Index Guided Self-Aligned Structure", T Onishi, O Imafuji, T. Fukuhisa, A. Mochida, Y. kabayashi, M Yuri, K Itoh, and H Shimizu, Jpn. J. Appl. Phys. **40,** p 6401, 2001.

12 "Detuned Grating Multisection-RW-DFB Lasers for High-Speed Optical Signal Processing", M Mohrle, B Sartorius, C Bornholdt, S Bauer, O Brox, A Sigmund, R Steingruber, M Radziunas and H-J Wunsche, IEEE J. Select. Topics in Quantum Electron. **7,** (2), 2001.

13 "Self-Pulsation in Multielectrode Distributed Feedback Lasers", G. H. Duan, and P. Landais, IEEE Photon. Tech. Lett. **7,** (3), p1041, 1995.

14 "Observation of bistability in GaAs quantum-well vertical cavity surface-emitting lasers", X. Tang, J. P. Van der Ziel, B. Chang, R. Johnson, J. A. Tatum, E. Jonsson, IEEE Quant. Electron. **33,** (6), p 2003, 1997.

15 "Self-Pulsating VCSEL with controllable quantum-well saturable absorber", S. F. Lim, J. A. Hudgings, G. S. Li, W. Yuen, K. Y. Lau, C. J. Chang-Hasnain, IEEE LEOS p 19, 1997.

16 "Optimum conditions for the high frequency noise reduction method in optical videodisc players", A. Arimoto, M. Ojima, N. Chinone, A. Oishi, T. Gotoh, and N. Ohnuki, Appl. Opt. **25,** (9), p1398, 1986

17 "Theoretical analysis of noise-reduction effect in semiconductor lasers with help of self-sustained pulsation phenomena", M. Yamada, J. Appl. Phys. **79,** (1), p 61 1996.

18 "Experimental Characterization of the Feedback Induced Noise in Self-Pulsating Lasers", M. Yamada, Y Ishikawa, S. Yamamura, M Kidu, A. Kanamori, and Y Aoki, IEICE. Trans. Electron. **E82-c**, (12), p2241 1999.

19 "Theoretical investigations of electro-optical synchronisation of self-pulsating laser diodes", A. Egan, P. Rees, J. O'Gorman, M. Harley-Stead, G. Farrell, J. Hegarty, and P. Phelan, IEEE Proc. Optoelectron. **143,** (1), p 31 1996.

Chapter 2 Theoretical Background

This chapter is intended to provide a review of the basic concepts in laser theory upon which much of the work in the subsequent chapters is based. We begin with an introduction to semiconductor band structure and the effect of strain on the band structure. Following on from this, the various radiative and non-radiative processes that become important in later chapters are discussed. The chapter concludes with an outline of optical waveguide theory specific to self-pulsation laser design, and a description of the various numerical approaches to the solution of the two-dimensional wave equation is given.

2.1 Semiconductor Band Structure: Effective Mass Theory

In order to understand the optical properties of semiconductors, such as absorption or gain due to electronic transitions in the presence of an incident optical wave, the electronic bandstructure must be known. For optical devices we are only interested in direct band gap semiconductors in which the conduction band minima lies directly above the valence band maximum in k space. In the indirect band gap case, phonon emission is required in order to conserve momentum and therefore the transition probability is reduced considerably. The general band structure theory follows from the Bloch theorem [1], the eigenstates ψ of the one-electron Hamiltonian $H = -\frac{\hbar^2 \nabla^2}{2m} + U(r)$, where $U(r+R) = U(r)$ for all Bravais lattice vectors R in the Bravais lattice, can be chosen to have the form of a plane wave times the periodicity of the Bravais lattice:

$$\psi_{nk}(r) = e^{ik.r} u_{nk}(r) \tag{2.1}$$

A full description of the band structure requires numerical methods for its solution. The k.p method was introduced by Bardeen [2] and Seitz [3] and it is a useful technique for analysing the band structure close to the extremum at the Brillouin zone centre. The band structure and gain calculations were provided by Dr Woon-Ho Seo. We will briefly describe the Luttinger-Kohn model [4], which accounts for the spin-orbit interaction and the degeneracy of the bands. It is useful within this method to

apply Löwdin's renormalisation method [5], which is a technique used within perturbation theory in which the eigenfunctions and eigenenergies are divided into class A and class B. This treatment is based on the idea that we are mainly interested in the states in class A, and the influence of the states in class B, are treated as a perturbation. As shown in figure 2-1 the six valence bands are treated as class A and the rest of the bands are treated as class B.

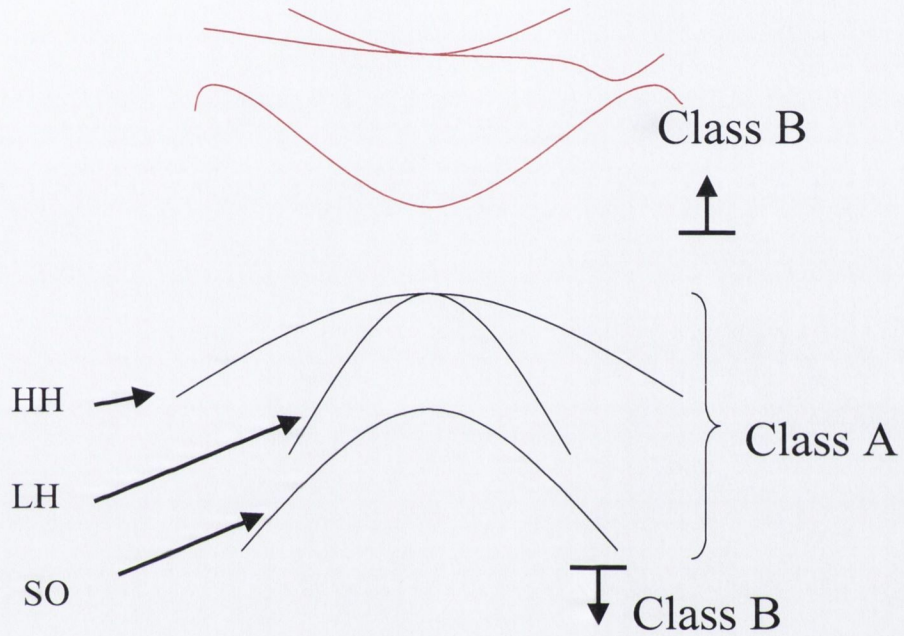


Figure 2-1 Illustration of Löwdin's method applied to Luttinger-Kohn's model. The doubly degenerate heavy-hole (HH), light-hole (LH) and spin-split-off (SO) bands are treated as class A All other bands are labelled as class B.

Using the Schrödinger equation for the Bloch function the following equation is solved using Löwdin's perturbation,

$$\left\{\frac{p^2}{2m}+V(r)+\frac{\hbar}{4m^2c^2}[\nabla V\times p]\bullet\sigma\right\}\psi_{nk}(r)=E_n(k)\psi_{nk}(r) \qquad (2.2)$$

in which the third term accounts for the spin-orbit interaction, and σ is the Pauli spin matrix. The result requires the solution of an eigenequation

$$\sum_{j=1}^{6} H_{ij}^{LK} a_j(k) = E a_j(k) \tag{2.3}$$

where H^{LK} denotes the Luttinger-Kohn Hamiltonian. Applying the effective mass theory for a perturbation potential $U(r)$, such as a quantum well potential, for degenerate bands, the solution $\psi(r)$ in the presence of the perturbation, is given by

$$\psi(r) = \sum_{j=1}^{6} F_j(r) u_{jo}(r) \tag{2.4}$$

where $F_j(r)$ satisfies,

$$\sum_{j=1}^{6} \left[E_i(0)\delta_{ij} + \sum_{\alpha,\beta} D_{ij}^{\alpha\beta} \left(-i\frac{\delta}{\delta x_\alpha} \right) \left(-i\frac{\delta}{\delta x_\beta} \right) + U(r)\delta_{ij} \right] F_j(r) = E F_j(r) \tag{2.5}$$

The details of which can be found in [6]. An important conclusion of the effective mass theory is that the periodic potential $V(r)$ determines the energy bands, but the effective mass, and the effective mass equation (2.5), contains only the extra perturbation potential $U(r)$.

2.1.1 Strain Effects on Band Structure

The use of strained superlattices has been of great interest since the early 1980s. It was suggested by Yablanovitch and Kane [7][8], and independently by Adams [9], that the introduction of compressive strain into the semiconductor crystal lattice, could enhance the operating performance of the semiconductor laser diode. Through the introduction of strain it has been possible to vary the band gap, lattice constant, and the perpendicular transport effective mass, using ternary strained layer superlattices. Application of strained layer quantum well lasers has been shown to exhibit superior performance compared to their lattice-matched counterpart and this will be discussed in chapter 6. Pikus and Bir [10][11] provided the fundamental theory necessary to describe how lattice deformations affect the Hamiltonian, which describes the interaction between the heavy-hole (HH), light –hole (LH), and split-off (SO) bands. Since the typical values for the thickness of quantum wells are below 20nm, it is possible to grow them in a state of strain without the formation of

structural defects, which only occur after a critical value of the strain and layer-thickness has been reached. If this epi-layer has a lattice constant greater than the surrounding lattice, then the epi-layer will undergo compressive strain in the plane perpendicular to the growth direction and will elongate in the growth direction in an attempt to maintain cell volume (Figure 2-2(a)). If the epi-layer to be introduced has a smaller lattice constant than the surrounding lattice, then the epi-layer will undergo tensile strain in the direction perpendicular to the growth direction and will shrink in the growth direction (Figure 2-2(b)).

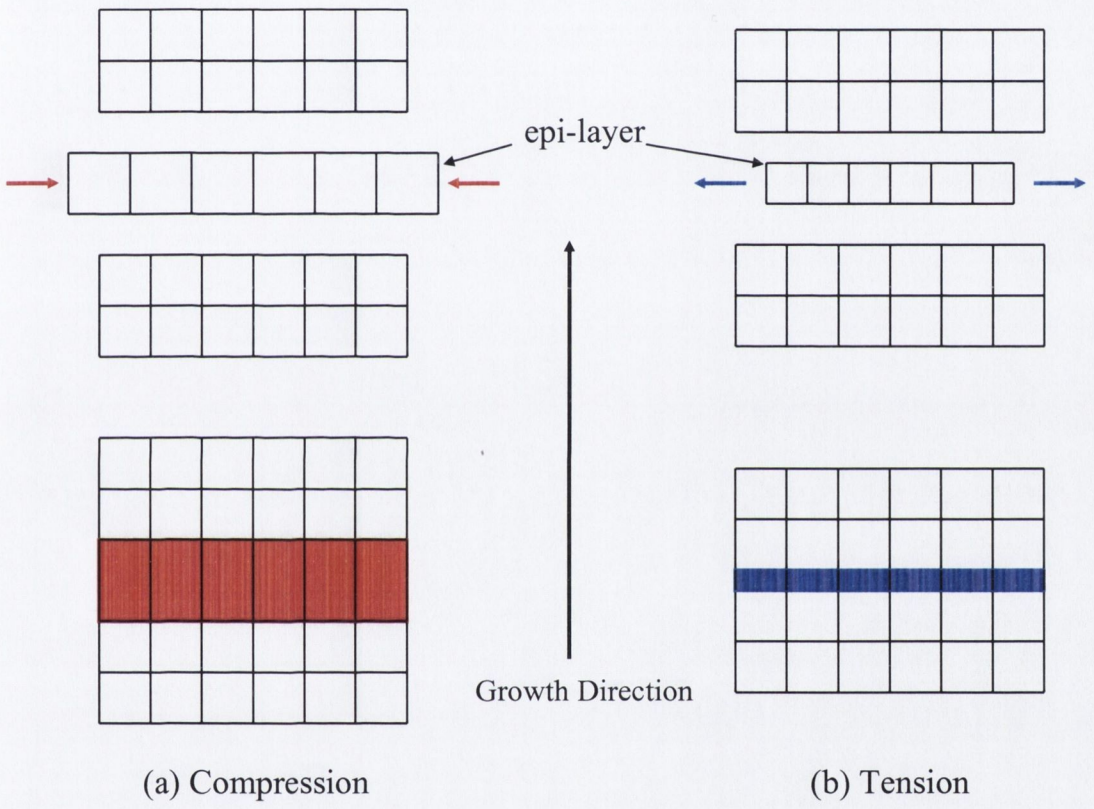


Figure 2-2 (a) Introduction of an epi-layer whose lattice constant is larger than the surrounding layers, which results in compressive strain perpendicular to the growth direction (red arrows). (b) The epi-layer lattice constant is less than the surrounding layers resulting in tensile strain in the direction perpendicular to the growth direction (blue arrows)

Since there is a direct relationship between the energy gap and the lattice spacing, distortions in the crystal lattice will lead to alterations in the bandgap of the strained layer. As can be seen from figure 2-3 there are two main modifications that occur. The first effect is an upward shift in the conduction band as well as a downward shift

in both valence bands, increasing the overall bandgap by δE_{hy}, which is positive for compressive strain and negative for tensile strain. The hy subscript indicates that the shift is a result of the hydrostatic component of the strain. The second effect is that the HH and LH bands are each pushed in opposite directions from the centre by an amount $\zeta = \frac{1}{2}\delta E_{sh}$. Where the sh subscript denotes the shear component of the strain. The band degeneracy of the two valence bands is removed. If we consider the example shown in figure 2-3 for the case of a bulk GaxIn1-xAs material, in the case of biaxial compressive, where the Ga mole fraction x in GaxIn1-xAs is < 0.468, the heavy hole band is above the light hole band and its effective mass is lighter than the light-hole band in the transverse plane (the kx or ky) direction. In the tensile strained case where x > 0.468, the light-hole band shifts above the heavy-hole band. Figure 2-3 is taken from [12] where kz represents the growth direction.

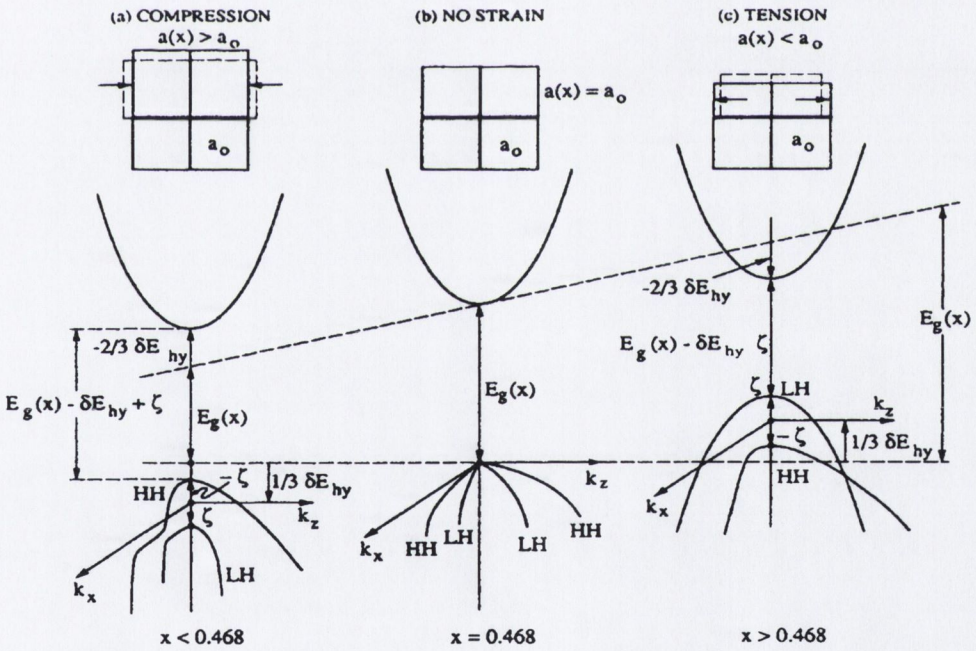


Figure 2-3 The energy band structure in momentum space for a bulk GaxIn1-xAs material under (a) biaxial compressive, (b) lattice matched, (c) biaxial tension for the different Ga fraction x.

One of salient features of figure 2-3 is that under strain, the effective mass is reduced in the direction parallel to the growth interfaces which decreases the density of states function and hence the lasing threshold current of the laser.

2.2 Optical Processes in Semiconductors

In order to gain an understanding of the optical transitions; absorption, spontaneous and stimulated emission in semiconductors we must first consider the interactions between photons and electrons. The optical waves interaction with the electron enters the Schrödinger equation through the vector potential A where the new Hamiltonian can be expressed as

$$H = H_0 + H' \tag{2.6}$$

where, H_0 is the unperturbed Hamiltonian

$$H_0 = \frac{P^2}{2m_0} + V(r) \tag{2.7}$$

and H'

$$H' = -\frac{e}{m_0} A \cdot P \tag{2.8}$$

can be treated as perturbation due to the presence of the optical field. Through the treatment of this term using time dependent perturbation theory [13], the rate of transition of an electron from an initial state i with energy E_i to a final state f with energy E_f is given by Fermi's golden rule

$$W_{i\to f} = \frac{2\pi}{\hbar}\left|H'_{fi}\right|^2 \delta\left(E_f - E_i - \hbar\omega\right) + \frac{2\pi}{\hbar}\left|H'_{fi}\right|^2 \delta\left(E_f - E_i + \hbar\omega\right) \tag{2.9}$$

where

$$\begin{aligned} H'_{fi} \equiv \langle f|H'(r)|i\rangle &= \int \psi_f^*(r) H'(r) \psi_i(r) d^3r \\ &= -\frac{e}{m_0} A \cdot \langle f|p|i\rangle = -\frac{eA}{2m_0} \hat{e} \cdot p_{fi} \end{aligned} \tag{2.10}$$

represents the overlap of the initial and final state wavefunctions. In order to calculate the net upward transition rate per unit volume in the crystal, R

$$R = R_{i\to f} - R_{f\to i} \tag{2.11}$$

we must take account of the probability that the state i is occupied and that state f is empty. Even the shortest recombination times are much longer than the time taken at

room temperature for the electrons in the conduction band, or the holes in the valence band to reach thermal equilibrium (10^{-12}s). Thus the orbital occupancy distribution of electrons and holes are very close to equilibrium Fermi-Dirac distributions in each band separately. The probability that the initial state i is occupied is given by

$$f_i = \frac{1}{1+e^{(E_i - E_{Fi})/k_B T}} \tag{2.12}$$

where E_{Fi} denotes the i^{th} quasi-Fermi level. Combining this with the even property of the delta function $\delta(-x) = \delta(x)$ and accounting for both spin orientations, we obtain

$$R = \frac{2}{V}\sum_{k_i}\sum_{k}\frac{2\pi}{\hbar}\left|\hat{e}\cdot p_{fi}\right|^2 \delta\left(E_f - E_i - \hbar\omega\right)\left(f_i - f_f\right) \tag{2.13}$$

Within Fermi's Golden Rule lies the assumption that the electron initially occupies a single state, which makes a transition to one of a large number of final states. Within a semiconductor both the final and the initial states are immersed within an energy band, therefore it is necessary to determine the density of transition pairs per unit energy, called the reduced density of states.

2.2.1 Density of States

In order that we can determine the number of states that lie within the energy range between E and E+dE or in k space between k and k+dk we must first develop a method for counting the states. As we can see from the second column in figure 2-4 for the bulk case, the three-dimensional vector k_{xyz} sweeps out a sphere of radius k in k space. In order to determine the number of states contained within the m-dimensional volume, we simply divide the volume in k space by the volume of one state, giving,

$$N_s = \frac{V_k}{(2\pi/L)^m} \tag{2.14}$$

where m = 2, 3 for 2D and 3D respectively. Therefore the m dimensional density of states function $\rho^{mD}(k)$ is described as

$$\int_{v_k} \rho^{mD}(k)dk = \frac{N_s}{V} \tag{2.15}$$

Solving for $\rho^{mD}(k)$ and applying equation (2.14), we obtain

$$\rho^{MD}(k) \equiv \frac{1}{V}\frac{dN_s}{dk} = \frac{(L)^m}{V}\frac{1}{(2\pi)^m}\frac{dV}{dk} \tag{2.16}$$

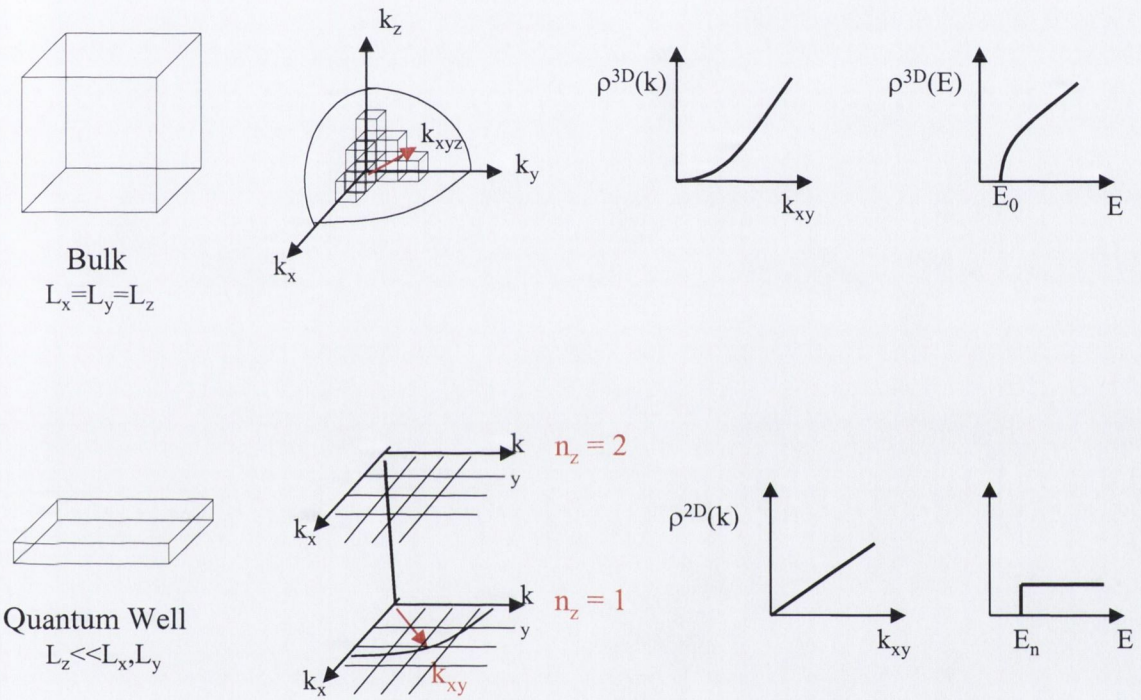


Figure 2-4 Comparison between the bulk and quantum well density of states. The second column illustrates the distribution of k vector states in k space where the grid represents a unit cell. The third and fourth columns show the density of states function as a function of k vector and energy respectively.

Often we are more interested in the density of states in energy space, the simple transformation is given by

$$\rho(E)dE = \rho(k)dk \quad \rightarrow \quad \rho(E) = \frac{\rho(k)}{dE/dk} \tag{2.17}$$

Thus the density of states can be for the bulk and quantum well structures can be expressed as

$$\rho^{3D}(E) = \frac{1}{4\pi^2}\left(\frac{2m}{\hbar^2}\right)^{\frac{3}{2}}\sqrt{E} \tag{2.18}$$

and

$$\rho^{2D}(E) = \frac{1}{L_z}\sum_{n_z}\frac{m^*}{\pi\hbar^2}H(E - E_{nz}) \tag{2.19}$$

where $H(x)$ is the Heaviside unit step function, which has the property that H(x) = 1 for x > 0, and 0 for x < 0. Due to the strict k-selection rule only states with identical k vectors can form transition pairs. As a result, the number of transition pairs is equal to the number of states in either the conduction or valence band $\rho_r dE_{fi} = \rho_c dE_f = \rho_v dE_i$ and since $dE_{fi} = dE_f + dE_i$ we obtain an equation for the reduced density of states in terms of the conduction and valence band density of states.

$$\frac{1}{\rho_r} = \frac{1}{\rho_c} + \frac{1}{\rho_v} \tag{2.20}$$

Expressing equation (2.13) in terms of the reduced density of states and describing the absorption coefficient within the crystal as the fraction of photons absorbed per unit distance

$$g(\hbar\omega) = \frac{R}{S/(\hbar\omega)} = C_0(\hat{e}\cdot p_{cv})^2 \int_0^\infty dE\,\rho_r(E)\frac{\Gamma/(2\pi)}{(E_g + E - \hbar\omega)^2 + (\Gamma/2)^2} \times\left[f_c(E) - f_v(E)\right] \tag{2.21}$$

and $C_0 = \dfrac{\pi e^2}{n_r c\varepsilon_0 m_0^2 \omega}$. Here we have replaced the delta function in equation (2.13) by a Lorentzian function of linewidth Γ where $\Gamma/(2\pi) = \dfrac{\hbar}{\tau_{in}}$. The intraband relaxation time, τ_{in}, is the time constant associated with the assumed exponential decay of the electrons after scattering to new states within the band. The Fourier energy spectrum required to construct an exponential time dependent state has a Lorentzian lineshape. Hence the energy state of each transition is no longer sharp but has an energy spread

over a range $\Delta E \approx \frac{\hbar}{\tau_{in}} \approx 7meV$ for a scattering time of 0.1ps. More sophisticated theoretical methods of determining the lineshape function can be found in [14][15][16][17].

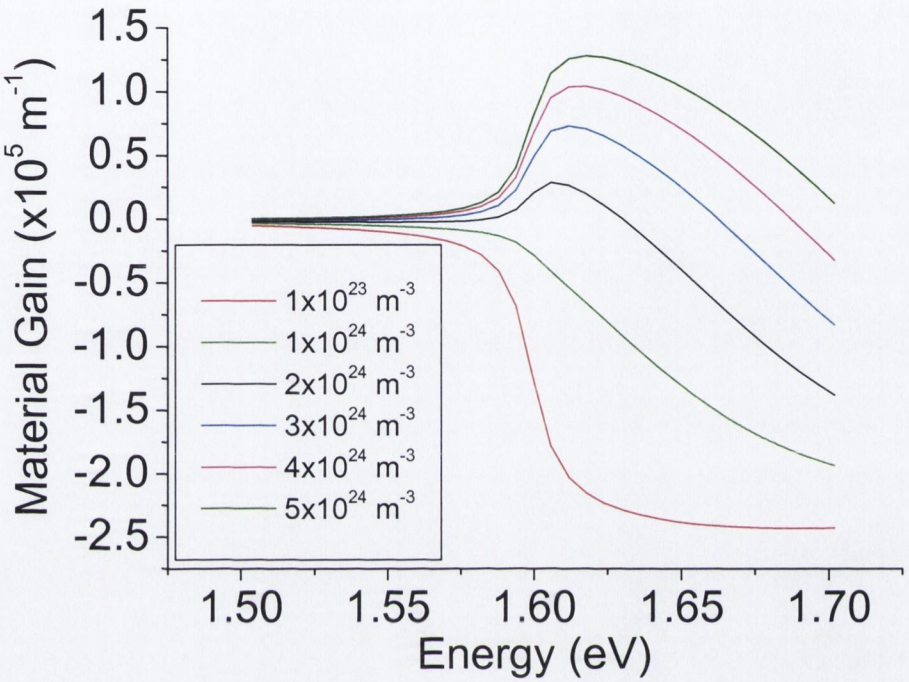


Figure 2-5 Calculated material gain at a temperature of 300K for an $Al_{0.14}Ga_{0.86}As$ material active layer of thickness 0.06μm.

The transparency carrier density for the bulk layer material gain shown in figure 2-5 has a value of $1.8x10^{24}m^{-3}$. The increase in energy value of the peak gain with increasing carrier density value can be attributed to the increase in the Fermi-level separation as a result of Fermi-Dirac statistics, this effect will be discussed in section 2.2.6.

2.2.2 Bernard-Duraffourg Inversion Condition

From equation (2.21) it is clear that a population inversion and gain will be achieved for $f_c(E) - f_v(E) > 0$. Since

$$f_c(E) - f_v(E) = \frac{e^{(E_v - F_v)/k_B T} - e^{(E_c - F_c)/k_B T}}{\left(1 + e^{(E_c - F_c)/k_B T}\right)\left(1 + e^{(E_v - F_v)/k_B T}\right)} > 0 \qquad (2.22)$$

Which requires that $e^{(E_v-F_v)/k_BT} > e^{(E_c-F_c)/k_BT}$ or

$$F_c - F_v > E_c - E_v = \hbar\omega \tag{2.23}$$

This is referred to as the Bernard-Duraffourg inversion condition [18]. The term population inversion requires $f_c - f_v > 0$ and not $\rho_c f_c - \rho_v f_v > 0$ as the name might imply. As we can see from equation (2.23) it is the magnitude of the relative difference between and not the absolute positions of F_c and F_v that determines the gain.

2.2.3 Spontaneous Emission

Unlike the case of stimulated emission, the spontaneous emission rate is not dependent on the number of photons within the cavity since although the upward transition is proportional to $\langle n_{ph} \rangle \hbar\omega$ where $\langle n_{ph} \rangle$ is the expected number of photons in the given optical mode; the downward transition is proportional to $(\langle n_{ph} \rangle + 1)\hbar\omega$ [19]. Therefore without any photons in the optical mode a finite downward transition rate exists. This point is central to the origin of the radiative spontaneous emission, since the occupation of the optical mode is no longer a requirement for spontaneous emission, the electron will interact with all optical modes in the energy range near $\hbar\omega$. It is therefore necessary to calculate the density of optical modes within a given energy range $\rho_{opt}(\hbar\omega)$. If we consider a cube of volume L^3 and by applying the periodic boundary conditions such that

$$k_x = l\frac{2\pi}{L}, \quad k_y = m\frac{2\pi}{L}, \quad k_z = n\frac{2\pi}{L} \tag{2.24}$$

and integrating the number of states with a differential volume in k space $d^3k / (2\pi / L^3) = k^2 dk d\Omega / (2\pi / L^3)$ where $d\Omega$ denotes the differential solid angle.

$$N(\hbar\omega) = 2\int \frac{k^2 dk d\Omega}{(2\pi)^3} \delta(\hbar\omega) = \frac{8\pi n_r^3 (\hbar\omega)^2}{h^3 c^2} \tag{2.25}$$

Incorporating the optical density of states (2.25), Fermi's golden rule (2.9) and the probability that an electron is occupied within the conduction band and a hole is unoccupied, for a photon energy $\hbar\omega$, giving, $f_c(1-f_v)$ we obtain

$$r^{spon}(\hbar\omega) = \left(\frac{8\pi n_r^2 E^2}{h^3 c^2}\right) C_0 \frac{2}{L_z} (\hat{e}\cdot p_{cv})^2 \int_0^\infty dE \rho_r(E) \times \frac{\Gamma/(2\pi)}{(E_g + E - \hbar\omega)^2 + (\Gamma/2)^2} \left[f_c(E)(1-f_v(E))\right] \tag{2.26}$$

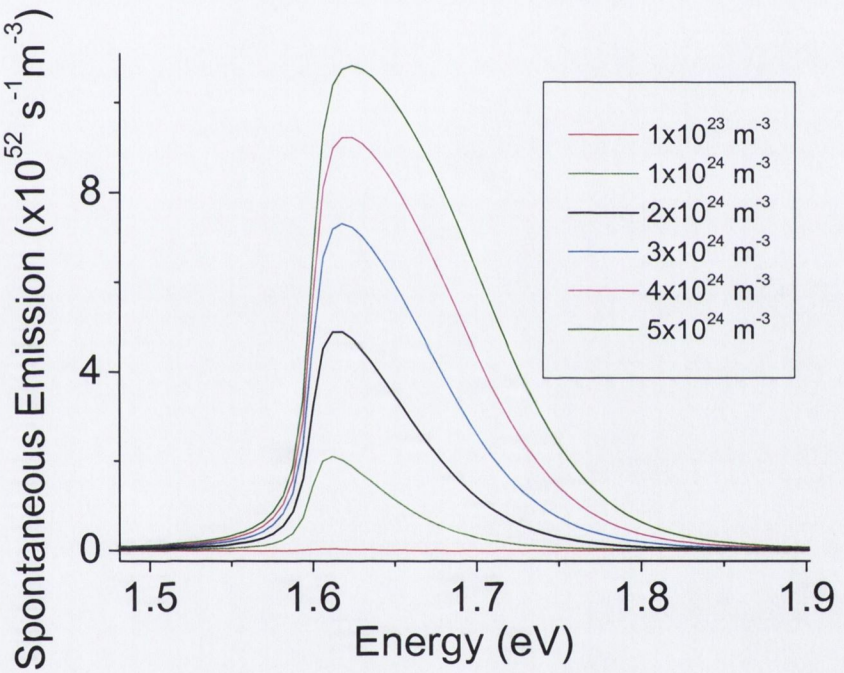


Figure 2-6 Calculated spontaneous emission profile at 300K for an $Al_{0.14}Ga_{0.86}As$ active layer material of thickness 0.06μm.

In order to determine the total spontaneous emission rate we must sum over the average of the three polarisations (2xTE + TM)/3 [20] and integrate over the emission spectrum.

$$R_{sp} = \int_0^\infty r^{spon}(\hbar\omega) d(\hbar\omega) \tag{2.27}$$

2.2.4 Intervalence Band Absorption

Intervalence band absorption (IVBA) has been proposed as a possible cause of the temperature sensitivity of threshold currents in the longer-wavelength lasers used for optical fibre communications. IVBA in III-V semiconductors results from upward radiative transitions in the valence band. As can be seen from the illustration in figure 2-7 an electron in the conduction band recombines with a hole near the valence band maximum, creating a photon of energy $\hbar\omega$, close to the bandgap energy E_g. IVBA occurs when the photon is subsequently reabsorbed by lifting an electron from the spin-split-off band (SO) into a hole state in the heavy-hole band. At optical communications wavelengths the bandgap is typically 0.5 eV greater than the spin-orbit splitting Δ, the reabsorption is expected away from the Brillouin zone centre in order to conserve energy and momentum. Phonon-assisted IVBA is also possible and has been suggested that for long wavelengths this process could be competing equally with the direct process [21]. IVBA will be considered as part of chapter 5.

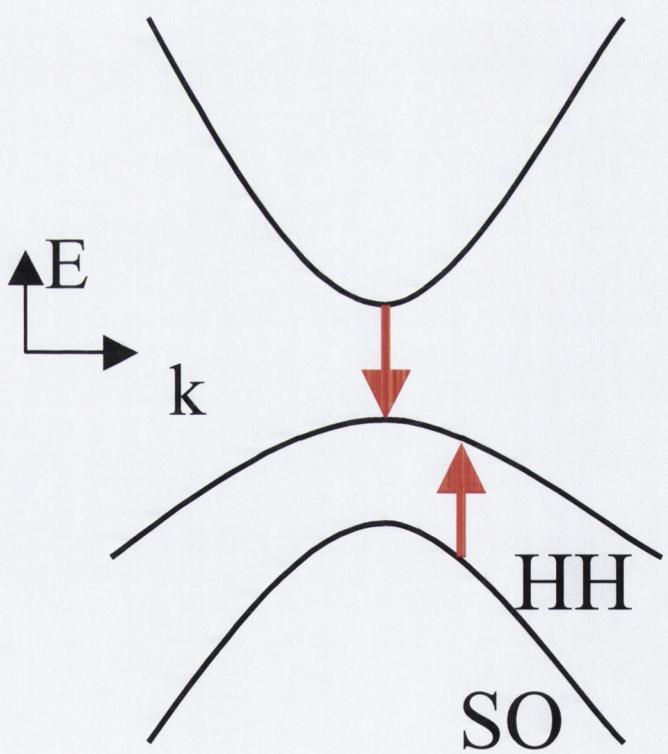


Figure 2-7 Illustration of the direct intervalence band absorption

2.2.5 Differential Index

Carrier induced refractive index changes have a dramatic effect on the weakly guided self-pulsation lasers. An understanding of the causes and effects of such a mechanism is vital to the understanding of the self-pulsation mechanism. There are three main effects that lead to an alteration in refractive index with carrier density. These effects, Burstein-Moss effect, band gap renormalisation, and free-carrier absorption, will now be discussed in turn outlining the strength of their contribution, and the processes which dominate in the carrier density regime in which the self-pulsation laser operates.

2.2.6 Burnstein-Moss Effect

Due to the Pauli exclusion principle for fermions, the conduction band quasi-Fermi level shifts upwards with increasing carrier density. As can be seen on close inspection of figure 2-5, this results in a blue shift in the gain peak with increasing carrier density. This process termed the Burstein–Moss [22][23] effect is often termed band filling. The shift in the absorption edge with increasing carrier density was first explained for InSb [22]. The observation of bandfilling is due to the fact that the effective masses of the charge carriers in other semiconductors are much larger than the effective mass of the electrons in InSb, so that a large shift in the Fermi level could be achieved for relatively small changes in the carrier density. Since the real and imaginary components of the refractive index ($n+ik$) are related through the Kramers-Kronig integrals [24]. Writing the absorption coefficient α in terms of the extinction coefficient k we get $\alpha = \frac{4\pi k}{\lambda}$ and since the refractive index can be calculated if the absorption coefficient is known for all frequencies ω, any change in the absorption coefficient $\Delta\alpha$ is accompanied by a change in the real refractive index Δn.

$$\Delta n(N,P,E) = 1 + \frac{2c\hbar}{e^2} P' \int_0^\infty \frac{\alpha(N,P,E')}{E'^2 - E^2} dE' \qquad (2.28)$$

where P' represents the principal value of the integral. Although the Burnstein-Moss effect is sometimes referred to as a shift of the absorption edge [25] in reality there is a change in the shape of α with energy E and not a simple translation.

2.2.7 Bandgap Renormalisation

There is a considerable theoretical and experimental body of work that has taken place on bandgap renormalisation or bandgap shrinkage and we will only qualitatively describe the results. The effect is most pronounced for high carrier densities in which the charges screen out the atomic forces of the atoms thereby weakening the effective atomic periodic potential. The single electron wavefunctions become less localised and the nearest neighbour electron overlap decreases, thereby reducing the energy gap between bands. Since the bandgap shrinkage is inversely proportional to the average spacing between carriers r_s, then $\Delta E_g \propto -1/r_s$, using an expression from [26] originally developed by Wolf [27]

$$\Delta E_G = -\left(\frac{e}{2\pi\varepsilon_0\varepsilon_s}\right)\left(\frac{3}{\pi}\right)^{1/3}\chi^{1/3} \tag{2.29}$$

The renormalisation causes a red shift of the absorption curve. Unlike the case of the Burnstein-Moss effect, Δn is positive for energies below the bandgap.

2.2.8 Free-Carrier Absorption

We have so far considered the variation in the interband absorption due to the Burnstein-Moss Effect and bandgap renormalisation. Apart from these interband processes a free carrier can absorb a photon and move higher into the band. This effect can be estimated using the classical dipole oscillator model of Drude and Lorentz. Based on the assumption that the free carriers move in the optical field according to Newton's second law then the polarisation produced $\mathbf{P}$, is related to the electric field $\mathbf{E}$ by

$$\mathbf{P} = -\frac{e^2}{\omega}\left(\frac{N}{m_e}+\frac{P}{m_h}\right)\mathbf{E} \tag{2.30}$$

As shown in [28] this leads to a refractive index change,

$$\Delta n = -\left(\frac{e^2\lambda^2}{8\pi^2c^2\varepsilon_0 n}\right)\left(\frac{N}{m_e}+\frac{P}{m_h}\right) \tag{2.31}$$

where, $\lambda, \varepsilon_0, m_e, m_h, n, N, P$ denotes the photon wavelength, permittivity constant, electron mass, hole mass,carrier independent refractive index, electron carrier density

and hole carrier density respectively. As in the case of the Burnstein-Moss effect, free carrier absorption Δn is negative for energies below the bandgap. Both effects are greatest near the band gap and approach zero for $E \ll E_g$.

Combining the three carrier effects for concentrations above 10^{24}m^{-3}, the model in [26] predicts band filling to be dominant resulting in $\Delta n < 0$. Bandgap renormalisation was found to be important over the carrier concentration range $1\times10^{23}\ m^{-3} \le N = P \le 5\times10^{23}\ m^{-3}$, approximately cancelling the Burnstein-Moss effect. Comparison with experiments is difficult as has been pointed out in [26], since the number of precise measurements of the index change with carrier density is quite small but of those that are available [29][25], both agree quite well with the values derived in [26].

2.3 Non-Radiative Processes

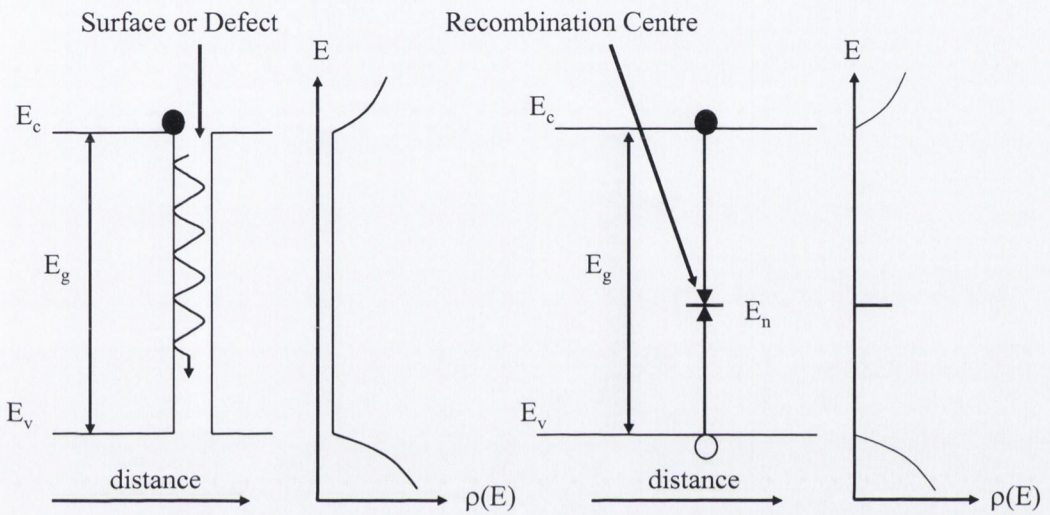
With the radiative transitions defined in sections 2.3.1 and 2.3.3, we will now consider the non-radiative transitions. Within the semiconductor crystal, non-radiative recombination is related to crystalline defects, impurities, and the Auger effect.

2.3.1 Defect and surface recombination

Among the crystalline defects are dislocations, stacking faults and point defects such as interstitial atoms and vacancies. These defects affect the tight binding state between electrons and atoms, which may give rise to a continuum of states in the band gap joining the conduction band to the valence band, as illustrated in figure 2-8(a). As shown in figure 2-8(b) point defects often produce deep level traps in the bandgap. This type of recombination often results in the emission of a lower-energy photon from that of the band gap resulting in a lowering in the efficiency of the device. The defect or impurity recombination rate R_d was first analysed by Shockley and Read [30] and independently by Hall [31]. Within the Boltzmann nondegenerate carrier density regime the defect recombination rate takes the form.

$$R_d = \frac{NP - N_i^2}{\left(N^* + N\right)\tau_h + \left(P^* + P\right)\tau_e} \tag{2.32}$$

where N_i is the intrinsic carrier density, τ_e is the time required to capture an electron from the conduction band assuming all the traps are empty, and τ_h is the time required to capture a hole from the valence band assuming all traps are full. Since the capture time is inversely proportional to the trap density, the higher the trap densities the shorter the capture time. N^* and P^* represent the electron and hole carrier densities that would exist if the Fermi level was aligned with the energy level of the trap.



(a)
Defect or Surface effects in Crystal resulting in a continuum of states

(b)
Deep level Defect in Crystal

Figure 2-8 (a) Depiction of the continuum of resulting from surface recombination or defects within the crystal. (b) Discreet deep level as a result of a point defect.

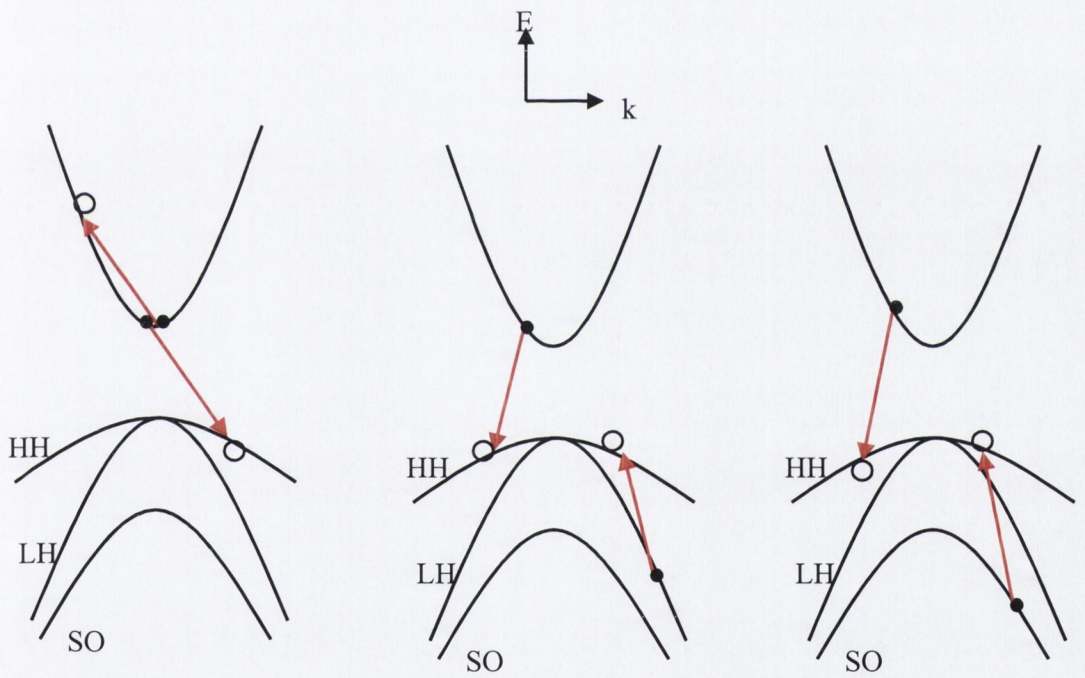
If the trap level is close to the band edge then these terms become large, thereby reducing the defect recombination rate. From this it is clear that the reduction in the density of deep level traps as shown in figure 2-8(b) will reduce the defect recombination rate significantly more than for their shallow counterparts. At the lasing levels of carrier concentration in which $N = P >> N_i, N^*, P^*$, equation (2.32) reduces to

$$R_d = \frac{N}{\tau_h + \tau_e} \tag{2.33}$$

Another form of nonradiative transition, as depicted in figure 2-8(a), is that of recombination via surface states of the crystal. In a similar manner to the two-step defect recombination mechanism the continuum of states is brought about through the termination of the crystal lattice at the surface or at interfaces between two materials. The unmatched bonds that occur at one side of the surface or interface gives rise to dangling bonds, which occur at high enough densities to form minibands. Recombination via surface states can be treated in an analogous manner to defect and impurity recombination via the Shockley-Read-Hall theory.

2.3.2 Auger Recombination

Although a nonradiative process, the Auger recombination effect is not related to the recombination processes via defects and surface recombination creating levels within the bandgap.



(a) CHCC (b) CHLH (c) CHSH

Figure 2-9 Band-to-band Auger processes in direct bandgap semiconductors. Closed circles denote the initial states, while the final states, before phonon interaction, are denoted by open circles.

Within this process the energy released during the electron-hole recombination is transferred to another electron or hole which is excited to a higher energy state in the band. The electron or hole relaxes back to its equilibrium state with the emission of its

energy through phonons (lattice vibrations). The three band-to-band Auger processes are depicted in figure 2-9. The three processes are labelled CHCC, CHLH, CHSH, where C stands for the conduction band, and H, L, and S stand for the heavy-hole, light hole, and split-off valence bands respectively. In the CHCC process, an electron recombines with a hole and the excess energy generated is transferred to another electron, which is excited into the band. This electron loses its energy to phonons when it relaxes back to thermal equilibrium. In a similar manner the CHLH and CHSH involve one electron state, two heavy-hole states, and one split-off or light-hole state. Since Auger recombination rate is a three-carrier nonradiative recombination process (for example, two electrons and one hole state as shown in figure 2.9a for the CHCC process) it will increase with carrier density.

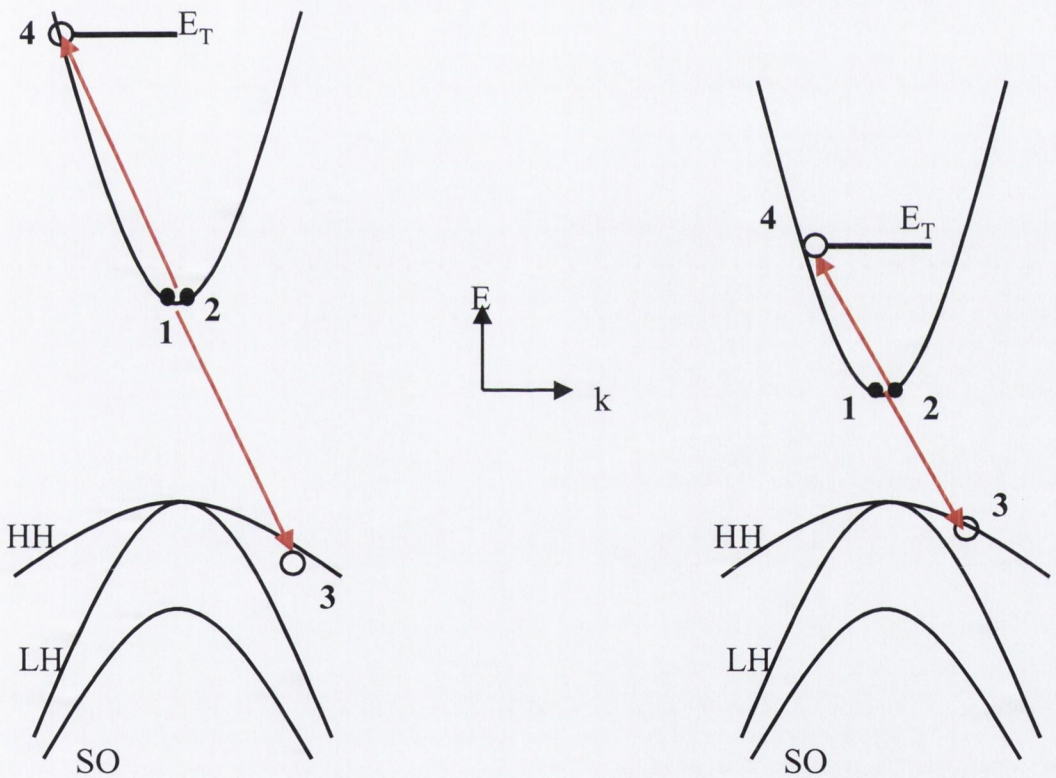


Figure 2-10 Illustration of the CHCC Auger process for a wide and narrow bandgap material.

The rate of Auger recombination R_A is proportional to the cube of the carrier density, and for an un-doped active region where electron density is equal to the hole density (N = P), $R_A = CN^3$.

Here C represents the Auger coefficient, whose magnitude is dependent on the predominant Auger process as well as the material used. The Auger recombination rate is strongly dependent on the bandgap material. A qualitative description of why

the Auger recombination rate is larger for narrow band gap material can be derived from the illustration in figure 2-10. As we can see for the wider band gap material the position of the hole in state 3 is further into the heavy hole band than in the case of the narrower bandgap. The probability that a hole exists for state 3 is greater in the narrower band gap case following on from the Fermi statistics. As has been shown in [32], the probability of the initial electron hole transition is maximised when the difference between the conduction band edge and empty higher conduction band state (4), which is referred to as the threshold value E_T, is minimised. Although this illustration is not quantitatively accurate, since it only considers the transition between one set of states in the low carrier density Boltzmann approximation regime, it does illustrate the severity of the problem for long-wavelength lasers, which will be come important in chapter 5. Another type of Auger recombination involves phonon-assisted transitions. In the case of phonon assisted Auger recombination, the final momentum of the two electrons does not equal the initial momentum, but through phonon interaction the overall momentum is conserved. Since phonon assisted Auger recombination involves an extra particle the process is less likely to occur. They begin to become important when the normal Auger recombination is a minimum, such as for large bandgap materials and/or at low temperatures. For example, Auger recombination in GaAs is dominated by phonon-assisted processes, wheras in InGaAsP long-wavelength materials are dominated by by normal Auger processes at room temperature. However, as at low temperatures below 100-150°C, normal Auger recombination processes begin to be suppressed, and the less temperature sensitive, phonon-assisted processes begin to dominate even in long-wavelength materials [32].

2.4 Carrier Recombination Rates

The radiative and non-radiative recombination rates that we have expressed earlier can be combined into an overall recombination rate denoted by R_{rec}. This consists of a contribution from the spontaneous recombination rate, R_{sp}, the non-radiative recombination rate, R_{nr}, and the stimulated recombination rate R_{st}.

$$R_{rec} = R_{sp} + R_{nr} + R_{st} \tag{2.34}$$

As many of the principle methods of determination of the carrier lifetime are taken at or below the threshold current it has become standard practice to separate the stimulated recombination rate from that of the total recombination rate and to assign a carrier lifetime τ to describe the spontaneous and non-radiative processes collectively as

$$R_{rec} = \frac{N}{\tau} + R_{st} \tag{2.35}$$

By expanding $1/\tau$ into a power series of N up to the third order we obtain the expression

$$\frac{N}{\tau} = BN^2 + \left(AN + CN^3\right) \tag{2.36}$$

The spontaneous recombination rate R_{sp} that we defined in equation (2.27) is equal to BN^2, where B is referred to as the bimolecular recombination coefficient. The non-radiative recombination rate is divided into two components, the combined contribution of surface and defect contributions and those due to Auger recombination. The non-radiative recombination due to defects and surface effects as defined in section 2.3 is denoted by the AN term. It is equivalent to the (2.33), if surface effects are included. Since the non-radiative Auger recombination process, denoted by CN^3 is only appreciable for the narrow bandgap materials, this term is included for the InGaAsP/InP material system only. The A and C terms are determined from experiment measurements of the carrier lifetimes of the specific material.

2.5 Double-Heterostructure Design

The double-heterostructure laser diode consists of a thin region of undoped active region sandwiched between p and n type cladding layers, which have a higher energy band gap than the active material.

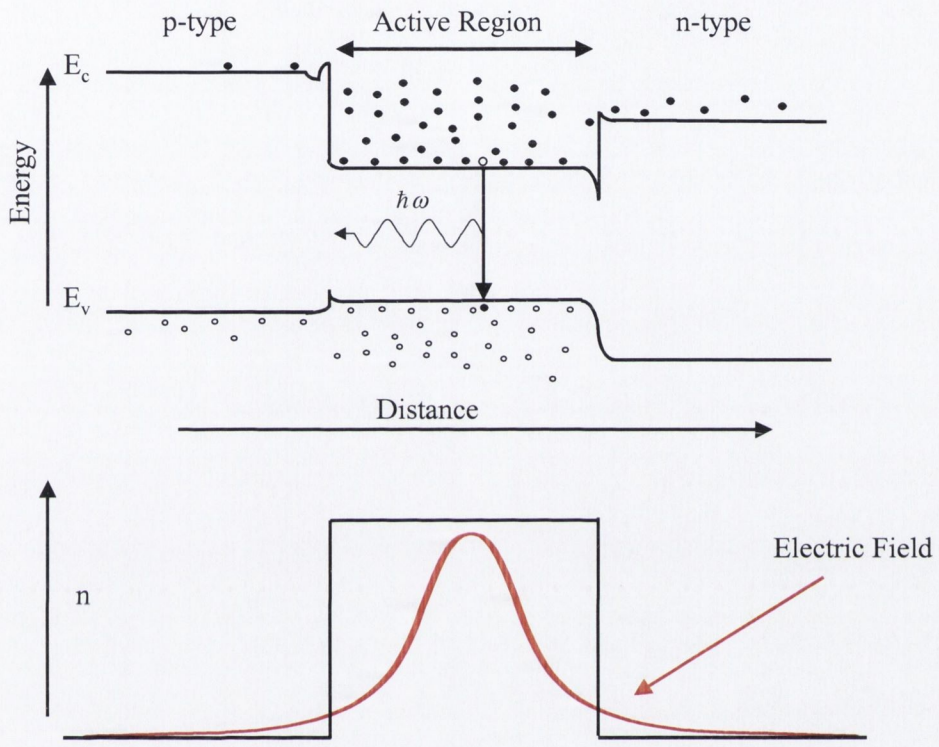


Figure 2-11 Energy band diagram and refractive index profile illustrating the electric field for a double-heterostructure laser under forward biased conditions.

This bandgap difference between the cladding and active regions as shown in figure 2-11 results in the formation in potential barriers that confine the injected carriers to the active region. Of course it is important to ensure that the material for the cladding and active region are chosen so that they are latticed matched, or that the amount of strain is small in order to prevent any dislocation or defects at the active cladding layer interface. In the lower half of the figure 2-11 we see that the bandgap of the active region has a higher refractive index than the surrounding cladding and therefore the light is confined within this region. The tail of the optical field that is not contained within the active region is not absorbed in the cladding layers due to the higher energy bands in these regions. The overlap of the electric field profile and the high refractive index active region is depicted in the lower half of figure 2-11. It

should be noted that the band diagram is not drawn to scale and the active region is much smaller than the surrounding cladding layers. This combination of carrier and optical confinement increases the probability of radiative recombination. It was the use of the double heterostructure, which transformed the earlier homostructure devices that were only operable at low temperatures, into truly practical devices for the first time.

2.6 Optical Waveguiding

In this section we will describe how the optical field is calculated within the semiconductor laser diode waveguide. The important concepts such as the optical confinement factor, modal gain and the effective index approximation will be discussed.

2.6.1 Scalar Wave Equation

Since the classical description of all optical phenomena is based on Maxwell's equations, it is appropriate that we would start our discussion considering these equations. The semiconductor waveguide media is assumed to be isotropic, non-conducting and nonmagnetic. Hence, the permeability μ is equal to μ_0 everywhere. For harmonic wave propagation along the longitudinal z direction we consider the electric and magnetic fields

$$\mathbf{E}(x,y,z,t) = (E_x, E_y, E_z)e^{i(\omega t - \beta z)} \tag{2.37}$$

$$\mathbf{H}(x,y,z,t) = (H_x, H_y, H_z)e^{i(\omega t - \beta z)} \tag{2.38}$$

$$\mathbf{D} = \varepsilon(x,y)\mathbf{E}, \quad \mathbf{B} = \mu_0 \mathbf{H} \tag{2.39}$$

Where $\mathbf{D}, \varepsilon,$ *and* $\mathbf{B}$ represent the electric displacement vector, the permittivity and the magnetic flux density vector respectively. It should be noted that symbols in bold denote vector quantities. Since the components of the electric and magnetic field are components of x and y only. From Maxwell's equations for source free regions,

$$\nabla \cdot \mathbf{D} = 0, \quad \nabla \cdot \mathbf{B} = 0 \tag{2.40}$$

$$\nabla \times \mathrm{E} = -\frac{\partial \mathbf{B}}{\partial t} = -i\omega\mu_0 \mathrm{H} \tag{2.41}$$

$$\nabla \times \mathbf{H} = \frac{\partial \mathbf{D}}{\partial t} = i\omega\varepsilon \mathbf{E} \tag{2.42}$$

we obtain

$$\nabla \times \left(\nabla \times \mathbf{E}\right) = \nabla\left(\nabla \cdot \mathbf{E}\right) - \nabla^2 \mathbf{E} = \omega^2 \varepsilon \mu_0 \mathbf{E} = k^2 \mathbf{E} \tag{2.43}$$

in which

$$k\left(x, y\right) = \omega\left(\varepsilon\mu\right)^{\frac{1}{2}} = 2\pi n\left(x, y\right) / \lambda \tag{2.44}$$

where λ is the vacuum wavelength. By taking the derivative of both sides of equation (2.43) we find that

$$\nabla \cdot \mathbf{E} = -\mathbf{E} \cdot \nabla \log_e k^2 \tag{2.45}$$

which upon substitution into equation (2.43) yields the wave equation

$$\nabla^2 \mathbf{E} + k^2 \mathbf{E} + \nabla\left(\mathbf{E} \cdot \nabla \log_e k^2\right) = 0 \tag{2.46}$$

As $k\left(x, y\right)$ is piecewise constant $\nabla \log_e k^2 = 0$ and from equation (2.37) we find that

$$\frac{\partial}{\partial z} \equiv -i\beta, \qquad \frac{\partial^2}{\partial z^2} \equiv -\beta^2 \tag{2.47}$$

and equation (2.46) reduces to the Helmholtz wave equation

$$\frac{\partial^2 \mathbf{E}}{\partial x^2} + \frac{\partial^2 \mathbf{E}}{\partial y^2} + \left(k^2 - \beta^2\right)\mathbf{E} = 0 \tag{2.48}$$

In the case of the self-pulsation laser diodes studied here, the waveguide structure consists of materials whose dielectric constants are very nearly identical in those regions where the field intensity is large, then a scalar solution of the wave equation will suffice. The scalar wave equation can then be written as

$$\frac{\partial^2 E_z}{\partial x^2} + \frac{\partial^2 E_z}{\partial y^2} + \left(k^2 - \beta^2\right) E_z = 0 \tag{2.49}$$

where we solve for the field profile $E_z(x, y)$. The optical field propagates in the transverse electric polarisation (TE) in the self-pulsation diode lasers discussed here and this is true for most laser diodes. There are a number of reasons why this is the case. Firstly the reflectivity coefficient is larger for the TE field [33] and therefore the modal loss through the mirror facets for the TE polarisation is less. Secondly, if the active layer is composed of quantum well(s), that are not under tensile strain, then the TE polarisation has a higher material gain, and in fact in the case of compressive strain at room temperature, the transverse magnetic component is drastically suppressed due to the removal of the light hole subband transitions [34]. And finally the optical confinement factor, which shall now be defined, is in general greater in the TE case.

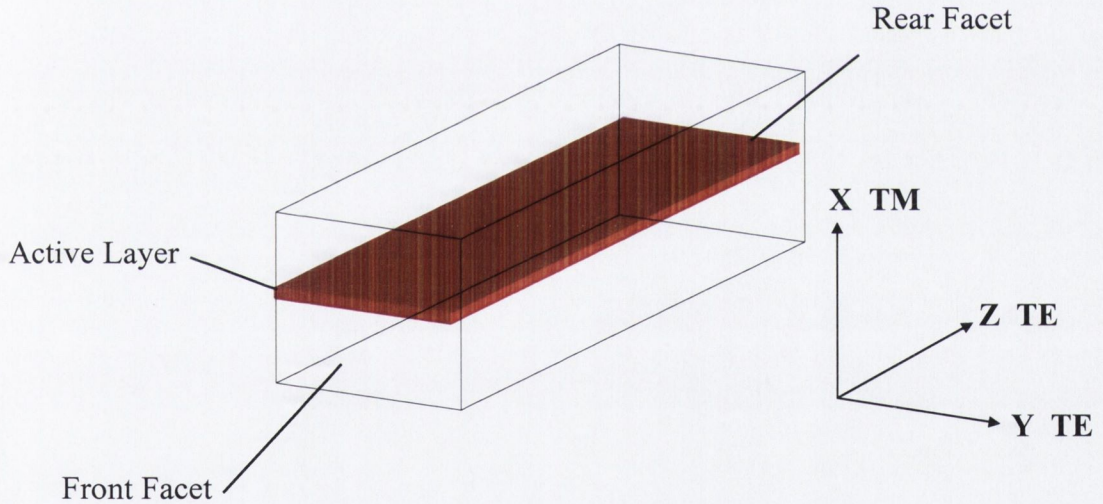


Figure 2-12 Illustration of the laser diode showing the active region and the front and rear facets where the light is emitted. The direction of propagation is along the z axis.

2.6.2 Optical Confinement Factor and Modal Gain

Let us consider the Helmholtz equation for TE polarisation. In this case the non zero components are $\{E_y, H_x, H_z\} \neq 0$, eliminating these from the Maxwell equations yields the following wave equation for E_y

$$\left[\frac{\partial^2}{\partial x^2} + k^2 - \beta_z^2\right] E_y = 0 \tag{2.50}$$

Multiplying by the complex conjugate of E_y and integrating the result from minus to plus infinity gives

$$\beta_z^2 \int_{-\infty}^{+\infty} \left|E_y(x)\right|^2 dx = \int_{-\infty}^{+\infty} E_y^* \frac{\partial^2}{\partial x^2} E_y dx + k^2 \int_{-\infty}^{+\infty} \varepsilon_r \left|E_y(x)\right|^2 dx \tag{2.51}$$

since

$$\int_{-\infty}^{+\infty} E_y^* \frac{\partial^2}{\partial x^2} E_y dx \in \mathbb{R} \tag{2.52}$$

if we take the imaginary component of (2.51) yields

$$\mathrm{Im}\left\{\beta_z^2\right\} = \sum_i \Gamma_i^{TE} \mathrm{Im}\left\{k_i^2\right\} \tag{2.53}$$

where Γ_i^{TE} represents the transverse confinement factor for the ith layer, which is defined as

$$\Gamma_i^{TE} \equiv \frac{\int_i \left|E_y(x)\right|^2 dx}{\int_{-\infty}^{\infty} \left|E_y(x)\right|^2 dx} \tag{2.54}$$

Form the standard expression for the modal gain $G = 2k_0 \,\mathrm{Im}\{\beta_z\}$ and assuming weak guiding such that $\mathrm{Re}\{\beta_z\} = \mathrm{Re}\{\beta_i\}$ this leads us to the expression for the total modal gain within the cavity

$$G = \sum_i \Gamma_i^{TE} g_i \tag{2.55}$$

This formula captures the essence of the modal gain, due to the fact that a small percentage of the optical field occupies the active region of localised material gain or loss. The confinement factor of the active region is the fraction of the optical mode

that overlaps this region. This well known result can also be derived from scalar theory but a corresponding relation does not hold for the TM or transverse magnetic mode in which the electric field component is in the growth direction (the x direction in figure 2-12). As has been shown in [35], since $\mathrm{Re}\{n_i\} \gg \mathrm{Im}\{n_i\}$ it follows that,

$$G = \sum_i \Gamma_i^{TM} g_i - \left(k_0^3 \int_{-\infty}^{\infty} |H_y(x)|^2 dx \right)^{-1} \sum_{x_q,i} \mathrm{Im}\left\{ H_y^* \frac{i\Delta \mathrm{Im}\{n_i\}}{\mathrm{Re}\{n_i\}} \frac{\delta}{\delta x} H_y \right\} \qquad (2.56)$$

Here we can see that the connection between modal gain and confinement factor is different for the transverse magnetic or TM mode. In conclusion the use of scalar theory to determine the confinement factor and modal gain does not neglect the polarisation effects but it is only appropriate for the case of TE modes.

2.6.3 Effective Index Method

The effective index method is an approximate technique for solving the two-dimensional Helmholtz equation given by equation (2.50) by separation of variables. Provided the lateral (y direction) refractive index variation is much less than the transverse index variation (x direction) then we can approximate the two-dimensional electric field as

$$E(x,y) = \psi(x,y_i)\Phi(y) \qquad (2.57)$$

where $\psi(x,y_i)$ is the transverse electric field in the x direction at the point y_i. The first step of the effective index technique is to find the effective index values at each position y_i for all of the lateral sections. The effective index is simply defined as the transverse propagation constant divided by the vacuum wavenumber.

$$n_{eff}(y_i) = \frac{\beta_x}{k_0} \qquad (2.58)$$

Then the one dimensional slab waveguide comprising of the effective index for each of the lateral sections is solved, resulting in the lateral field profile as shown in figure 2-13. Unfortunately although the effective index is surprising accurate for strongly guided waveguides, the technique becomes unreliable as the fundamental mode approaches cutoff. A further discussion of this and other numerical techniques for the solution of the two-dimension scalar wave equation will now follow.

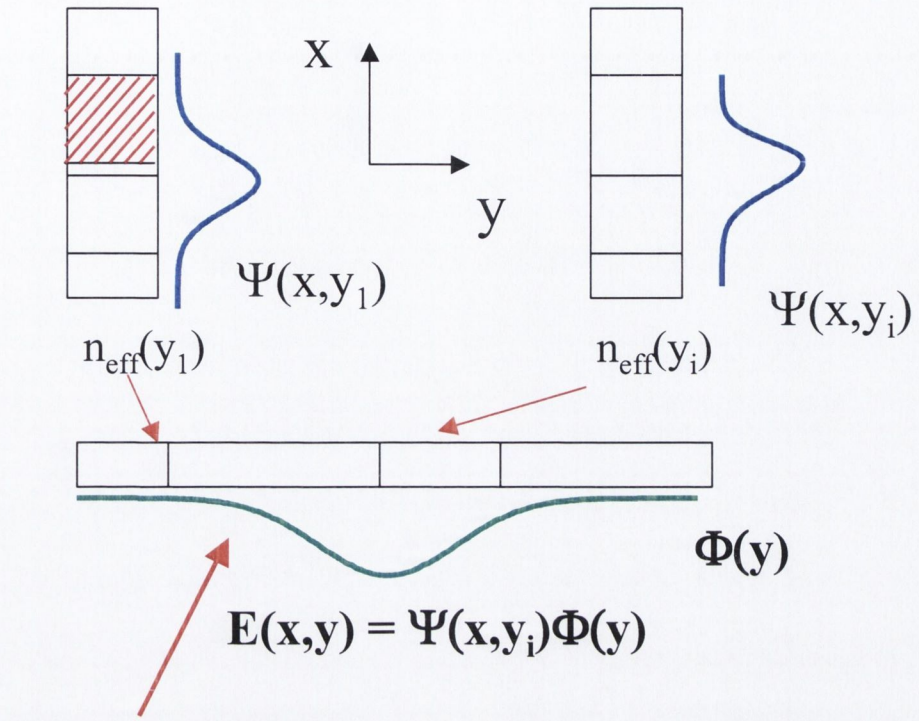


Figure 2-13 Illustration of the effective index method showing the solution of the transverse waveguide giving the effective index that forms the lateral waveguide, from which $\Phi(y)$ is determined

2.7 One Dimensional Waveguide Analysis

For the self-aligned self-pulsation device design it is necessary to consider the effects of carrier induced variation in the real and imaginary components of the refractive index as part of the waveguiding analysis. Since there is no variation in the device design along the longitudinal length we will make the approximation that the device can be solved using the two-dimensional wave equation. Unfortunately only a few geometries and index profiles are amenable to exact analysis. These waveguides consist of real index guided, simple geometry designs. Thus numerical and approximate techniques become important for a complex refractive index guided structure composed of a multitude of lateral and transverse sections and layers. Due to the fact that we are interested in the temporal and spatial variation in the photons and carriers within the device there are two overriding factors as to our choice of numerical method for the solution of the wave equation.

The first consideration is computational efficiency. It will be necessary to calculate the waveguiding properties of the device such as effective index and confinement factor on a timescale of the order of the photon lifetime, and so for a 5ns simulation in which the field profile is updated at every picosecond, it would be necessary to calculate the field around 5000 times. A computationally efficient method would therefore be the first prerequisite. Secondly as we are dealing with devices that are weakly guided in the lateral direction and whose solution depend on the effects of both the real and imaginary refractive index, we would choose a method that could incorporate a weakly complex guided waveguide close to cutoff. A discussion of the performance of some key numerical techniques employed with the aim to meet the previous two criteria will now be outlined.

2.7.1 Galerkin's Formalism in One Dimension

2.7.2 Sine Series Basis Function

By expanding the electric field as an orthogonal sine series we can solve the transverse waveguide in the growth direction.

$$E = \sum_{v=1}^{N} c_v \sin\left(\frac{\pi v x}{L}\right) \tag{2.59}$$

Where L denotes the distance between the computational boundaries.

Air	$n_6 = 1.00$
Au	$n_5 = 0.18 - 10.2i$
p-InP	$n_4 = 3.16 - 0.001i$
InGaAsP	$n_3 = 3.60 + 0.02i$
n-InP	$n_2 = 3.16 - 0.001i$
InP	$n_1 = 3.16$

Figure 2-0-14 Geometry of the planar optical amplifier with both gain and losses used for comparison of both methods. The vacuum wavelength is $\lambda 0 = 1.3\mu m$.

The validity of this approach can be confirmed by comparing this technique with the results of Visser et al [36] who uses a scattering matrices formalism to compute the TE and TM modes for waveguides containing gain and losses as shown in figure 2-14.

	Visser : Scattering Matrices Formalism	Galerkin's Method : Sine Series Basis
Real Effective Index	3.2808	3.2809
Imaginary Effective Index	9.139×10^{-4}	9.138×10^{-4}

Table 2-1 Comparison of the scattering matrix and Galerkin's method for a waveguide with gain and losses.

Through the expansion of the transverse electric field as a function of orthogonal sine functions the field profile of the mode with the largest modal gain is used to determine the effective index and transverse confinement factor.

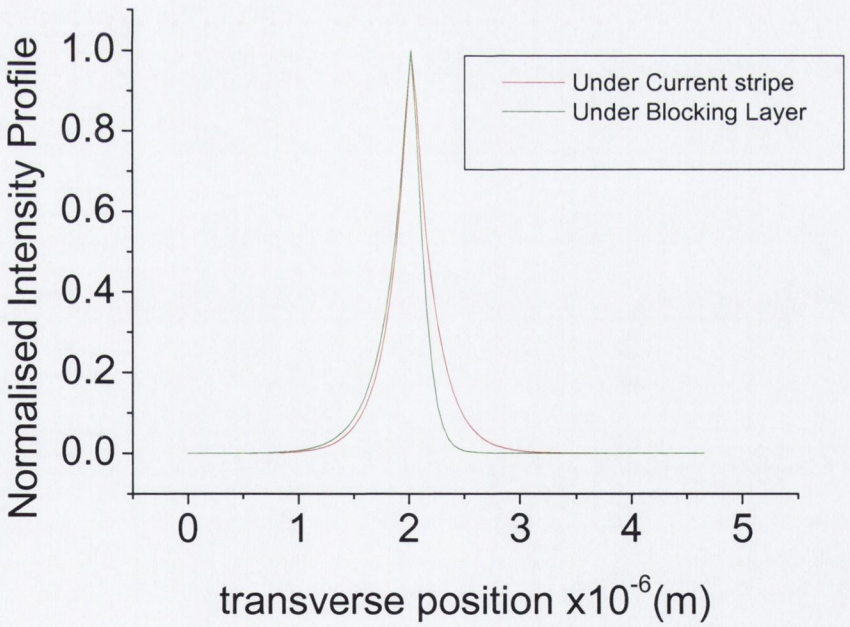


Figure 2-15 Transverse intensity profile for a self-pulsation device reflecting the asymmetry of the waveguide in the region under the current blocking layer. (The transverse direction is also referred to as the growth direction, where the origin lies at the beginning of the substrate layer)

Figure 2-15 shows the Intensity profile for the 0_{th} order mode for the region below the current blocking layer and that in the region under the current stripe. The effect of the lower index current blocking layer is clearly evident from the asymmetric intensity profile compared to that of the more symmetric profile of that under the current stripe. By considering the effects of carrier density on the refractive index of the active region it is possible to determine the effective index and transverse confinement factor versus carrier density.

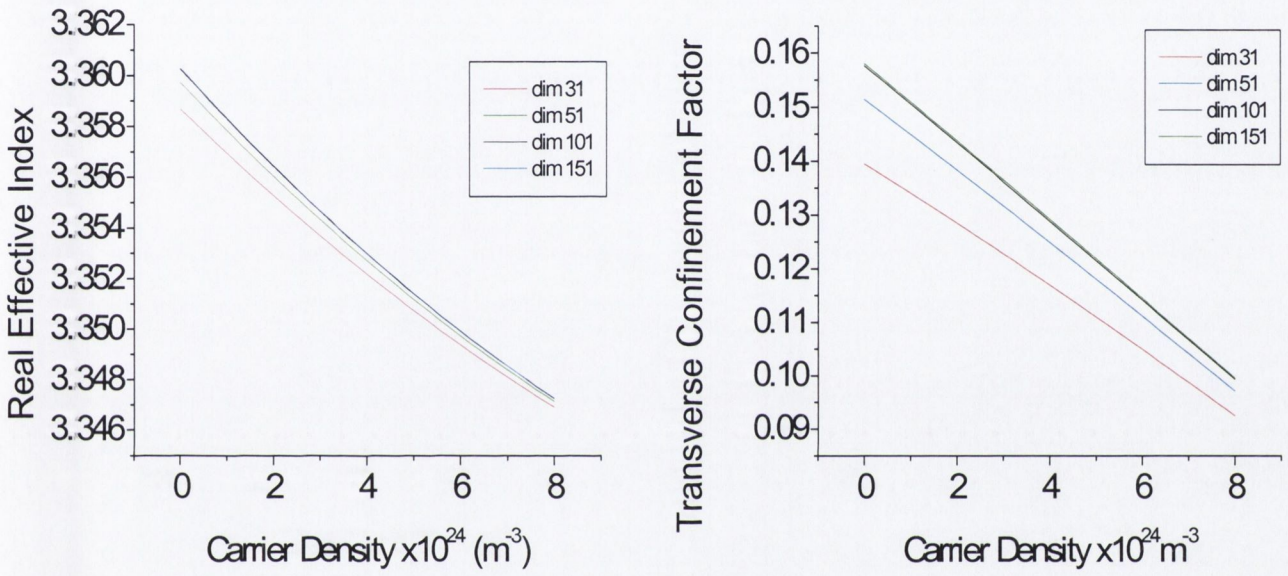


Figure 2-16 Illustration of the convergence with number of basis functions of the variation of real effective index and transverse confinement factor with carrier density

As can be seen from figure 2-16, as the number of basis functions (dim) increase from 31 to 151 the effective index converges. The effect of increasing the carrier density within the active region lowers the refractive index of that layer and causes the light to become less confined to the active layer region resulting in a lowering of the transverse confinement factor and effective index. One of the main benefits from this type of approach is that an accurate solution for the effective index and transverse confinement factor can be achieved with a relatively small number of sine terms thus making this approximate scheme computationally efficient. Restricting the solution of the wave equation to a finite domain does not present problems for well-guided modes whose intensity decays exponentially with increasing distance from the waveguide core and can be assumed to be zero at the boundary of a sufficiently large

domain. The restriction to a finite domain presents a problem for a weakly guided waveguide and a different basis function or method is required. Once we obtain the effective index values from the transverse strongly guided direction the small contrast in effective index between the region under the current stripe and that under the current blocking layers leads us into the weakly guided complex index regime in which the sine series approximations of the sine series expansion no longer hold.

2.7.3 Hermite-Gauss Basis

Unfortunately the sine series basis function does not satisfy the boundary conditions at infinity. At modes close to cutoff any trigonometric basis functions depend critically on the size of the domain and it becomes difficult to choose the size of the domain in order to give accurate results [37], [38]. By applying a complete set of Hermite–Gauss functions rather than trigonometric functions, (these functions naturally satisfy the boundary conditions at infinity), the need for enclosing the waveguide structure in a computational window is eliminated [39]. These functions suffer from a major drawback over their trigonometric basis cousins in that unless the real and imaginary parts of the normalised refractive index are expressible (or can be approximated) in a power series expansion then the integrations involved in the algebraic equation require a numerical solution. The accuracy of the solution depends on this and the computing effort increases considerably. This therefore does not represent a viable option for the refractive index profiles of interest here.

2.7.4 Finite Difference Method

The finite difference method (FDM) was first developed by A.Thom [40] in the 1920s under the title "the method of squares" to solve non-linear hydrodynamic equations. Since then the method has found applications in solving different field problems. The finite difference techniques are based upon approximations, which permit replacing differential equations by finite difference equations. These finite difference approximations are algebraic in form; they relate the value of the dependent variable at a point in the solution region to the values at some neighbouring points

Instead of approximating the solution of the electric field with various mathematical basis functions, the finite difference method involves overlaying a grid of finite period over the waveguide, the field will be determined at the nodes of the grid by converting

the scalar wave equation into a set of finite difference equations specified at the grid points. After discretisation, the differential equation is assembled into a system matrix A as shown below.

$$AE = \beta^2 E \tag{2.60}$$

As in the case of Galerkin's method, the use of complex refractive indices within the waveguide results in the matrix A being non-hermitian, the dimension of which is determined by the number of grid points. The accuracy of the finite difference method depends on the grid size, the assumed nature of the electromagnetic field, (scalar, polarised or vector) and on the order of the finite difference scheme used. The time taken for the solution of the eigenvalue equation is proportional to the cube of the dimension, so this can lead to strongly increased computational time. As in the case of Galerkin's method, we can apply the effective index approximation to our two dimensional waveguide. If we consider the solution of the lateral effective index slab, as we lower the effective index step, the field intensity will occupy a greater proportion of the lower effective index regions. Figure 2-17 represents the variation in effective index step size based on the solution of the transverse waveguide for a device whose stripe width is 1.6μm.

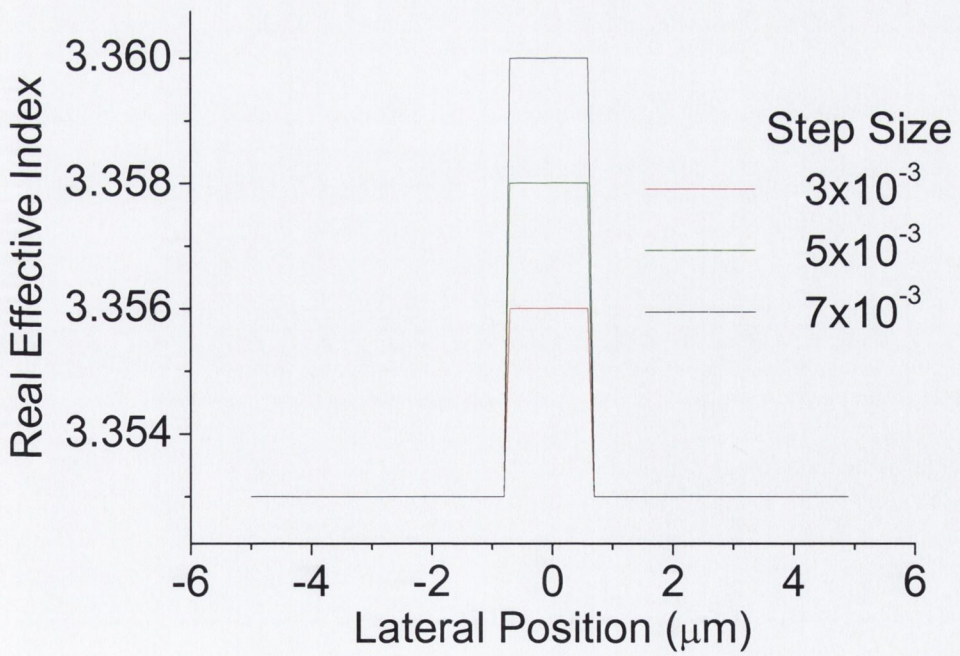


Figure 2-17 The variation in real effective index step between the region under the stripe and the passive region

This example is used to indicate the basic principle of lateral field spreading with a reduction in effective index step without the complications of including carriers. The consideration of the effective index step difference between the region lying under the current stripe and that under the current blocking layer is an important factor in any self-pulsation device design of this kind.

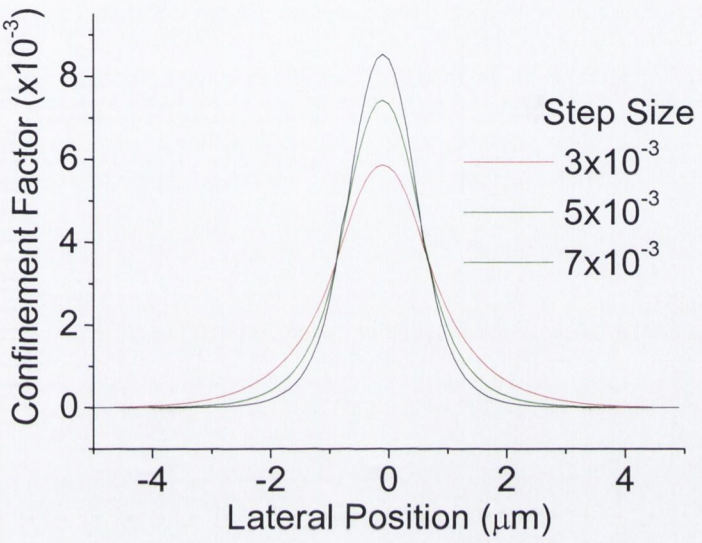


Figure 2-18 Demonstrating the spreading out of the normalised lateral field intensity profile with the reduction in the effective index step

The advantage of the finite difference technique over that of Galerkin's method, is that provided the computational window is large enough to accommodate the field a variation in it will not effect the solution. The effective index method is accurate provided the change in refractive index in the lateral dimension is slowly varying relative to the refractive index steps in the transverse waveguide. As the lateral effective index step decreases, the waveguide becomes progressively more anti–guiding and the effective index approximation breaks down. The degree to which this failure was present in our weakly guided structures needed to be examined. Since the computational load increases significantly in going from 2x1D to 2D solution, the 2D sine series expansion method was initially tested.

2.8 Two Dimensional Methods

2.8.1 Sine Series Expansion

By considering the solution of a standard strongly guided real index structure it was possible to examine the effects of variations in the computational window on the accuracy of the solution. Let us consider the simple case of a rectangular waveguide core embedded in a homogenous medium given in [41].

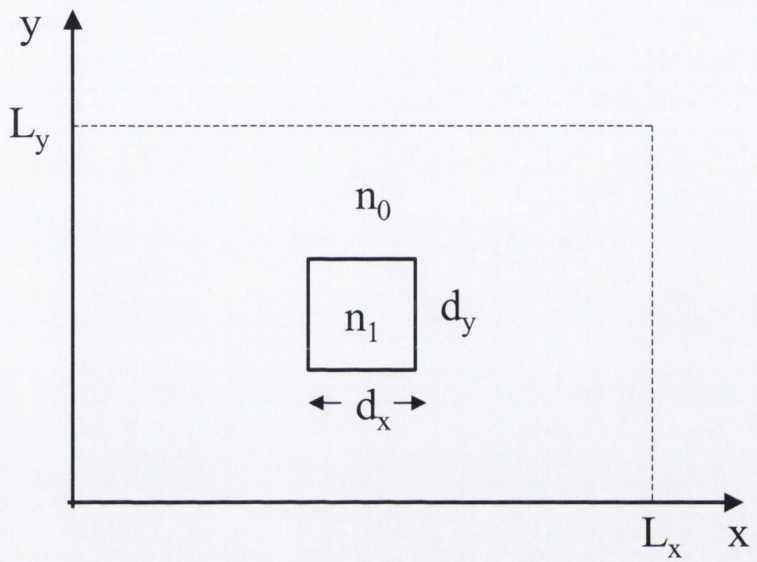


Figure 2-19 Rectangular embedded waveguide core. The dotted outline represents the boundary of the computational window

The function

$$\phi_{\mu\nu}(x,y) = \sqrt{\frac{4}{L_x L_y}} \sin\left(\frac{\pi}{L_x}\mu x\right) \sin\left(\frac{\pi}{L_y}\nu y\right) \tag{2.61}$$

with integers μ and ν forms a complete orthogonal set over the domain $0 < x < L_x$ and $0 < y < L_y$ that satisfy the orthogonality conditions

$$\int_0^{L_x} dx \int_0^{L_y} dy\, \phi_{\mu\nu}(x,y)\phi_{rs}(x,y) = \delta_{\mu r}\delta_{\nu s} \tag{2.62}$$

The optical field can now be expressed as

$$\psi = e^{-i\beta z} \sum_{\mu=1}^{N_x} \sum_{\nu=1}^{N_y} c_{\mu\nu}\phi_{\mu\nu}(x,y) \tag{2.63}$$

A waveguide with a square core, $d_x = d_y = 3$ μm, $n_1 = 1.05$, $n_0 = 1$ at an operating wavelength of 1 μm was chosen initially and the computational window was defined by $L_x = 10\mu m$ and $L_y = 15\mu m$. Due to the increased length in the y direction, the number of terms used in the series expansion is $N_y = 15$ as opposed to $N_x = 10$ in the x direction. If we define the frequency parameter V as,

$$\frac{V}{\pi} = \frac{2D}{\lambda}\left(n_1^2 - n_2^2\right)^{\frac{1}{2}} \tag{2.64}$$

Then $\frac{V}{\pi}$ = 1.92 and the calculated normalised propagation constant has the value 0.281, in agreement with [42].

Figure 2-20 illustrates the weakness of sine series expansion using Galerkin's method. By taking a well guided structure and varying the computational window, oscillations appear for the part of the field overlapping the cladding region. Increasing the number of basis functions from $N_x = 7$ to $N_x = 20$ and $N_y = 15$ to $N_y = 30$ does not cause the electric field to decay to zero at the boundary.

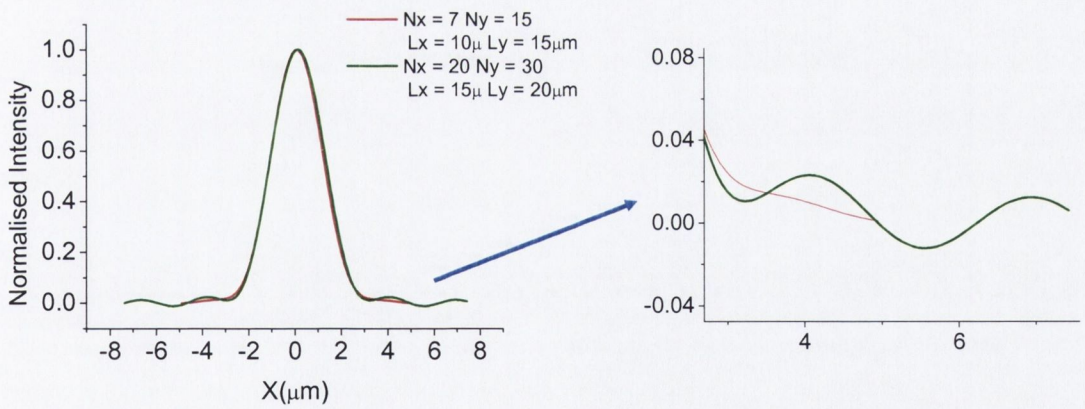


Figure 2-20 Plot of the E_{12} mode of a dielectric waveguide with a square core in the xz plane. Inset: shows the oscillation of the field with increasing computational boundary

2.8.2 Finite Difference Method

The final method that will be discussed is the two-dimensional finite difference method, which offers advantages over both the two-dimensional Galerkin's method

and the effective index finite difference method. The finite difference effective index method offers a computationally efficient and accurate means of solution of the two-dimensional wave equation for strongly guided waveguides. When the waveguide becomes weakly guiding in one dimension, as is the case of the lasers described here, the validity of the effective index approximation breaks down. In figure 2-21 we can see that for the lateral carrier density profile shown the effective index step due to the higher refractive index of the cladding over the blocking layers has been reduced such that the magnitude of the effective index under the stripe is equal to that at the boundaries. From this profile it is clear that the mode will no longer be strongly guided and in fact the field spreads out with a large proportion occupying the regions beneath the blocking layers as seen from figure 2-21.

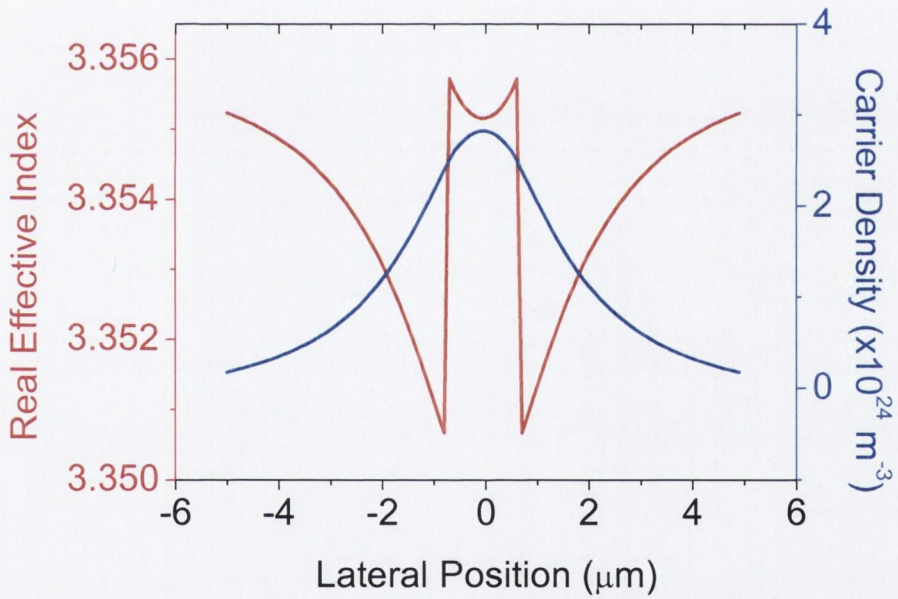


Figure 2-21 The lateral carrier density profile and the corresponding effective index profile used in the comparison of the two methods.

In contrast to the two-dimensional Galerkin method with sine series basis functions, the field profile in the case of the two dimensional finite difference method decays to zero as one approaches the boundaries and increasing the computational window does not show the oscillating behaviour seen with Galerkin's method. Therefore as seen in figure 2-22 the two-dimensional finite difference method is rigorous enough to

provide accurate solutions to the weakly guided complex index guided structures. There is, however, a corresponding significant increase in the computation effort required.

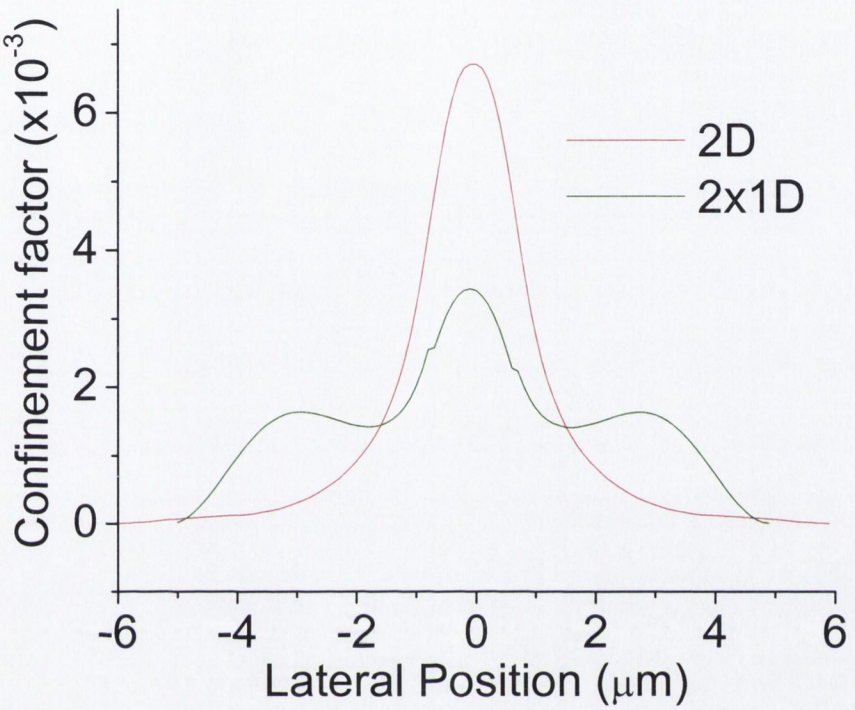


Figure 2-22 Comparing the confinement factors for the effective index method (2x1D) and the (2D) finite difference method for the carrier density profile shown in figure 4-4.

2.9 Conclusions

We have provided a review of some of the more important theoretical concepts that are pertinent in the modelling of complex index guided self-pulsation laser diode.

In particular we have demonstrated that Galerkin's formalism based on a sine series expansion is accurate for strongly guided modes along the transverse or growth direction. This results in an accurate determination of the effective index values. But in the lateral direction where the optical mode is weakly guided the restriction of the waveguide to a finite domain does not ensure that the optical mode decays exponentially towards the boundary. Since the since series basis does not converge to zero at infinity, using a two-dimensional Galerkin's method solution results in an

oscillating field component in the cladding regions of the device. The use of alternative basis such as the Hermite-Gauss functions were considered, but since the integrals can no longer be solved analytically as was the case for the trigonometric basis functions the accuracy of the solution and the computational effort depends on of the numerical integration. The finite difference method is the method of choice for the solution of the 2x1D or effective index method but this also shows erroneous results for weakly guided waveguides. The validity of the finite difference effective index method for waveguides in which the fundamental mode is close to cutoff shall be considered in the next chapter.

References

1 "Solid state physics", N. W. Aschcroft and N. D. Mermin, Saunders College Publishing, 1976.

2 "An improved calculation of the energies of metallic Li and Na", J.Bardeen, J.Chem.Phys. **6,** p 367, 1938.

3 "The Modern Theory of Solids", F. Seitz, New York, p352, 1940.

4 "The Motions of electrons and holes in perturbed periodic fields", J. M. Luttinger, and W. Kohn, Phys. Rev. **97**, p869, 1955.

5 "A note on the quantum-mechanical pertubation theory", P. Löwdin. J.Chem.Phys. **19,** p1396, 1951.

6 "Physics of Optoelectronics Devices", S. L. Chuang, John Wiley & Sons, New York, p144, 1995.

7 "Reduction of the lasing threshold current density by the lowering of valence band effective mass", E. Yablanovitch, and E. O. Kane, J. Lightwave, Technol. **4,** p 504 1986.

8 "Correction to "Reduction of the lasing threshold current density by the lowering of valence band effective mass"" E. Yablanovitch, and E. O. Kane, J. Lightwave, Technol. **4,** p 961, 1986.

9 "Band-structure engineering for low-threshold high-efficiency semiconductor lasers", A. R. Adams, Electron. Lett. **22,** p 249, 1986.

10 "Effects of deformation on the hole energy spectrum of germanium and silicon", G.E.Pikus, and, G.L.Bir, Sov. Phys.-Solid State1, p 1502, 1960.

11 "Symmetry and Strain-Induced Effects in Semiconductors", G.L.Bir and G. E. Pikus, Wiley, New York, 1974.

12 "Efficient band-structure calculations of strained quantum wells", S. L. Chuang, Phys. Rev. B. **43** 12 p 9649, 1991.

13 "Quantum Electronics", S. Yariv, 3rd edition, Wiley, NewYork, 1989.

14 "Phase Dampings of Optical Dipole Moments and Gain Spectra in Semiconductor Lasers", M. Yamanishi, and Y. Lee, IEEE J.Quantum Electron, **23,** p 367, 1987.

15 "Intraband relaxation effects on Optical Spectra in Quantum Well Lasers", M. Asada, ed. P. S. Zory, Jr, Ch 2 Quantum Well Lasers Academic Press, San Diego, 1993.

16 "Lifetime broadening in GaAs-AlGaAs quantum well lasers", A. I. Kucharska, and D. J. Robbins, IEEE. J. Quant, Electron, **26,** p 443 1990.

17 "A model for GRIN-SCH-SQW diode lasers". R. Chinn, P. Zory, and A.R. Reisinger, IEEE. J. Quant. Electron. **24,** p 2191, 1988.

18 "Laser conditions in semiconductors", M. G. A. Bernard, and G. Duraffourg, Phys. Status Solidi **1**, p 699, 1961.

19 "The Feynman Lectures in Physics", R.P Feynman, R. B Leighton, and M. Sands, vols II and III, Adison-Wesley, Reading, Massachusetts. 1963.

20 "Physics of Optoelectronic Devices", S. L . Chuang, Wiley New York, p387, 1995.

21 "Valence Band Parameters in Cubic Semiconductors", P. Lawaetz, Phys. Rev. B **4,** p3460, 1971.

22 "Anomolous Optical Absorption Limit in InSb", E. Burnstein, Phys. Rev. **93,** p632, 1954.

23 "Semiconductor Opto-electronics", T.S. Moss, G. J. Burrell, and B. Ellis, Wiley New York 1973.

24 "Dispersion of the index of refraction near the absorption edge of semiconductors", F. Stern, Phys. Rev A. **133,** p 1653, 1964.

25 "The Carrier-Induced Index Change in AlGaAs and 1.3μm InGaAsP Diode Lasers", J. Manning, R. Olshansky, and C. B. Su. IEEE. J. Quant. Electron. **19,** (10) , p 1525 1983.

26 "Carrier Induced Change in Refractive Index of InP, GaAs, and InGaAsP", B. R. Bennett, R. A. Soref, J. A. Del Alamo, IEEE. J. Quant. Electron. **26,** (1), p 113, 1990.

27 "Theory of the band structure of very degenerate semiconductors", P. A. Wolff, Phys. Rev. **126,** p 405, 1962.

28 "Spectral Dependence of the change in the refractive index due to carrier injection in GaAs lasers", C. H. Henry, R. A. Logan, and K. A. Bertness, J. Appl. Phys **52,** (7), p 4457, 1981.

29 "Optimisation of the carrier-induced effective index change in InGaAsP waveguides-application to tunable Bragg Filters", J. P. Weber, IEEE. J. Quant. Electron. **30,** (8), p 1801, 1994.

30 "Statistics of the recombinations of holes and electrons", W. Shockley, and W. T. Read, Jr., Phys. Rev. **87,** p 835, 1952.

31 "Electron-hole recombination in Germanium", R. N. Hall, Phys. Rev, **87** p387, 1952.

32 "Diode Lasers and Photonic integrated Circuits", L. A. Coldren and S. W. Corzine, Wiley, New York, 1995.

33 "Reflectivity of TE Modes at the Facets of Buried Heterostructure Injection Lasers", IEEE. J. Quant. Electron **22** (4) 1986.

34 "Quantum Well Lasers" P. S. Zory, Academic Press, 1993.

35 "Confinement and Modal Gain in Dielectric Waveguides", T. D. Visser, B. Demeulenaere, J. Haes, D. Lenstra, R.Baets, and H. Blok J. Lightwave. Tech. **14,** (5), p 885, 1996.

36 "Modal Analysis of a Planar Waveguide with Gain and Losses", T. D. Visser, H. Block, and D. Lenstra, IEEE J Quantum Electron. **31,** (10), p 1803, 1995.

37 "A Vector Galerkin's Method Based on E Fields", Sung-Yuen Wang, Wei-Yu Lee and Shung-June Hwang, IEEE Photon. Technol. Lett. **5**, (5), p 1439, 1993.

38 "Optical Waveguide Modes: An approximate solution Using Galerkin's Method with Hermite–Gauss Basis Functions", Robert L.Gallawa, I.C. Goyal, Yinggang Tu, and Ajoy K.Ghatak, IEEE J. Quantum Electron. **27,** (3), p 518, 1991.

39 "Vector and Quasi-Vector Solutions for the Optical Waveguide Modes Using Efficient Galerkins Method with Hermite-Gauss Basis Functions", A. Weisshaar, J.Li, R.L.Gallawa, and I. C. Goyal, IEEE J Lightwave Tech. **13,** (8), p 1795 1995.

40 "Field Computations in Engineering and Physics", A. Thom, and C. J. Apelt, D. Van Norstrand, London, 1961.

41 "Theory of Dielectric Optical Waveguides", 2nd Ed, Dietrich Marcuse. Academic press, New York, 1991.

42 "Dielectric rectangular waveguide and directional coupler for integrated optics", E. A. J. Marcatili. Bell. Syst. Tech. J. **48,** (7), p 2071 1969.

Chapter 3 Self-Pulsation Dynamics

3.1 Introduction

Some of the earliest attempts to model the dynamics of self-pulsation for narrow stripe semiconductor were based on coupling three rate equations [1]. These describe the evolution of the carrier density within the gain and absorbing layers as two separate sections and the final rate equation described the photon evolution with time. Although these models produced some insight into the mechanisms of self-pulsation they failed to provide any spatial information of the laser diode. As a result of this the self-pulsation mechanism was understood solely in terms of the saturable absorption as a result of the photo-generation of carriers in the absorber section. Later [12] a spatial model was developed in which the diffusion between sections could be treated more rigorously but the optical field was assumed to be stationary throughout the calculation. It was in a subsequent paper [13], that the same author realised that in order to provide a quantitative description of the self-pulsation mechanism both a spatial carrier and optical field time varying model was required and this chapter is modelled on that that principle.

This chapter will give a description of the key components that need to be included within the simulation. In what follows the effects of current spreading underneath the current blocking layers, ambipolar diffusion, the discretisation of the active region as well as the threshold current determination will be discussed. Upon that basis the spatial and temporal dynamics will be shown, giving insights to the model and the limitations of the effective index approximation for the determination of the optical field.

3.2 Current Spreading

The current blocking layer within the structures presented does not extend to the active region. There is a region underneath which, the current may spread out laterally. This has important consequences for the carrier distribution within the active layer. Current spreading through carrier drift and diffusion in semiconductor lasers plays an important role in the determination of threshold current densities and lateral gain and carrier profiles. An effective model is required to determine the parameters within the structure that affect the current and carrier profiles. For this purpose there are many models that have been suggested to describe the behaviour of current flow, current spreading and carrier diffusion within the active region [2][3][4]. As shown in [5] for the double-heterostructure stripe geometry, in which the current is guided through a Zn diffused cap or equivalently through the use of current blocking layers, there is excellent agreement between the original analytical model proposed by Yonezu [1] and more complex self-consistent models in which the current flow is coupled to the carrier diffusion and the solution of Laplace's equation is performed through the use of finite element triangulation. For structures in which the current is not guided through blocking layers the method shows erroneous results for the junction current density as a result of the invariance in conductivity for the superstrate and upper cladding layers.

For the structure shown in figure 3-1, we assume that the combined thickness of the current spreading layer d_p and the active layer thickness d_a are much less than the stripe width, then the total current I_t is shown to be the sum of the uniform current under the stripe I_e, and the spreading current I_0, flowing to each side of the stripe region:

$$I_t = I_e + 2I_0 \tag{3.1}$$

The current across the junction between y and y + dy is

$$-dI_y = LJ_s\left(e^{\beta V_y} - 1\right)dy \tag{3.2}$$

Where J_s is the saturation current density, and $\beta = \frac{q}{nk_bT}$ is the exponential junction parameter, with n = 2 as the typical experimental value [6][7].

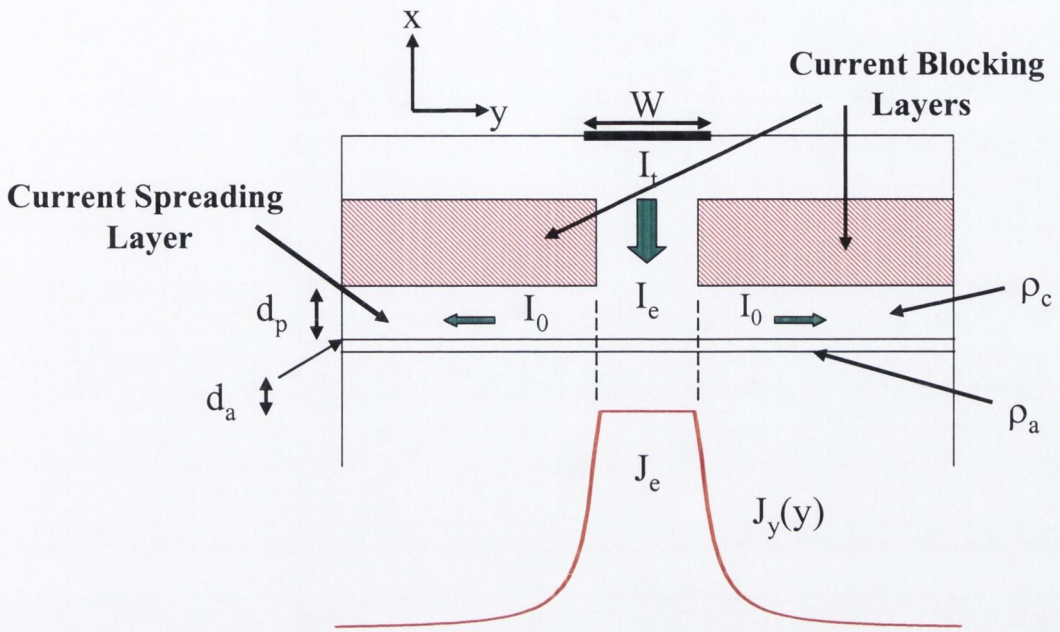


Figure 3-1 Schematic representation of current spreading in a contact stripe geometry laser with current blocking layers

V_y is the junction voltage at y, where q, k_b and T, denotes the electron charge, Boltzmann's constant and the temperature respectively. The voltage drop across the current spreading and active layers is given by

$$-dV_y = \rho_s I_y dy \tag{3.3}$$

where ρ_s is the composite sheet resistivity given by:

$$\frac{1}{\rho_s} = \frac{d_p}{\rho_c} + \frac{d_a}{\rho_a} \tag{3.4}$$

Since at 300K and depending on the junction voltage at y, $\beta V_y \approx 5\times10^2$, then $e^{\beta V_y} \gg 1$ in equation (3.2) we can obtain the following differential equation by combining equation (3.2) and (3.3)

$$\frac{d^2 I_y}{dy^2} = -\beta \rho_y I_y \frac{dI_y}{dy} \tag{3.5}$$

After a little manipulation it can be shown as in Appendix A of [2] that the current density across the junction is given by

$$J_y(y) = \frac{I_0}{l_0 L}\left[1 + \frac{\left(|y| - \frac{W}{2}\right)}{l_0}\right]^2 \tag{3.6}$$

where $l_0 = \frac{2L}{\beta \rho_s I_0}$ can be considered the characteristic length of the current density profile and the spreading current I_0 is taken as the positive solution of

$$I_0 = \frac{\left[1 + \left(\frac{W \beta \rho_s}{2L}\right) I_t\right]^{\frac{1}{2}} - 1}{\left(\frac{W \beta \rho_s}{2L}\right)} \tag{3.7}$$

As can be seen from equation (3.4) the layer with the smallest $\frac{\rho}{d}$ ratio determines within which layer the majority of the current will flow. Therefore the current spreading layer of thickness d_p will dominate the spreading. Figure 3-2 shows the increase in current spreading as the thickness of the current spreading layer increases from d_p = 0.05μm to 0.20μm. The resistivity of the active layer (ρ_a) and current spreading layers (ρ_s) are taken to be 0.002Ωm.

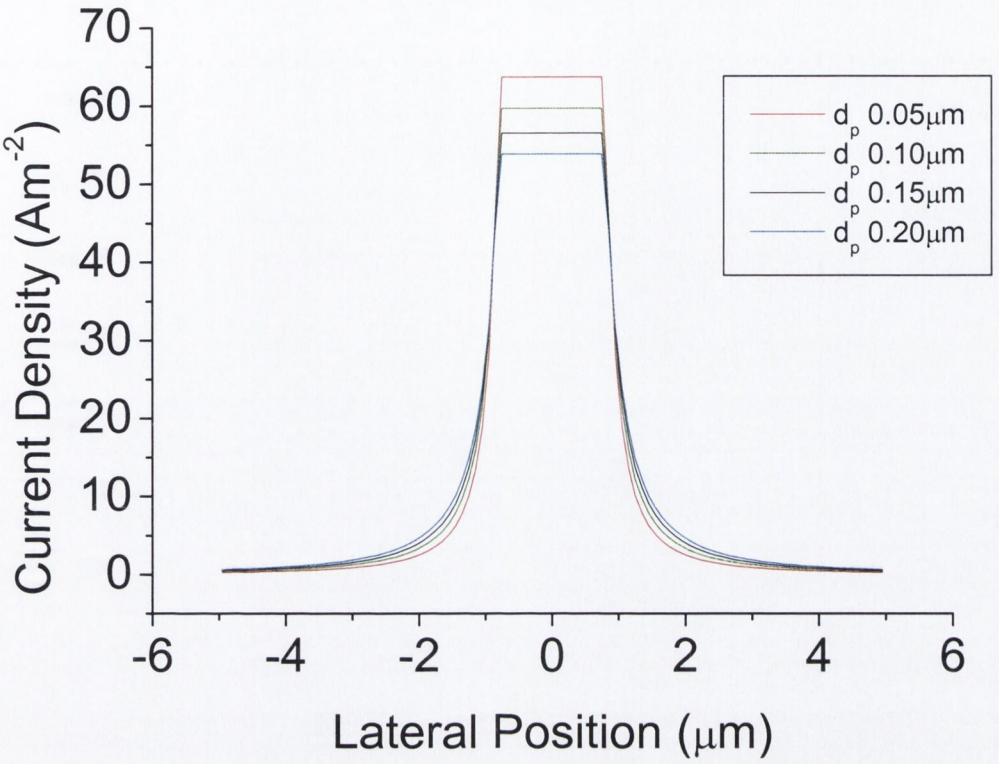


Figure 3-2 Illustration of the current density variation with spreading layer thickness dp for I_t = 35mA. The spreading current I_0 ranges between 4.8mA for dp = 0.05μm, to 6.7mA for dp = 0.20μm. Correspondingly, the characteristic length l_0 ranges between 0.3μm for dp = 0.05μm, and 0.5μm for dp = 0.20μm.

3.3 Ambipolar Diffusion

Certain approximations are only valid in the regime of a current confined structure such as those discussed here. The justification for the use of an ambipolar diffusion term describing collectively, the electron and hole drift and diffusion will be outlined in the following. For double-heterostructure devices the conventional use of the diffusion equation to describe the lateral carrier motion in the active layer has been brought into question [8] because of a seemingly neglected drift term. From what will follow the justification for this approximation for the specific case of a structure incorporating n-doped current blocking layers will be outlined.

Based on the derivation given in [9] the active layer current density J_n can be written as

$$J_n = q\mu_n E + qD_n \nabla N \tag{3.8}$$

where E represents the active layer drift field, the electron mobility is denoted by μ_n, the electron diffusion coefficient D_n is given by

$$D_n = \frac{\mu_n s(u)}{q} k_b T \tag{3.9}$$

This is the degenerate Einstein relation in which s is the degeneracy factor and $u = \frac{N}{N_c}$ where N is the electron density and N_c represents the effective density of states for the conduction band. The lateral voltage drop in the p-doped spreading layer is very much larger than the drop in voltage across the n-doped cladding layer lying beneath the active region because of the following design features that are applied. The use of a thin current stripe with widths typically around 1.5μm, highly p-doped layer resistivity compared to that of the n-doped layer, and thin spreading layer thickness in comparison to the n-doped cladding layer thickness. Typical values for the p-doped current spreading layer thickness and the n-doped cladding layer thickness are 0.15μm and 1.5μm respectively. It is therefore a reasonable approximation to neglect the lateral voltage drops in the n-doped cladding layer i.e. the electron Fermi-level E_{fn} is assumed to be flat. This requires that

$$J_n = \mu_n N \nabla E_{fn} = 0 \tag{3.10}$$

The active layer electrons are stationary due to the effect of the large active layer drift field E overcoming the electron diffusion, thus

$$E = -\frac{D_n}{\mu_n}\frac{\nabla N}{N} = -s(u)\frac{k_b T}{q}\frac{\nabla N}{N} \tag{3.11}$$

The hole concentration P in the active layer is governed by an analogous set of equations to (3.10), (3.8) and (3.9) giving,

$$J_p = -\mu_p P \nabla E_{fp} = q\mu_p PE - qD_p \nabla P \tag{3.12}$$

Substituting equation (3.11) into (3.12) and assuming $N = P$ (charge neutrality in the undoped active region) yields

$$J_p = -qD_e \nabla P \tag{3.13}$$

where the effective diffusion coefficient is given by

$$D_e = \mu_p \left(\frac{D_p}{\mu_p} + \frac{D_n}{\mu_n} \right) = \frac{2k_b T \mu_p \langle s \rangle}{q} \tag{3.14}$$

where the mean degeneracy factor is given by

$$\langle s \rangle = \frac{1}{2}\left[s(u) + s(v) \right] \tag{3.15}$$

$v = \dfrac{P}{P_c}$ where, P is the hole density and P_c represents the effective density of states for the valence band. We can see that the effective diffusion coefficient derived here differs from the ambipolar diffusion constant D_a where

$$D_a = \frac{\left(\frac{D_p}{\mu_p} \right) + \left(\frac{D_n}{\mu_n} \right)}{\left(\frac{1}{\mu_p} \right) + \left(\frac{1}{\mu_n} \right)} = \frac{2k_b T}{q} \frac{\langle s \rangle}{\left(\frac{1}{\mu_p} \right) + \left(\frac{1}{\mu_n} \right)} \tag{3.16}$$

The degree to which there is a discrepancy between the effective and ambipolar diffusion depends on the relationship between the magnitudes of electron mobility μ_n to hole mobility μ_p. We find that for a laser operating at a wavelength of 780nm the active layer is composed of $Al_{0.14}Ga_{0.86}As$. In this particular case the electron mobility $\mu_n = 0.5116 m^2 V^{-1} s^{-1}$ and $\mu_p = 0.02487 m^2 V^{-1} s^{-1}$ [10]. Therefore for this case we can consider

$$\left(\frac{1}{\mu_p} \right) + \left(\frac{1}{\mu_n} \right) \cong \frac{1}{\mu_p} \tag{3.17}$$

where equation (3.16) reduces to (3.14). Thus for the specific case of a P-on-N device incorporating current blocking layers and a relatively conductive n-doped cladding layer $D_a \approx D_e$. That is, for current spreading in thin current stripe lasers incorporating current blocking where $d_p \ll W$, one can use for this special case, not only the ambipolar diffusion equation but also the degenerate ambipolar diffusion coefficient D_a. This approximation frees us from the need to have separate equations describing the dynamics of holes and electrons within the active region.

Determination of the threshold carrier profile in the active region incorporating these newly defined quantities, the lateral dependent current density $J(y)$ and the ambipolar diffusion constant D_a is now possible. Since at threshold current, the rate of loss of carriers due to stimulated emission is much less than that lost through spontaneous emission, we may neglect the stimulated emission term from our determination of the threshold carrier profile. Also, by applying the steady state condition

$$\frac{dN}{dt} = \frac{dS}{dt} = 0 \tag{3.18}$$

we arrive at the carrier density equation

$$\frac{dN}{dt} = \frac{J(y)}{qd_a} - R_{sp}(y) - \frac{N(y)}{\tau_{nr}} + D_a \frac{\partial^2 N}{\partial y^2} = 0 \tag{3.19}$$

The first term on the right hand side represents the rate of injection of carriers per unit volume into the active region where q represents the electron charge and d_a the active layer thickness. The second term represents the rate of loss of carriers per unit volume due to spontaneous emission, the third accounts for the loss of carrier through non-radiative recombination and the fourth term represents the ambipolar diffusion within the active region. In order to solve for the lateral carrier density profile we first divide the active regions into sections where the carrier density is considered constant in each section. As has been described in the section on discretisation of the second order differential wave equation the diffusion term can be approximated as

$$\frac{\partial^2 N}{\partial y^2} = \frac{\left(N(i-1) - 2N(i) + N(i+1)\right)}{\Delta^2} \qquad (3.20)$$

The active layer section thickness is represented here by Δ.

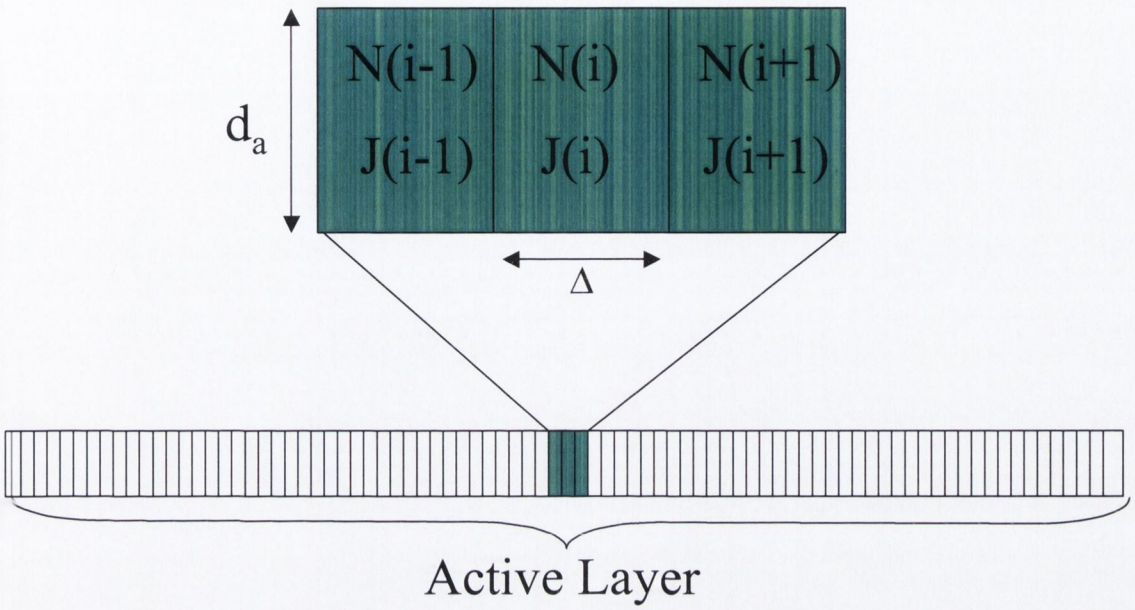


Figure 3-3 Schematic showing the division of the active regions into equally spaced sections of thickness Δ. Within each section the carrier density and current density are considered constant.

Since $R_{sp}(i)$ is carrier density dependent, unless an initial estimate for the carrier density profile can be found $R_{sp}(i)$ cannot be estimated accurately. To this end we will as an initial approximation, use a constant spontaneous (carrier independent) lifetime τ_s = 1.3ns to determine the first initial profile. Then, using this profile, R_{sp} can be calculated within each section. This sequence is iterated until the carrier density profile converges. Since each section in the active region is coupled to its nearest neighbour through the diffusion term (3.20) we can now set up a tri-diagonal equation in order to solve for the carrier density profile.

$$\begin{pmatrix} b & c & 0 & . & . & 0 \\ c & b & c & 0 & . & . \\ 0 & c & . & . & . & . \\ . & 0 & . & . & . & 0 \\ . & . & . & . & b & c \\ 0 & 0 & 0 & 0 & c & b \end{pmatrix} \begin{pmatrix} N_1 \\ N_2 \\ . \\ N_i \\ . \\ N_n \end{pmatrix} = \begin{pmatrix} J_1 \\ J_2 \\ . \\ J_i \\ . \\ J_n \end{pmatrix} \qquad (3.21)$$

where,

$$b = \left(\frac{1}{\tau_s} + \frac{1}{\tau_{nr}} + \frac{2D_a}{\Delta^2} \right) \tag{3.22}$$

and

$$c = -\frac{D_a}{\Delta^2} \tag{3.23}$$

This method allows the determination of the carrier density profile across the active region for a current I_t where $I_t \leq I_{th}$ (threshold current).

3.4 Threshold current determination

We will define the threshold current as that current that produces a carrier density profile in the active region such that the modal gain balances the modal losses within the cavity, that is

$$G - G_{th} = 0 \tag{3.24}$$

where

$$G = \frac{\iint_{Active} g|\phi|^2 \, dxdy}{\iint_{Total} |\phi|^2 \, dxdy} \tag{3.25}$$

The two-dimensional electric field is represented by ϕ, g is the material gain within the active region, $\iint_{Active} dxdy, and \iint_{Total} dxdy$ denote the area integration over the active region and total cross sectional area respectively. If we consider the fraction of the optical field intensity in one of the active layer sections denoted as i as seen in figure 3-3, then we can define the confinement factor for that section. The confinement factor for a specific active region section i can be represented by $\Gamma(i)$ where

$$\Gamma(i) = \frac{\int_{Active} \int_{x_l(i)}^{x_{up}(i)} |\phi|^2 \, dxdy}{\int_{Total} |\phi|^2 \, dxdy} \tag{3.26}$$

The modal gain in equation (3.25) can then be approximated as

$$G = \sum_{i=1}^{m} \Gamma(i) g(i) \tag{3.27}$$

where $g(i)$ represents the material gain in the ith section. Here we assume that the active region is divided into m sections. The threshold modal gain can be broken into, losses through the facets, free carrier absorption and absorption into the GaAs substrate. G_{th} can then be expressed as

$$G_{th} = \frac{1}{2L} \ln\left(\frac{1}{R_f R_r}\right) + \frac{\iint_{Active} (c_n + c_p) N |\phi|^2 \, dxdy}{\iint_{Total} |\phi|^2 \, dxdy} + \frac{\iint_{GaAs} \alpha_0 |\phi|^2 \, dxdy}{\iint_{Total} |\phi|^2 \, dxdy} \tag{3.28}$$

c_n and c_p are the free carrier absorption constants and α_0 is the bulk absorption coefficient in GaAs [11]. A flow chart outlining the numerical procedure in the determination of the threshold current for the device is presented in figure 3-4. Firstly an initial carrier profile is obtained from approximating the loss of carriers through spontaneous emission with the use of a spontaneous emission lifetime τ_s. Using this initial carrier profile $N(i)$, the spontaneous emission for each section $R_{sp}(i)$ can be determined. The tri-diagonal equation (3.21) is again solved this time adjusting equation (3.22) to

$$b = \left(\frac{R_{sp}(i)}{N_{old}(i)} + \frac{1}{\tau_{nr}} + \frac{2D_a}{\Delta^2}\right) \tag{3.29}$$

This process is repeated until the difference between the present and past profiles is less than a prescribed error ε (typically $\varepsilon = 1.0 \times 10^{-6}$).

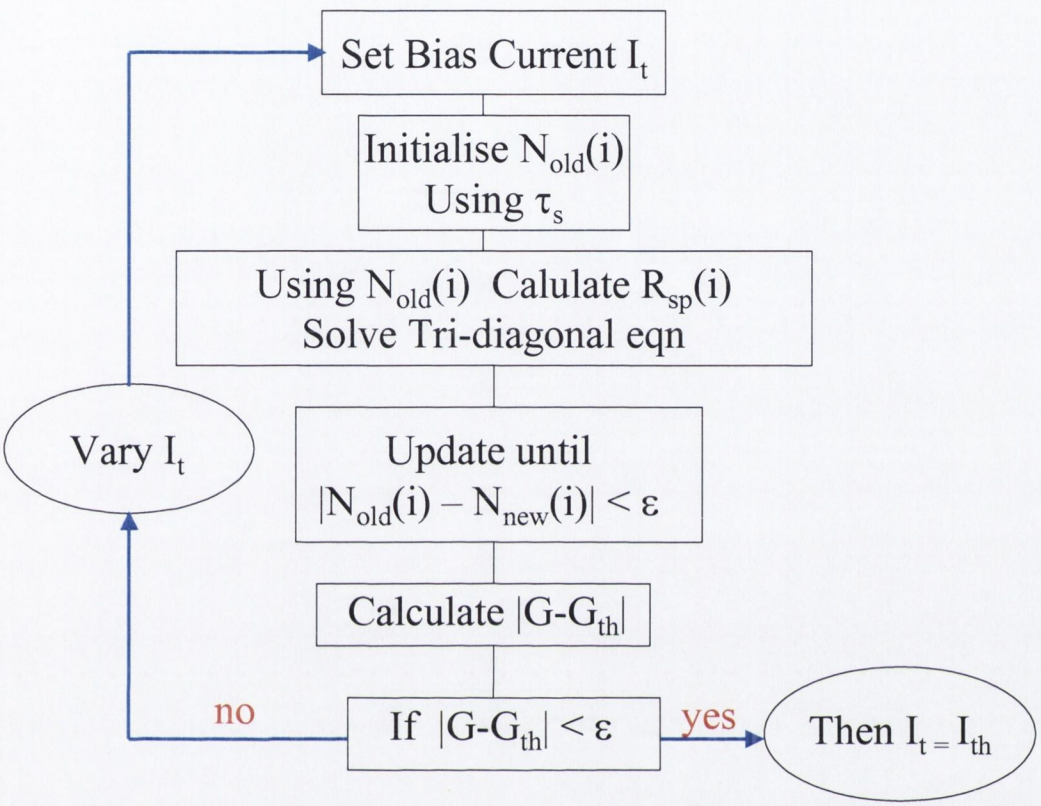


Figure 3-4 Flow chart for the determination of the carrier density profile for a given bias current It, the current is then varied until the threshold condition has been reached

Symbol	Description	Value	Unit
L	Device Length	250	μm
W	Stripe Width	1.4	μm
d_a	Active Region Width	0.06	μm
d_p	Spreading Layer Width	0.15	μm
ρ_a, ρ_c	Active and Cladding Layer Resistivity	$2x10^{-3}$	Ωm
β	Spontaneous Emission Factor	$1.5x10^{-5}$	
D_{ab}	Ambipolar Diffusion	$1.7x10^{-3}$	m^2s^{-1}
τ_{nr}	Non-Radiative Recombination Lifetime	8.0	ns
c_n	Electron Free-Carrier Absorption Constant	$3.0x10^{-22}$	m^2
c_p	Hole Free-Carrier Absorption Constant	$7.0x10^{-22}$	m^2
X_b	Blocking Layer Aluminium Mole Fraction	0.6	
X_c	Cladding Layer Aluminium Mole Fraction	0.5	
X_a	Active Layer Aluminium Mole Fraction	0.14	
R_f, R_r	Front and Rear Facet Reflectivity	0.3	
α_{GaAs}	GaAs Absorption Coefficient	$1.0x10^{6}$	m^{-1}
n_g	Group Refractive Index	3.6	

Table 3-1 Table of the parameters used within the AlGaAs device that is used in chapter 3 and chapter 4 with the exception of the current stripe width (W) and the Al mole fraction (X_b) in the blocking layer.

The bias current is then varied until the difference between the modal gain and losses is within a defined error ε. Once the threshold current and carrier profile are determined for a structure we can study the dynamics of the device. In order to do this we will define the carrier density and photon number rate equations based on [12] and [13].

$$\frac{dN(i)}{dt} = \frac{J(i)}{qd_a} - R_{sp}(i) - \frac{N(i)}{\tau_{nr}} + D_a \frac{\left(N(i-1) - 2N(i) + N(i+1)\right)}{\Delta^2} - \frac{c}{n_g} \frac{g(i)\Gamma(i)S}{V_a} \tag{3.30}$$

In a similar way to equation (3.19), the carrier density in each section is coupled to its nearest neighbour through the diffusion term. It is also coupled to the photon population in the cavity through the stimulated emission term (final term on the right hand side). The group refractive index is denoted by n_g. The confinement factor (sometimes referred to as the filling factor) in each section is defined in equation (3.26). The evolution of the number of photons S within the laser cavity is described by the following rate equation

$$\frac{dS}{dt} = \frac{c}{n_g}(G - G_{th})S + \beta V_a \iint_{Total} R_{sp} |\phi|^2 \, dxdy \tag{3.31}$$

The second term on the right hand side takes into the account the fraction of spontaneous emission that is coupled into the lasing mode, where β denotes the spontaneous emission factor. For uniform coupling to all modes it is just the reciprocal of the number of optical modes in the bandwidth of the spontaneous emission [14]. If the active region is divided into n sections then the solution of equation (3.30) and (3.31) requires the solution of n+1 ordinary differential equations. Since these equations are coupled, it is important when considering numerical methods of solution to consider that the error introduced in incrementing each equation over a time step d_t, must be calculated for each equation and the time step should be adjusted to meet the specific fractional error applied by the worst case. Other considerations, such as, the safeguarding against the accumulation in global errors is described further in [15]. The numerical scheme that has been used to meet the requirements is the fourth order Runge-Kutta driver with adaptive stepsize control. In the earliest models describing self-pulsation the optical field was assumed to be constant at its threshold value [12]. Later it was shown by the same group [13] that the assumption that the optical field is unchanged at its threshold value is not precise enough to simulate the self-pulsation phenomenon quantitatively. The need therefore to update the field profile during the course of the simulation is central to obtaining a quantitative self-pulsation simulation.

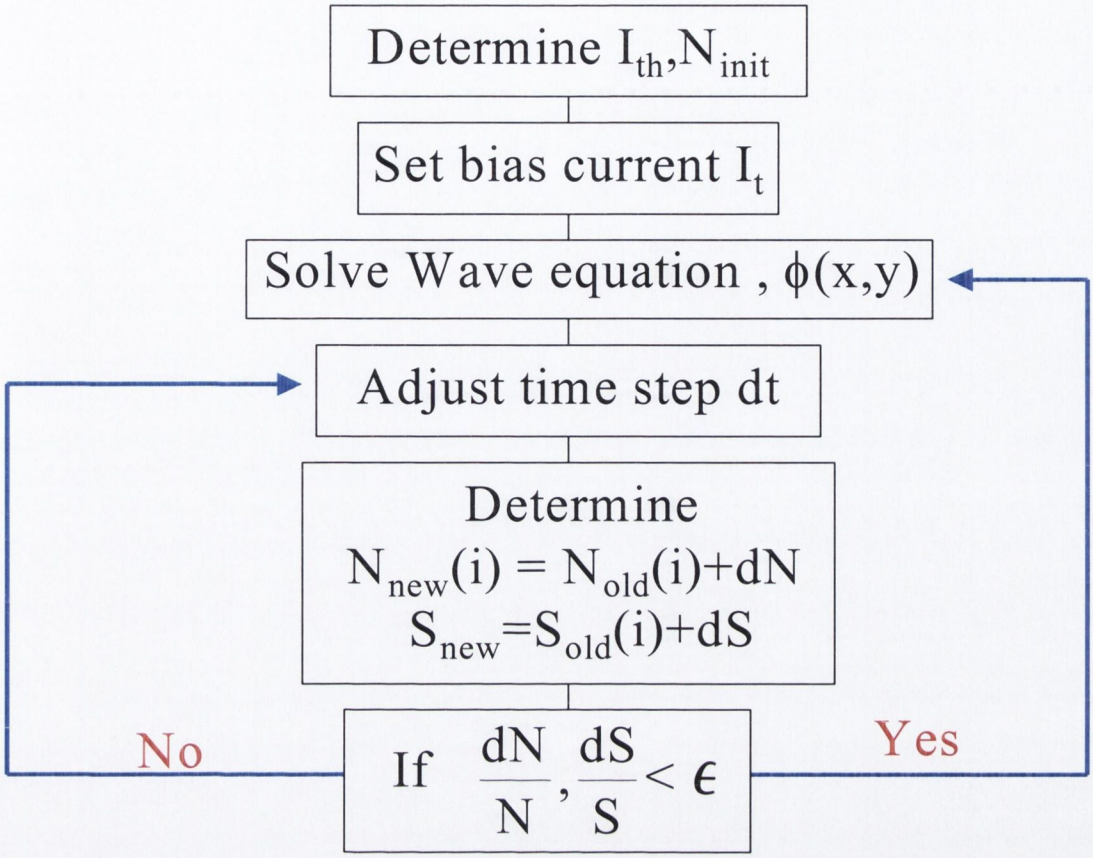


Figure 3-5 Flow chart showing the sequence of calculations for the carrier and photon equations

Since the width of a typical pulse is ~ 20ps. The electric field profile is updated on the order of 1ps. The flow chart in figure 3-5 illustrates the sequence of calculations and the important adaptive stepsize control. The optical power output from the front facet is simply the energy loss rate through the front mirror multiplied by the photon number within the cavity [16].

$$P = \frac{c}{n_g} \frac{\frac{1}{2}\ln\left(\frac{1}{R_f R_r}\right)}{1+\sqrt{\frac{R_f}{R_r}}\left(\frac{1-R_r}{1-R_f}\right)} \frac{hcS}{\lambda} \tag{3.32}$$

R_f and R_r represent the front and back facet reflectivity respectively, and λ represents the lasing wavelength. For our case $R_f = R_r = 0.32$ then,

$$1+\sqrt{\frac{R_f}{R_r}}\left(\frac{1-R_r}{1-R_f}\right)=2 \tag{3.33}$$

and as expected half of the output power is emitted through the front facet.

3.5 Self-Pulsation by Design

Now that the numerical procedure and methods have been outlined it is possible to examine more closely the self-pulsation mechanism and how to design a laser based on these principles. The narrow stripe self-pulsation laser diode has become the most widely available self-pulsation lasing device due to its application in optical-disc systems. The principles of the device design are a narrow current stripe, current blocking layers and a bulk active region. The narrow stripe width W < 3μm and the position of the n-doped blocking layer are designed so as to channel the current entering the active layer, so that there is a large variation in current density as one moves from the edge of the stripe region to the region under the current blocking layer. As a result of this, the carrier density profile decreases below its transparency value in the region under the current blocking layer. If the optical field overlaps this region then an absorption region is created. As we will later learn this is one of the prerequisites for obtaining self-pulsation in these types of devices. To ensure that the optical field overlaps these modal absorption regions it is necessary that the index guiding in the lateral direction is weak. Thus through device design the lasing mode will be amplified in the region under the stripe and suffer losses in the region over the current blocking layers. The key parameters that need to be controlled are the amount of current spreading into the regions under the current blocking layers and secondly the width of the two dimensional field and the degree to which it overlaps the absorption regions. The earliest of the narrow stripe self-pulsation laser designs employed n-doped GaAs blocking layers to channel the current into the active region. Although the use of GaAs as the blocking layer material does not effect the guiding of the current into the active region, limitations are imposed on the spreading of the optical field into the lateral regions. Since GaAs has a smaller bandgap compared to that of the $Al_{xa}Ga_{1-xa}As$ active region the lasing light is absorbed in the GaAs blocking layers. Due to this large band gap difference the refractive index of the GaAs layer is larger than that of the cladding. This means that in order to maintain a weakly guided

device it was necessary to have a wider current spreading layer d_p and stripe width W (see figure 3-7).

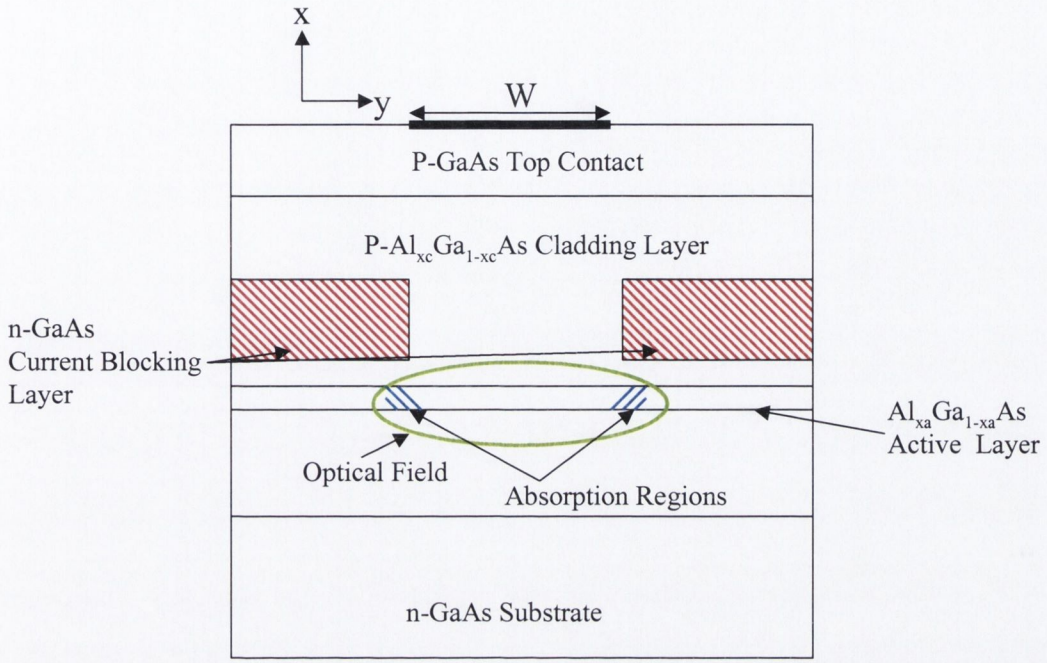


Figure 3-6 Schematic of the self-pulsation structure incorporating an n-doped GaAs blocking layers

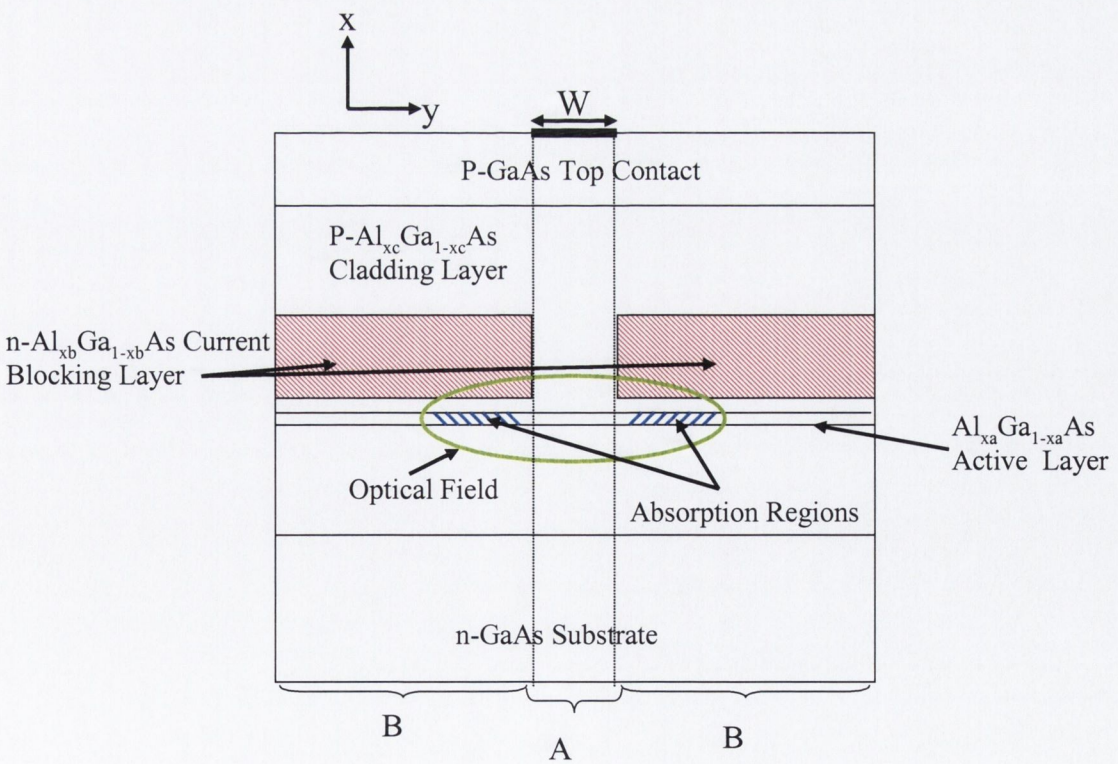


Figure 3-7 Schematic drawing of the narrow stripe AlGaAs/GaAs laser structure incorporating an n-doped $Al_{xb}Ga_{1-xb}As$ blocking layer. The overlap of the optical field into the regions under the stripes create absorption regions

This increase in the current spreading layer thickness d_p results in less current entering the gain region under the current stripe resulting in an increase in the threshold current. Improvements over the use of the GaAs blocking layer have been outlined in [17] in which the use of $Al_{xb}Ga_{1-xb}As$ was used as the blocking layer material. It is important that the aluminium fraction in the blocking layer is slightly higher than that of the absorbing layer (xb > xc) since this leads to an effective index step in the lateral direction. As the optical field is no longer absorbed in the blocking layer this leads to decrease in the threshold current of the device and a wider self-pulsation operating current range. For this type of structure the blocking layers are transparent to the lasing light, thus allowing the light to spread laterally as seen in figure 3-7. Since the band gap difference between the cladding layer and that of the blocking layer is less than that for the GaAs case, it is possible to reduce the width of the current spreading layer while maintaining weak lateral guiding. The use of the $Al_{xb}Ga_{1-xb}As$ blocking layers allows one to control the lateral guiding and current spreading independently. To illustrate the effect of the variation in xb on the lateral waveguiding it is useful to employ the use of the effective index method. For this purpose the waveguide can be broken into two sections, A the pumped five epitaxial layer region under the current stripe and B, the seven epitaxial layer region under the blocking layers (see figure 3-8). For each of the n lateral sections the one-dimensional wave equation is solved in the transverse direction. An equivalent one-dimensional waveguide is then formed in the lateral direction from the effective propagation constants. Since the current blocking layer has a lower refractive index than that of the cladding, an effective index step is formed in the lateral direction. By varying the aluminium fraction xb this step can be varied as can be seen from figure 3-8.

Blocking Layer Al fraction xb	Effective Index Step
0.55	3.7×10^{-3}
0.6	6.2×10^{-3}
0.7	8.1×10^{-3}

Table 3-2 Effective index step variation with Aluminium mole fraction xb in the blocking layer. The Aluminium mole fraction of the cladding layer xc is set equal to 0.5

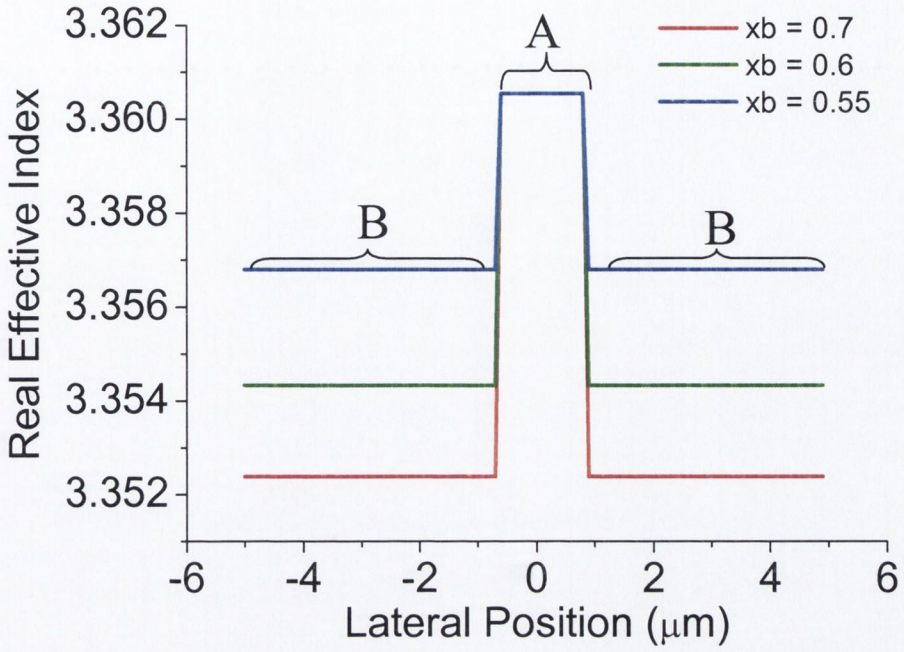


Figure 3-8 Variation in the effective index step in the lateral direction in which the cladding layer Aluminium fraction xc = 0.5

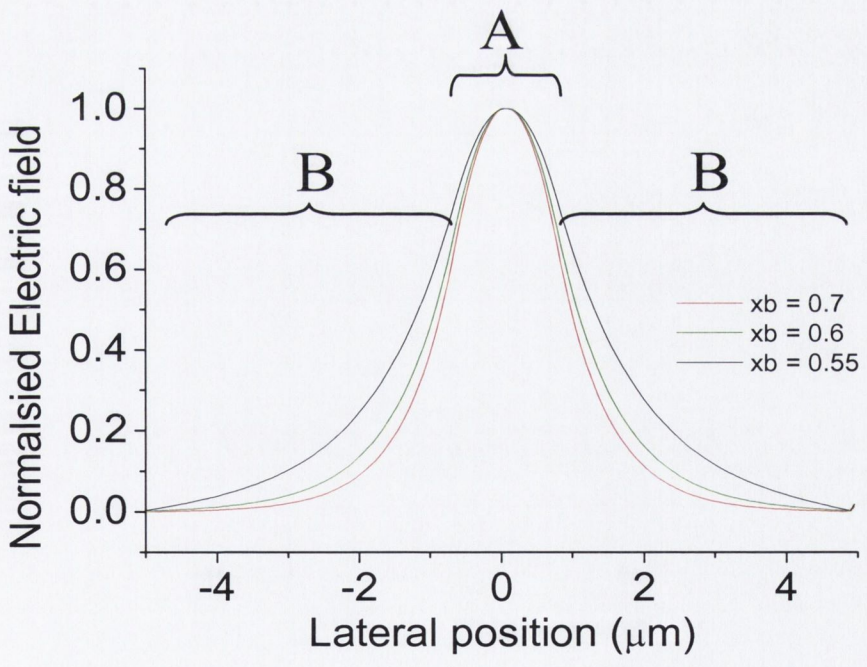


Figure 3-9 Widening of the normalised electric field as the effective index step decreases and the xb value approaches that of xc.

As the aluminium mole fraction of the blocking layer approaches that of the cladding layer the effective index step decreases and as can been seen in figure 3-8, the electric

field spreads into the passive regions beneath the blocking layers. In order to determine the amount of modal absorption that can be achieved for each of the three chosen xb values it is necessary to take into account the effect of carrier density on the refractive index. As has been outlined in the theoretical section the method that is employed to account for the variation in refractive with carrier density in each lateral section $N(i)$ can be expressed as

$$\mathrm{Re}\left(n_{Active}(i)\right) = n_o + \frac{dn}{dN} N(i) \tag{3.34}$$

$$\mathrm{Im}\left(n_{active}(i)\right) = \frac{g(i)}{2k_o} \tag{3.35}$$

n_o represents the refractive index of the active region devoid of carriers. $g(i)$ represents the material gain for section i. The rate of change of the refractive index with carrier density is denoted by $\frac{dn}{dN} = -1.2\times10^{-26}\ m^{-3}$ [18]. This reduction in refractive index due to carrier density has the effect of reducing the transverse electric field confinement and at the same time causing a reduction in the effective index. In order to ensure that the two times one dimensional effective index simulation is as efficient as possible, instead of solving the one dimensional wave equation for the effective index and transverse confinement factor and subsequently solving the lateral effective slab waveguide each time the two dimensional field needs to be calculated. A database was set up so that for a given carrier density the effective index and transverse confinement factor can be interpolated without the need to calculate these for each of the n sections. Figures 3-10 and 3-11 show the reduction in the effective index and transverse confinement factor values with increasing carrier density for both region A under the stripe for which xc = 0.5, and for region B under the current blocking layer.

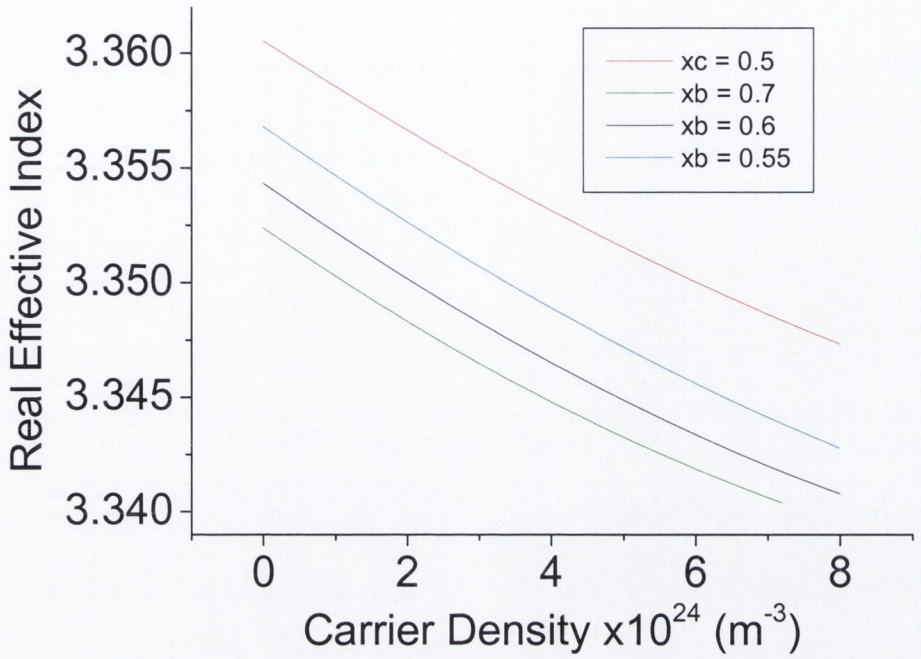


Figure 3-10 Real effective index variation with carrier density in the active region. xc = 0.5 represents the effective index in region A under the current

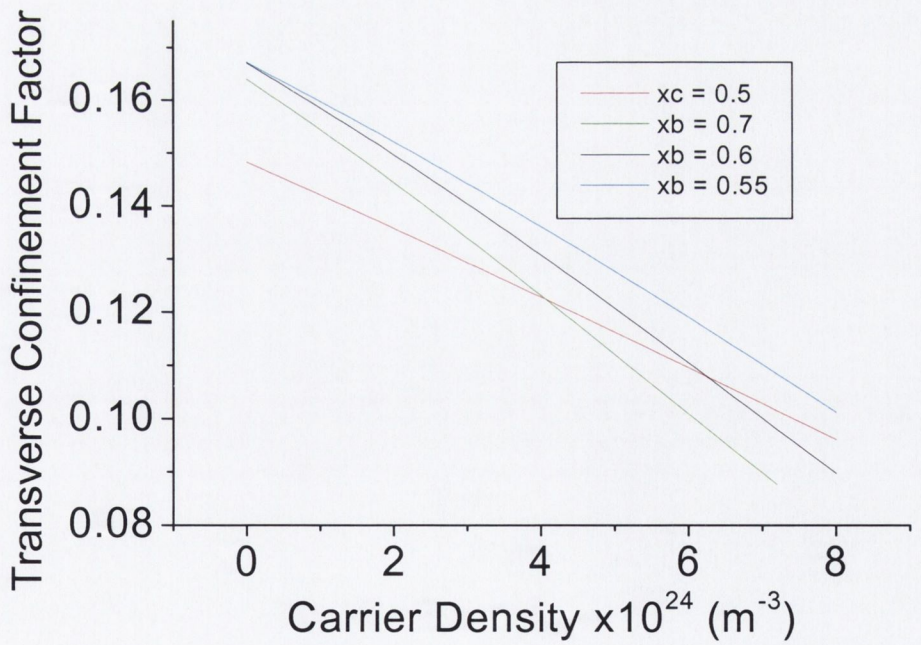


Figure 3-11 Reduction in the transverse confinement factor with increasing carrier density

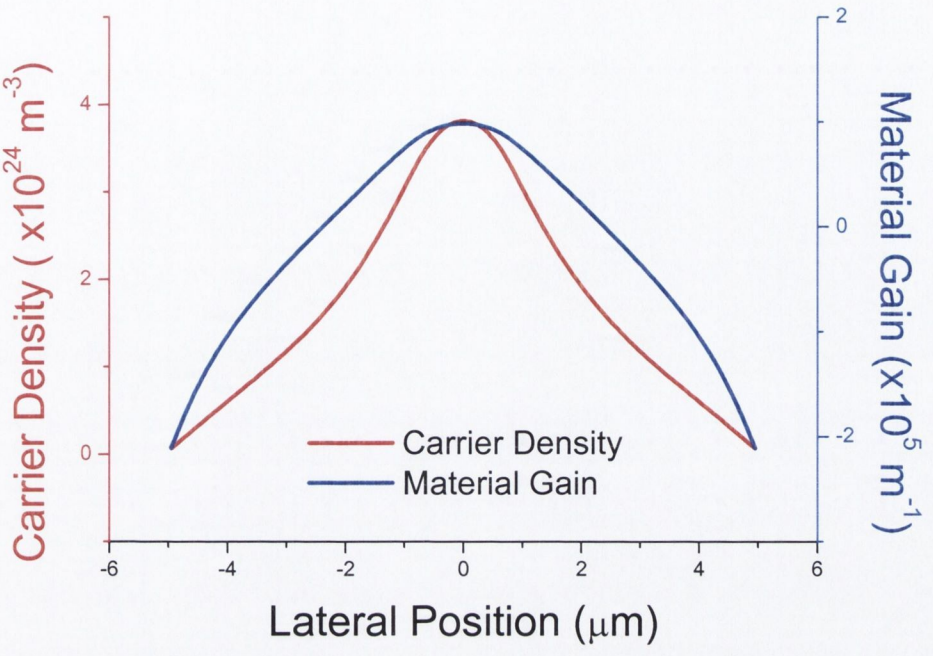


Figure 3-12 Carrier density and material gain profiles across the active region.

W = 1.4μm, d_a = 0.06 μm and d_p = 0.15μm. Bias current = 25mA. The central line indicates the position where the material gain is zero.

In order to determine the material gain profile from the carrier density profile as shown in figure 3-12 we must first determine the lasing wavelength. This is accomplished by first determining the maximum carrier density value. The energy for which the peak gain occurs in the material gain profiles as shown in figure 2-5 represents the lasing energy. Material gain is then determined by interpolating the material gain profiles for the specific carrier density at the lasing wavelength.

The greatest reduction in effective index occurs where the carrier density is highest, under the current stripe. As the carrier density decreases as we move laterally to either side of the current stripe the reduction in the effective index becomes less. These factors combine to create the effective profiles seen in figure 3-13. For the case when no carriers were present the lateral effective index profile was characterised by a effective index step of varying heights according to xb. For these weakly guided structures the effect of carriers reduces what was a central step in region A relative to region B, to one in which the central region lies slightly above the highest effective

index in the side region (xb = 0.7), to being level with in the xb = 0.6um and below for the xb = 0.55 case.

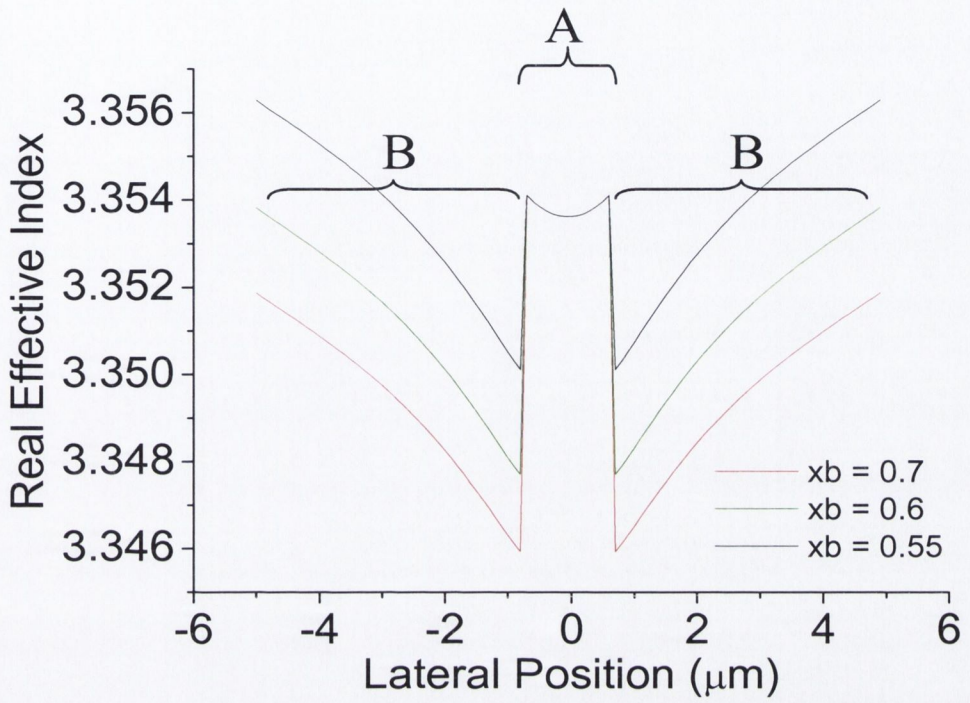


Figure 3-13 The effect of carriers on the lateral effective index profile for three values of aluminium mole fraction in the blocking layer xb

If we consider the effective index profile as a slab waveguide then as the central section A drops below the maximum effective index at the computational edges of the device, this can be viewed as being below cutoff, in analogy to the more simpler one dimensional cases [19]. For the xb = 0.7 case in which the waveguide remains above cutoff, the confinement factor is centred in the central stripe region with a relatively smaller proportion overlapping region B. As the effective index approaches cutoff, as seen in the xb = 0.6 example, a greater proportion of the field overlaps the loss regions reducing the confinement in the centre region A. For the below cutoff case the side lobes form in the side regions creating a regions of high optical confinement in these absorber sections as can been seen in figure 3-14.

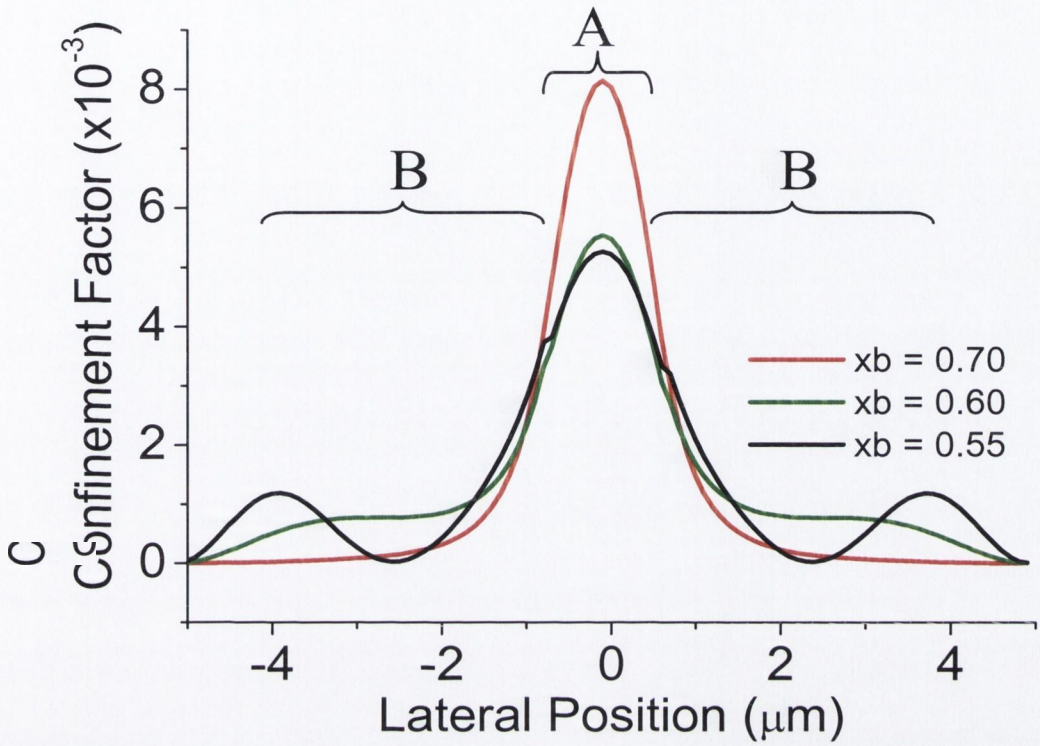


Figure 3-14 Variation in the confinement factor with blocking layer mole fraction xb during the transition from above cutoff (xb = 0.7), at cutoff (xb = 0.6) and below cutoff (xb = 0.55).

As can be seen from figure 3-12 absorption occurs within the active region, below the lateral position of 2.65μm and above 7.35μm, where 0μm represents the leftmost boundary of the lateral waveguide. As we see from the confinement factor in figure 3-14, there is very little overlap of the electric field with the absorber regions for the xb = 0.7 example, as a result no modal absorption in seen in these regions. Similarly as xb drops the field spreads into the absorber sections resulting in a larger proportion of the confinement factor in these regions giving rise to modal absorption as shown in figure 3-15.

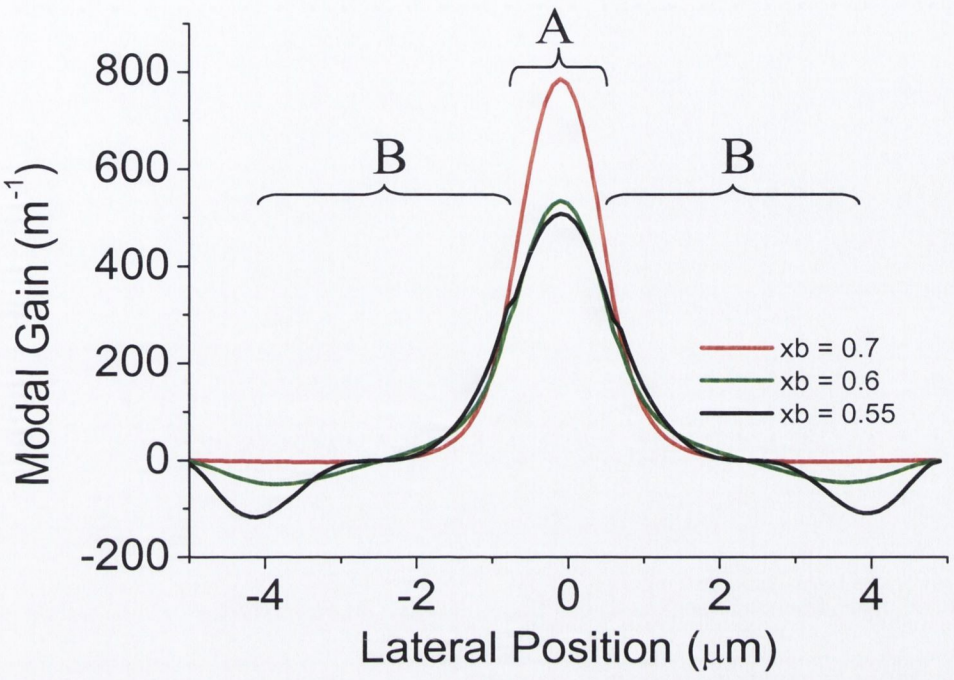


Figure 3-15 Modal gain profile across the active region. Modal absorption is only observed for the xb = 0.55 and xb = 0.6 cases for this carrier density profile.

3.6 Self-pulsation Dynamics

The transient behaviour of the carrier density and the photon number are calculated from (3.30) and (3.31). The optical field and confinement factor are determined at every step of the scheme, which allows the incorporation of the carrier density-dependent optical field. In order to appreciate the differences between self-pulsation and the more familiar transient relaxation oscillations seen in the more typical semiconductor laser it is quite informative to first consider a narrow stripe device in which the lateral optical field is strongly guided.

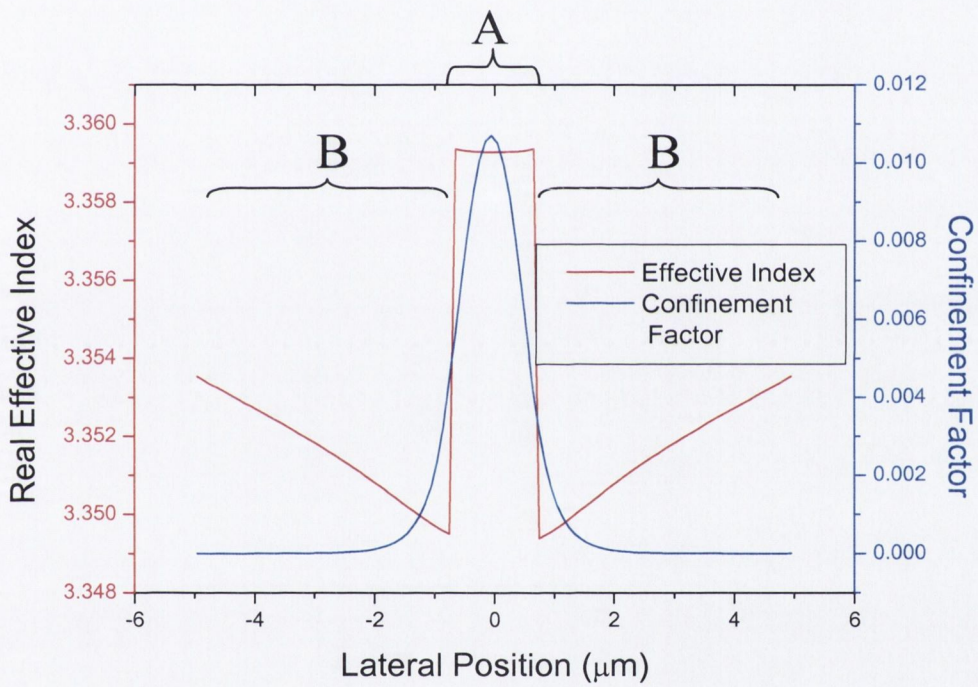


Figure 3-16 Effective index profile demonstrating strong index guiding in the lateral direction as seen from the concentration of the confinement factor to the region beneath the current stripe

Although there is a reduction in the effective index profile with carrier density the effective index step difference between the central stripe region and the computational boundary is approximately $6x10^{-3}$. This effective index step difference is achieved by varying the normal aluminium mole fraction in the blocking layer from Xb = 0.6 to Xb = 0.8, while the remaining parameters in table 3-1 are unchanged. This ensures that the majority of the optical field is concentrated within the central stripe region

with little overlap of the absorption regions under the blocking layers. As a result, no absorption is seen in the lateral modal gain profile. Figures 3-16 and 3-17 showing the spatial variation in confinement factor, real effective index and modal gain profile are all taken at a time of 1ns after turn on. They result from the solution of the coupled carrier density rate equations (3.30) and the photon number rate equation (3.31). The evolution of the power output from the front facet shows a decaying oscillation, termed relaxation oscillation. This is observed in non self-pulsating lasers after turn on or after direct current pulse modulation. After turn on the carrier density profile increases above its threshold value, once the modal gain overcomes the mirror and free carrier losses the photon number and output power increase sharply, this can be seen as the first and highest peak in figures 3-18 and 3-19 profile.

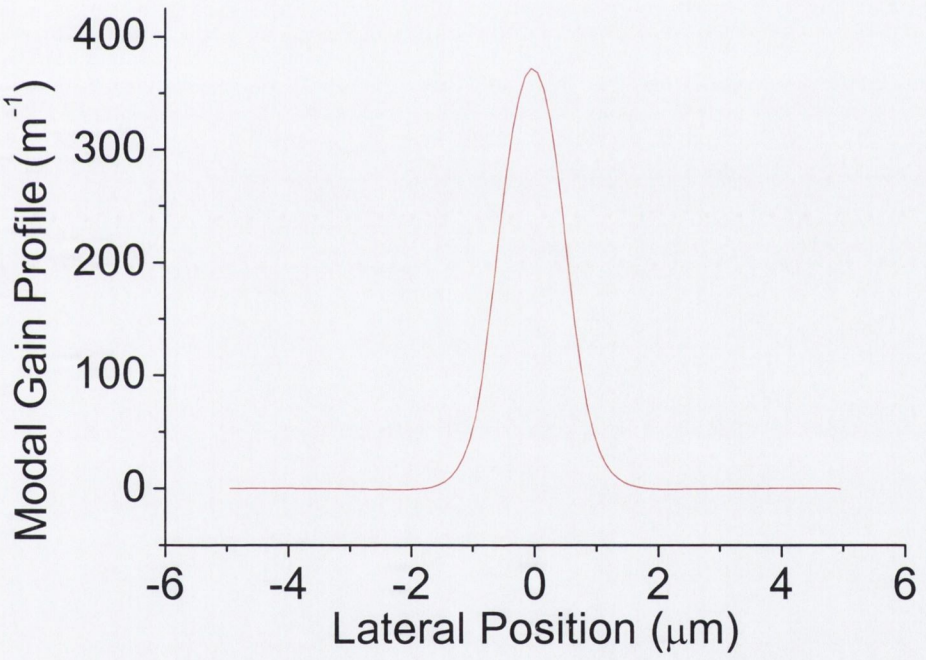


Figure 3-17 For the strongly guided lateral field the modal gain profile contains no absorption due to the confinement of the field to regions of gain only.

With this increase in photon number due to stimulated emission there is a subsequent decrease in the carrier density to the extent that the modal gain decreases below its threshold value until such time as the carrier density can build up again. This process is repeated but each successive cycle is diminished since there is no absorption in the lateral regions to provide positive feedback effect similar to Q-switching. As we will

now demonstrate the occurrence of absorption regions prevents this damping mechanism and contributes to pulsations that are self-sustaining.

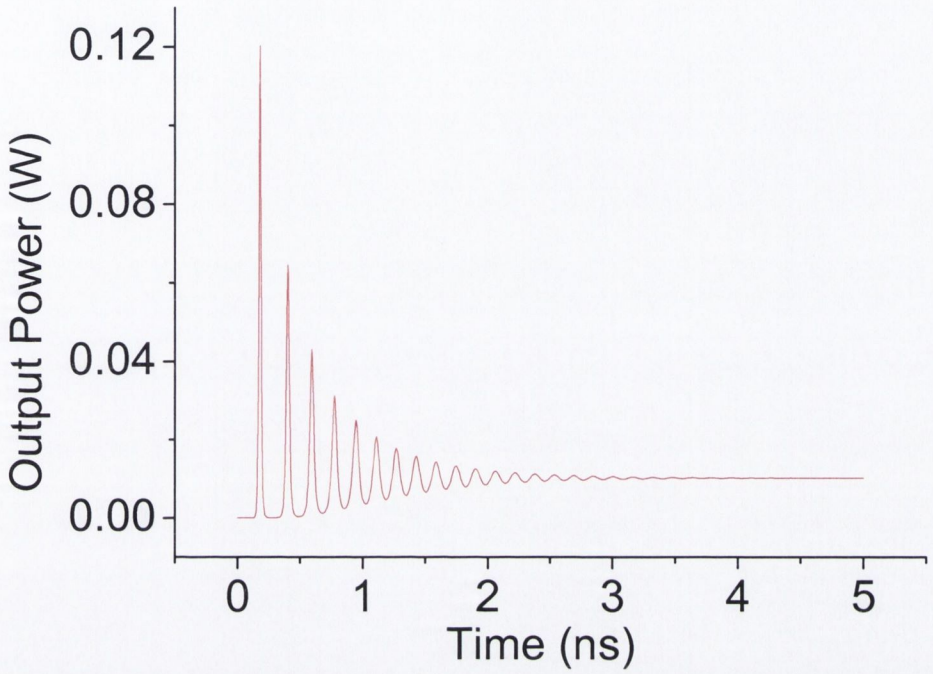


Figure 3-18 Relaxation oscillations in the output power from the front facet

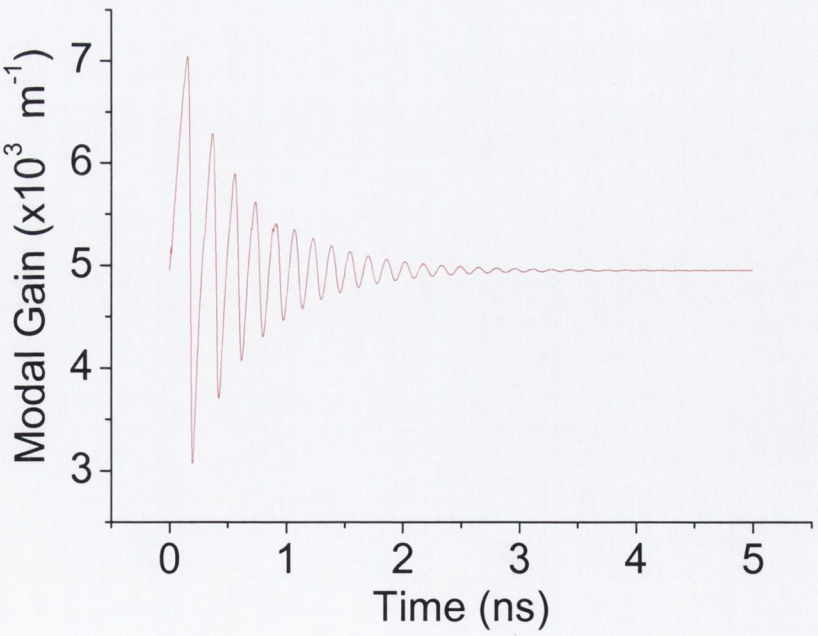


Figure 3-19 Relaxation oscillations in the modal gain profile

As the name suggests self-pulsation sustains the pulsed behaviour over time without the damping seen in the earlier case. Typically the pulsation frequency ranges between 800MHz and 5GHz depending on the normalised bias current.

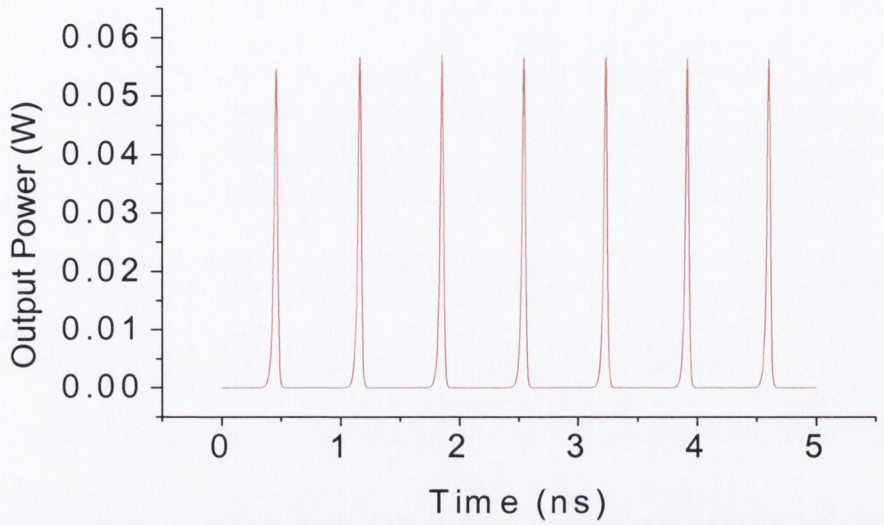


Figure 3-20 Self-sustained pulsation evolution of output power versus time. The self-pulsation frequency is 1.45GHz and bias current is 30mA, where the structure parameters are given in Tatable 3-1.

If we look at the carrier density evolution in the centremost section i.e. lying in the centre of the stripe region, we see that as the carrier density reaches its peak as

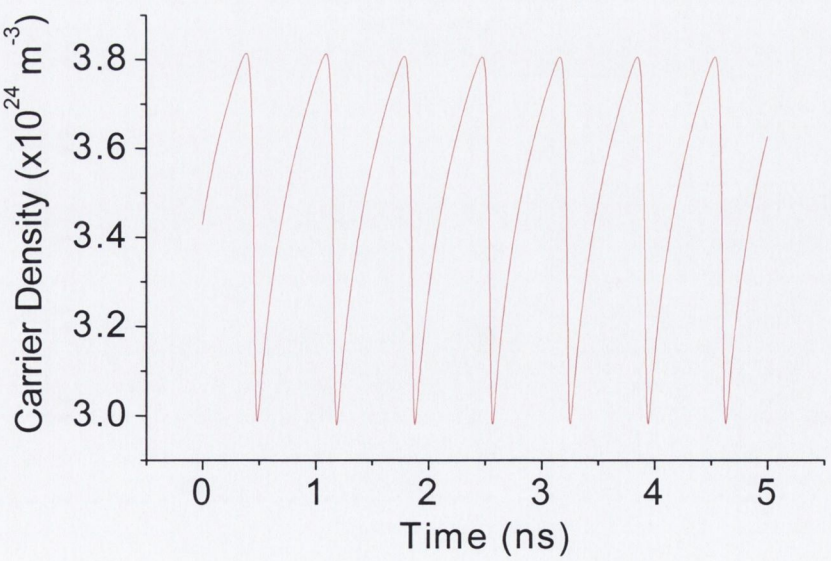


Figure 3-21 Carrier density variation within the centremost section of the active region

the pulse begins to form and as the output increases the carrier density reduces due to stimulated emission.

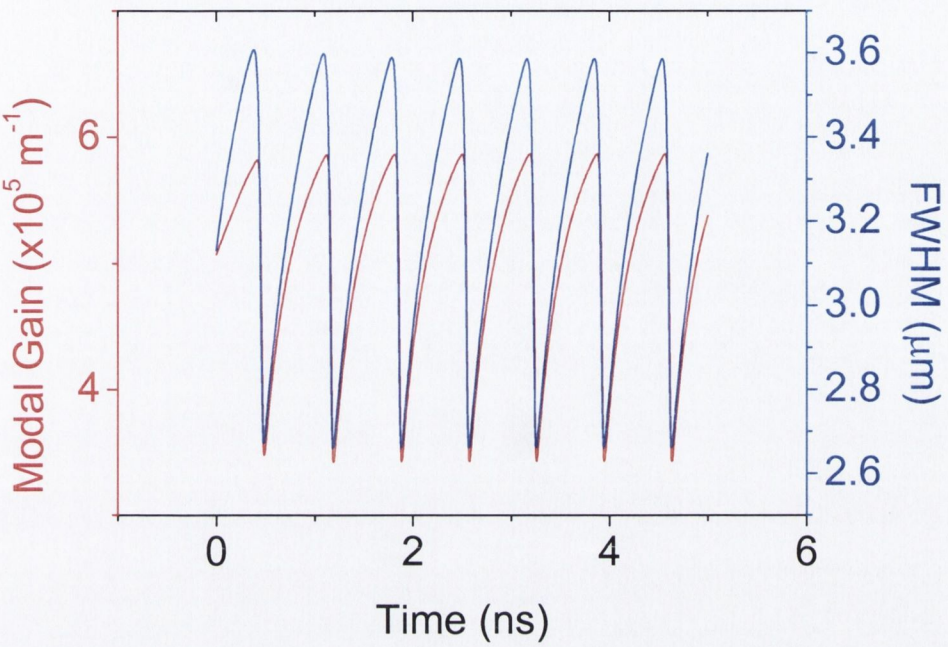


Figure 3-22 The full width half maximum of the lateral electric field is synchronised to the increase and decrease in the modal gain

An important feature of this type of self pulsation is that the increase in carrier density before a pulse is emitted reduces the effective index step in the lateral direction and as a result the full width half maximum (FWHM) of the lateral field increases mirroring the behaviour of the modal gain as seen in figure 3-22. With the resultant emission of the pulse and rapid decrease in the carrier density the effective index again increases in the central section resulting a focusing of the lateral field and a decrease in the FWHM. In order to gain further insight into the cause of the self-sustained modulation we concentrate on the spatial distribution of key parameters over the lifetime of a single pulse. Although the pulse itself occurs over of a time interval of the order of 100ps the build up of the modal gain profile is much slower and for this reason we have examined the pulse behaviour over 1ns from 0.5ns to 1.5ns as seen in figure 3-23.

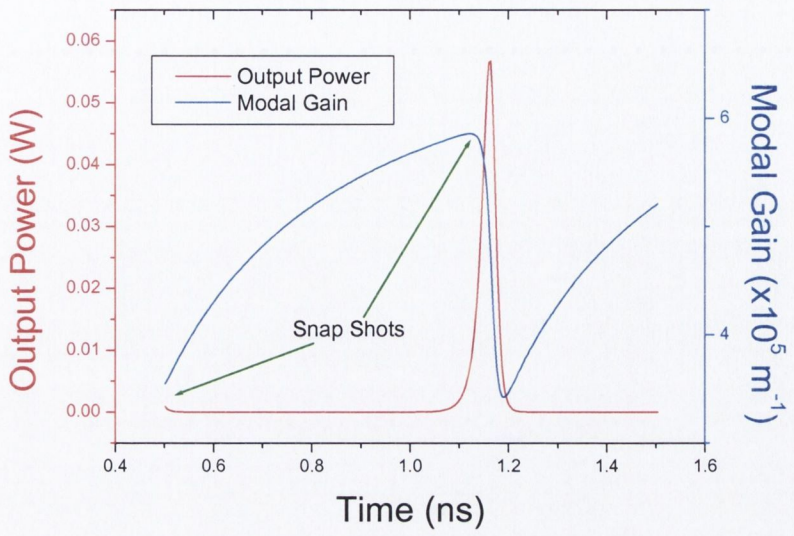


Figure 3-23 Build up in modal gain with the emission of a pulse over 1 ns time scale

We will take a closer look at the spatial profiles at the times corresponding to the minimum and maximum modal gain points as indicated in figure 3-23. We can see the carrier density profile is at a maximum in the region under the direct injection at 1.1ns just at the beginning of the pulse emission. The 0.5ns profile indicates that after pulse emission the carrier density is now depleted in the central region due to stimulated emission but that in the side regions it has increased and this can be explained due to the photo-generation of carriers in the absorber section. As the pulse is formed the optical field extends into the absorption regions, where photons are absorbed resulting in an increase in carrier density in these regions. This photo generated increase in the carrier density reduces the amount of absorption within these regions, the absorption therefore begins to saturate. This process is aided by the self-focussing of the optical field due to the increase in refractive index under the stripe as the carrier density is reduced due to stimulated emission.

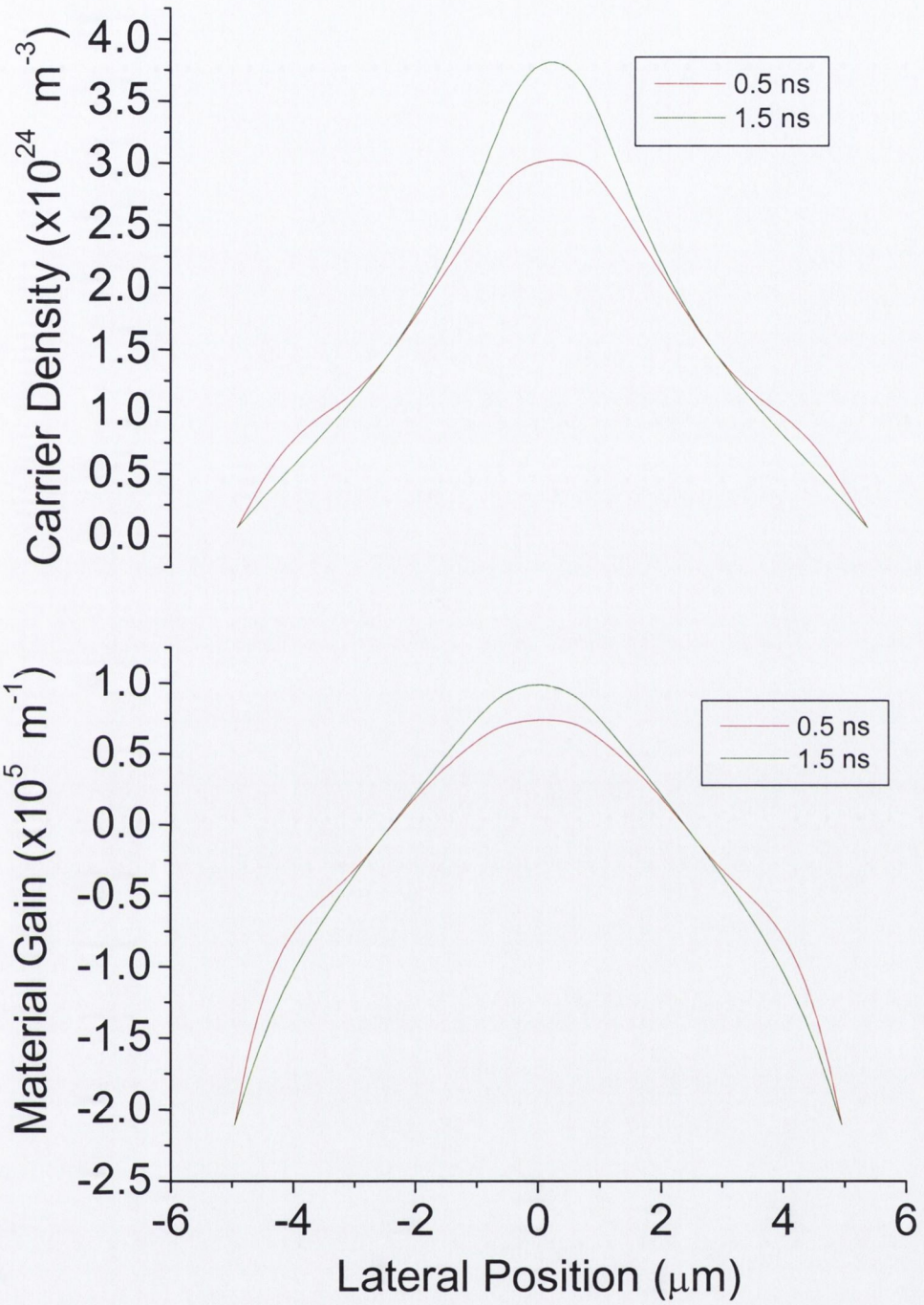


Figure 3-24 Lateral active layer carrier density and material gain variation at 0.5ns (modal gain minimum) and 1.5ns (modal gain maximum).

To demonstrate the importance of self-focusing and defocusing of the optical field the optical field was calculated once at threshold it then remained constant throughout the calculation. As can been seen in figure 3-25 this resulted in relaxation oscillations, thus demonstrating the importance of incorporating the carrier dependent optical field

and its contribution to the process of saturable absorption and enhancing self-pulsation.

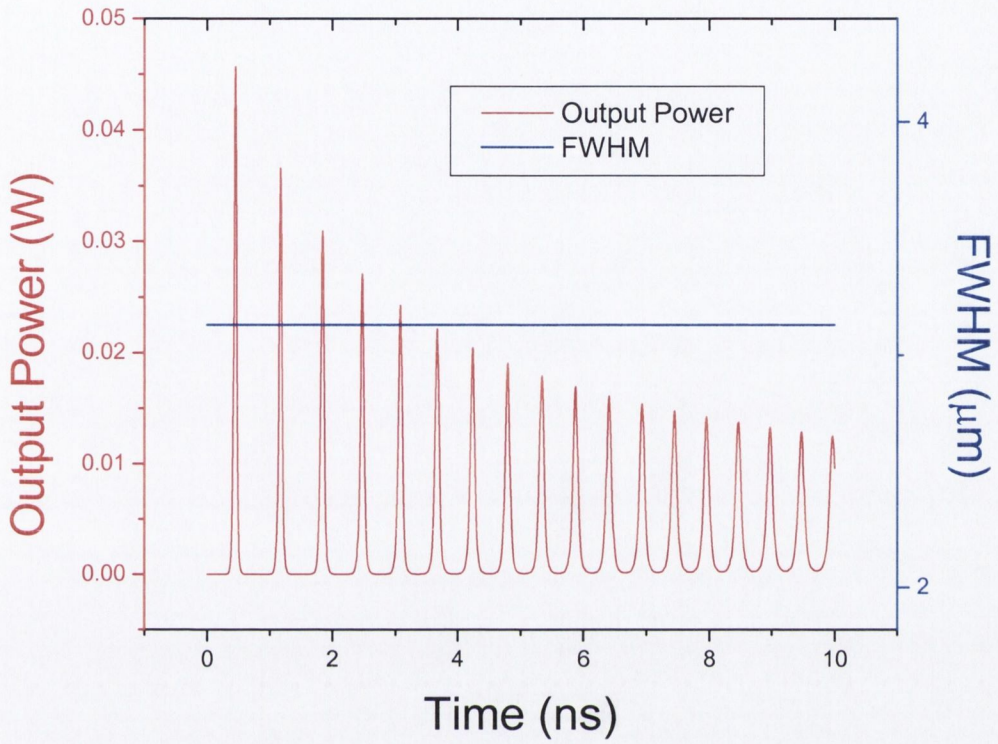


Figure 3-25 The FWHM of the optical field is constant throughout resulting in relaxation oscillations in the output power.

Up until this point we have not examined the confinement factor and in particular the amount overlapping of the absorption regions. As a result of the weak index guiding and negative differential index the effective index under the current stripe drops below the value at the computational boundary, this creates side lobes in the optical field profile as shown in figure 3-14. The corresponding modal gain profile shows a large region of optical absorption, without the appearance of the side lobes this modal absorption region would not be present.

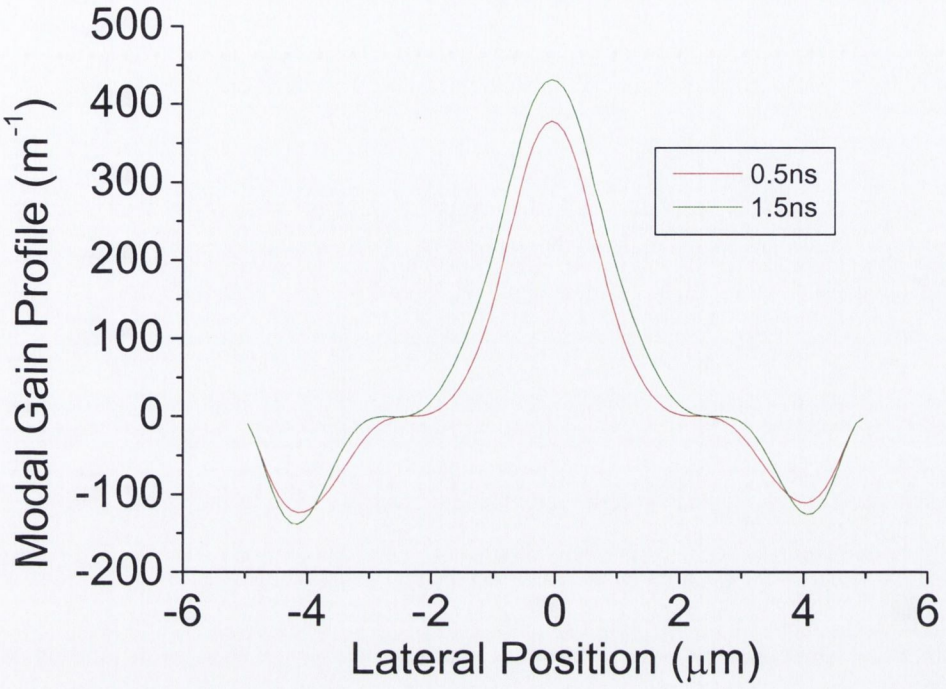


Figure 3-26 Modal gain profiles taken at the maximum and minimum modal gain value over one period. The effect of the lateral side lobes in the confinement factor is clearly evident

3.7 Conclusions

The work presented in this chapter has provided the justification for the calculation of the optical field throughout the simulation in order to account for the carrier density dependent variation of the optical field. The details of the rate equation model have been discussed, including the effects of current spreading, ambipolar diffusion and the threshold current determination. The fundamental limitations of the use of the effective index method for weakly guided waveguides were presented. Although the saturable absorption regions were created as a direct result of the failure of the effective index method, the mechanism of self-pulsation and its enhancement with the contribution of self focussing and defocusing is still valid. Therefore there is a need for a more rigorous treatment of the two-dimensional optical field and this is the subject of chapter 4.

References

1 "A Theoretical Analysis of Self-Sustained Pulsation Phenomena in Narrow-Stripe Semiconductor Lasers", M.Yamada, IEEE J. Quant. Electron. **29,** (5), 1993.

2 "A GaAs-$Al_xGa_{1-x}As$ Double Hetrostructure Planar Stripe Laser", H. Yonezu, I. Sakuma, K. Kobayashi, T. Kamejima, M. Ueno and Y. Nannichi, Jpn. J. Appl. Phys.**12,** (10), p 1585, 1973.

3 "An analytical solution of the lateral current spreading and diffusion problem in narrow oxide stripe (GaAl) As/GaAs DH lasers", G. Lengyel, P. Meissner, E. Patzak, and K.H. Zschauer, IEEE J.Quantum Electron. **18,** p 618, 1982.

4 "Steady-state junction-current distributions in thin resistive films on semiconductor junctions (solutions of $\nabla^2 v = \pm e^v$)", W.B.Joyce and S.H.Wemple, J. Appl. Phys. **41** p 3818 1970.

5 "Four Models of Lateral Current Spreading in Double-Hetrostrucutre Stripe-Geometry Lasers", R. Papannareddy, W. E. Ferguson, J K. Butler, IEEE J. Quant. Electron, **24,** (1), p 60, 1988.

6 "Electrical characterization of heterostructure laser" , W.B.Joyce, R.W.Dixon, J. Appl. Phys. **49,** p 3719, 1978.

7 "Derivative measurements of the current-voltage characteristics of double-heterostructure injection lasers", P. A. Barnes, T. L. Paoli, IEEE J. Quant. Electron, **12,** (10), p 633, 1976.

8 "A self-consistent static model of the double-heterostructure laser". DF.Wilt, A. Yariv, IEEE J. Quant. Electron, **17,** p 1941, 1981.

9 "Carrier Transport in double-heterostructure active layers", W.B.Joyce, J. Appl. Phys, **53,** (11) , p 7235, 1982.

10 "Handbook Series on Semiconductor Parameters, vol.2", M. Levinshtein, S. Rumyantsev and M. Shur, ed., World Scientific, London, p 3, 1999.

11 "Heterostructure Lasers", H. C. Casey, M. B. Panish, Academic Press, 1978.

12 "Low-Noise and High-Power GaAlAs Laser Diodes with a new Real Refractive Index Guided Structure", T. Takayama, O. Imafuji, H. Sugiura, M. Yuri, H. Naito, M. Kume and K. Itoh, Jpn. J . Appl. Phys, **34** (1) 1995.

13 "Two-Dimensional Analysis of Self-Sustained Pulsation for Narrow-Stripe AlGaAs Lasers", M. Yuri, J. S. Harris, T. Takayama, O. Imafuji, H Naito, M. Kume, K Itoh and T. Baba, IEEE Select.Topics.Quant.Electron **1** (2) 1995.

14 "Diode Lasers and Photonic Integrated Circuits", L. A. Coldren, S. W. Corzine, Wiley, New York, 1995.

15 "Numerical Recipes in C", W. H. Press, B. P. Flannery, S. A. Teukolsky, W. T. Vetterling, Cambridge University Press, 1988.

16 "A two-dimensional device simulator of semiconductor lasers", T. Ohtoshi, K. Yamaguchi, C. Nagaoka, T. Uda, Y Murayama, and N. Chinone, Solid-State Electron, **30,** (6), p 627, 1987.

17 "Low-noise and high-power real refractive index guided laser array", T. Takayama, O. Imafuji, M. Yuri, H. Naito, M. Kume, A. Yoshikawa and K.Itoh, Electron Letters **30**, (16), p 1307, 1994.

18 "Carrier-Induced Index Change in AlGaAs and 1.3μm InGaAsP Diode Lasers", J. Manning, R Olshansky and C Bing Su, IEEE J. Quant. Electron. **19,** (10), 1983.

19 "Optical waveguide theory", A. Snyder, J Love,Chapman and Hall, 1983.

Chapter 4 Two-dimensional Self-Pulsation

4.1 Introduction

This chapter aims to demonstrate the importance of a fully two-dimensional calculation of the optical field within the waveguide. We demonstrate the weaknesses of the effective index method for structures incorporating weak lateral guiding. It is shown that in order to achieve the solution of the two-dimensional system; the numerical solution of the non-hermitian eigenvalue problem is necessary. Based on the use of the implicitly restarted Arnoldi method and taking advantage of the inherent symmetry within the device, the two dimensional field profiles are calculated in a computationally efficient manner. This allows one to understand the mechanism of self-pulsation based on the spatial and temporal results of the model. The possibility to perform simulations far in excess of the threshold current is made possible. Some conclusions are drawn as to the possible factors that lead to the termination of the self-pulsation process at high currents.

4.2 The Advantages of Two-Dimensional Waveguiding

The need for a full two-dimensional solution of the wave equation was outlined in chapter 3 in particular the section relating to waveguide analysis. Figure 4-1 (shown again for clarity) demonstrates the clear advantage in solving the two-dimensional scalar wave equation for the weakly complex guided regime where the effective index approximation is no longer valid. As has been shown in chapter 2 the side lobes that appear close to anti-guiding within the effective index approximation result in an overestimate of the modal absorption within the regions of the active layer laying beneath the current stripe. It was therefore necessary to develop a simulator based on the two-dimensional finite difference method.

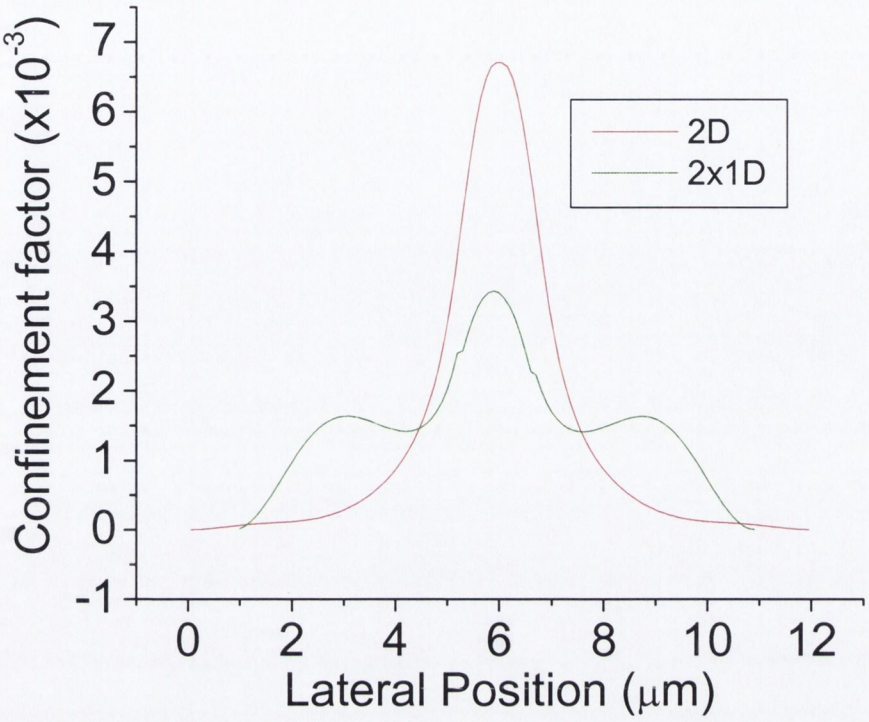


Figure 4-1 Comparing the confinement factors for the effective index method (2x1D) and the (2D) finite difference method for the carrier density profile shown in figure 2-22.

4.2.1 Use of the Inherent Symmetry of the Structure

The drawback of this more rigorous approach is that the computational effort scales approximately with the cube of the order of the matrix for standard QR based algorithms in which all eigenvalues and eigenvectors are determined [1]. The QR method is considered one of the most stable methods of solution, and it is based on Schur factorisation, that is for each matrix A, there exists an orthogonal matrix Q, so that

$$Q^* A Q = R \tag{4.1}$$

in which R is upper triangular and Q^* represents the inverse of Q. In the standard nomenclature, R stands for the fact that the right of the matrix is nonzero. The Schur factorisation reveals much of the eigenstructure of A: its diagonal elements are the eigenvalues of A and the off-diagonal elements of R indicate how small the angles

between the eigenvectors may be [2]. It is not an efficient method for large sparse matrices where only a small number of eigenvalues are required. This means that a simulation in which the field is calculated after each update of the carrier density and photon number would not be achievable on even the highest specification personal computer. A new numerical approach needed to be found that would allow the solution of the problem on a more reasonable time scale. The most obvious method in reducing the computational time was to take advantage of the inherent symmetry along the lateral dimension of the device.

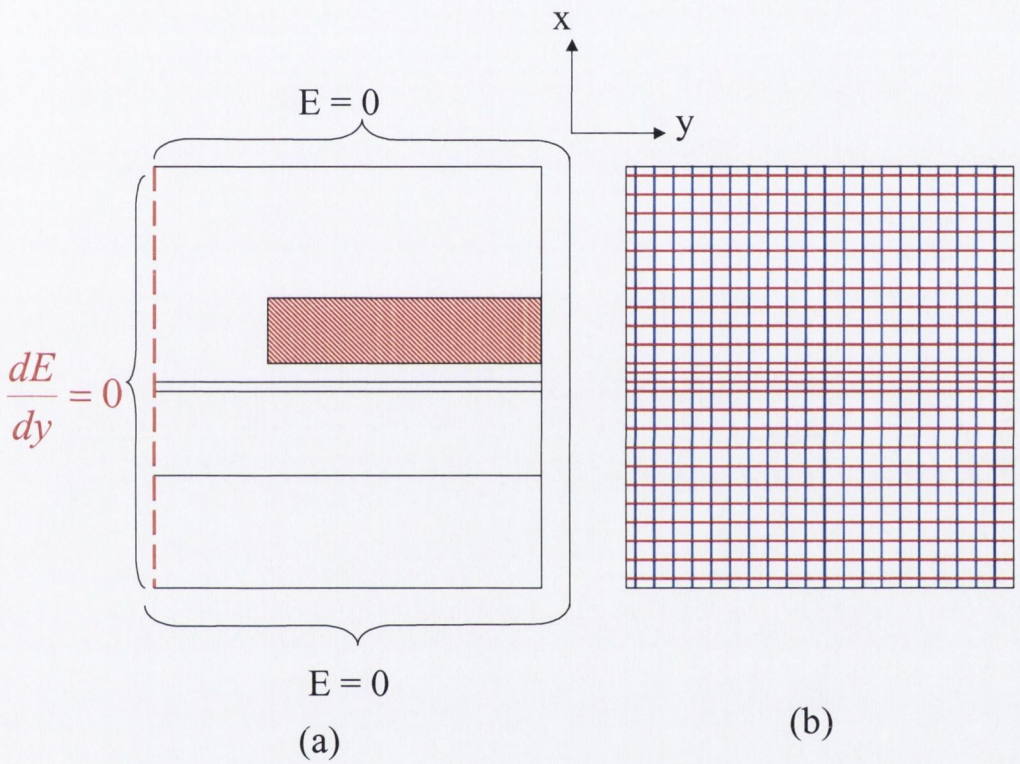


Figure 4-2 (a) Schematic of the device structure for the numerical calculation, in which half the lateral waveguide is used. (b) Schematic showing and equal mesh in the lateral (y) and unequal mesh in the transverse (x) direction.

Since there is no difference between the geometric or material properties of the device, a line joining the middle of the current stripe and the bottom substrate the device could cut the computational workspace in half. Since we are only interested in the fundamental mode the electric field of interest will be even (symmetric about the y axis).

By applying the von Neumann boundary condition $\frac{dE}{dy} = 0$ along the $(x,0)$ boundary we can ensure that only half the waveguide space is required to solve for the two-dimensional mode of interest. The benefits of this approach can be seen from the reduction in the number of lateral grid points by half (typically from $N_y = 120$ to $N_y = 60$ points). By dividing the computational space in half the order of the matrix equal to N, where $N = N_x \times N_y$, is reduced by half. This results in reduction in the computational time by a factor of 8 due to the cubic dependence of the matrix order. With the standard discretisation approach, the grid spacing in the transverse and lateral directions are kept constant in each dimension. By applying an unequal grid spacing within the transverse direction, as shown in the schematic in figure 4-2(b), allows one to place grid points within the thin active region while choosing a wider grid spacing for the outer cladding and substrate layers. The precision of the electric field profile could still be maintained, while reducing the required number of transverse grid points.

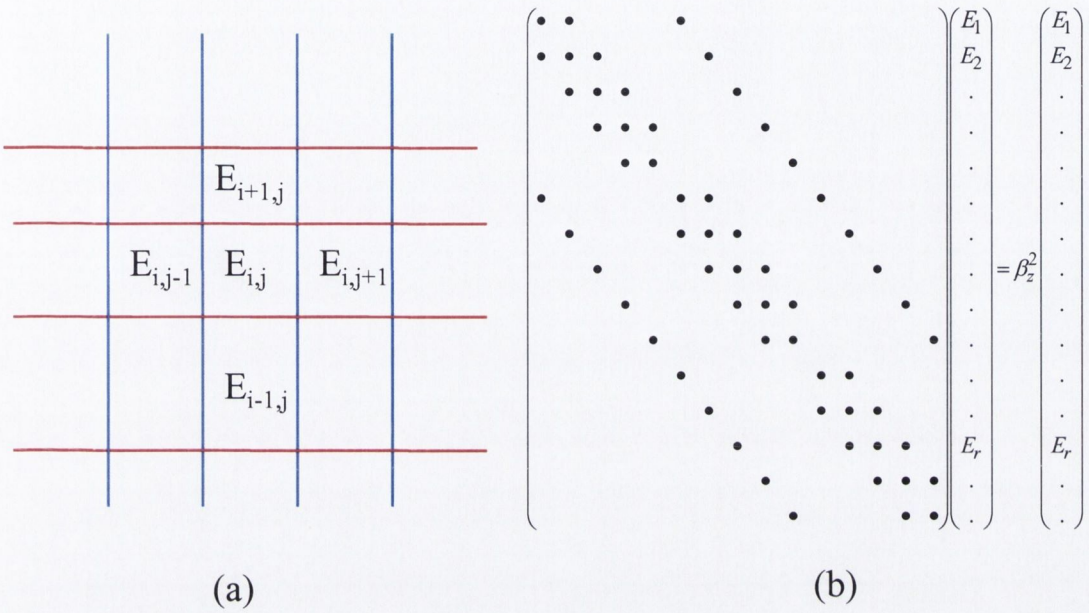
4.3 Numerical Solution of the Non-Hermitian Eigenvalue Problem

The non-uniform finite difference method is based on a five point discretisation scheme. Each grid point yields a five point linear equation in terms of $E_{i+1,j}$, $E_{i-1,j}$, $E_{i,j+1}$,$E_{i,j-1}$ (see figure 4-3(a)). A set of linear equations for all the grid points (i = 1, ...N_y and j = 1,....N_x) may now be rewritten in the following eigensystem.

$$AE = \beta_z^2 E \tag{4.2}$$

Here β_z represents the longitudinal propagation constant, the square of which represents the eigenvalue of equation (4.2). The matrix A as seen from the illustration in figure 4-3(b) for the simple Nx = 5, Ny = 3 case is sparse, containing just five non-zero diagonals as a result of the contribution from each of the five points in the discretisation. For the typical case the order of the matrix (N), is 3060. The number of non-zero elements (15078) represents 0.16% of the total number of elements in the matrix. Considering the size and sparsity of the matrix, a compressed row storage (CRS) scheme is employed. This scheme puts the subsequent nonzero elements of the

matrix in contiguous memory locations. Without this scheme it would be impractical to compute the eigenvalues due to the extensive memory required to store all the matrix elements. Without using the CRS format the matrix vector product is proportional to N^2 operations, whereas with the CRS scheme that number is reduced to 5N.



(a) (b)

Figure 4-3 (a) Illustration of the grid points that contribute to the five point discretisation for grid element (i,j). (b) Illustration of the sparse banded five diagonal matrix A, where each • point is non-zero. Taken for the simple case of $N_x = 5$, and $N_y = 3$.

4.4 Eigenvalue and Eigenvector Computation

The eigenvalue problem for square matrices A, that is, the determination of nontrivial solutions of equation (4.2), is a central topic in numerical linear algebra. Our approach takes full advantage of the sparsity of the matrix and circumvents the large memory requirements associated with dense methods. For realistic grids, the use of standard dense matrix eigenvlaue solvers, leads to unmanageable cpu time and memory requirements, since the solution for all eigenvalues and eigenvectors is attempted. The prime example of this is the LAPACK routine zgeev, which computes all eigenvalues and eigenvectors for a non-hermitian matrix [1]. Only a small fraction of these eigenvalues correspond to bound modes. Because we wish to select these modes, we impose the condition

$$\mathrm{Re}(n_{Clad}) \leq \mathrm{Re}(\beta_z) \leq \mathrm{Re}(n_{Well}) \tag{4.3}$$

And since we are only interested in the lasing mode, we only consider the mode with the largest modal gain. The second condition that is imposed after equation (4.3) is satisfied is that

$$Max \quad \mathrm{Im}(B_z) > 0 \tag{4.4}$$

The saving in computational effort by choosing an algorithm, which computes this very limited subset of eigenpairs, cannot be overstated. A longstanding method that is of great significance and serves as the basis for many algorithms is the Power iteration. The method is based on the idea that if a given vector is repeatedly applied to a matrix, and is properly normalised, then, ultimately it will lie in the direction of the eigenvector associated with the eigenvalues, which are largest in absolute value. The rate of convergence of the Power iteration depends on the ratio of the second largest eigenvalue (in absolute value) to the largest eigenvalue (in absolute value) and for many applications this leads to unacceptably slow convergence. The Power Method and the Inverse Power Method, in their pure form are no longer competitive methods even for the computation of a few eigenpairs, but they form either explicitly or implicitly, part of the most modern methods such as the QR method and the methods of Lanczos and Arnoldi [2]. Appropriate algorithms for determining a subset of eigenvalues/eigenvectors of large, sparse, nonsymmetric matrices include simultaneous iteration [3], nonsymmetric Lanczos algorithm [4], and variations on the method of Arnoldi [5].

4.5 The Arnoldi Method

Through correspondence with Professor Sorensen of Rice University, Austin, Texas and collaboration with a researcher, Heidi Thornquist, now of Sandia National Laboratories Albaquerque, it was possible to apply the Implicitly Restarted Arnoldi Method (IRAM) pioneered by Sorensen [6] to solve the eigensystem resulting from the discretisation of the two-dimensional scalar wave equation. The single-vector iteration like the power method does not take advantage of the information provided by the successive vectors in the sequence

$$v, Av, A^2v, A^3v, ...$$

This sequence may be rich with information along eigenvector directions that correspond to the dominant eigenvalues of A. By considering the k-dimensional Krylov subspace

$$\mathrm{K}_k(A,v) = span\left\{v, Av, A^2v, ...A^{k-1}v\right\} \tag{4.5}$$

The Arnoldi method [7], is used to construct an orthonormal basis of $\mathrm{K}_k(A,v)$. The result is the k-step Arnoldi factorisation of A

$$AV_k = V_k H_k + fe_k^T \tag{4.6}$$

where $V_k \in \mathbb{C}^{n\times k}$ has orthonormal columns and $V_k^H f = 0$. $\mathbb{C}$ denotes complex numbers and the conjugate transpose of V is denoted by V^H. The jth canonical basis vector is denoted by ej. Since A is non-hermitian, then $H_k = V_k^H AV_k$ is a $k \times k$ upper Hessenberg matrix. This factorisation can be used to obtain the approximate eigenvalues and eigenvectors for A. Incorporating an accelerating scheme with the Arnoldi method helps keep the dimension of the krylov subspace small. The two techniques essential for practical implementation of the IRAM are Restarting and Spectral transformations. Restarting the Arnoldi method accelerates convergence by modifying the starting vector v using eigenvector information obtained in the previous Krylov subspace. Spectral transformations improve the convergence of the Arnoldi method through the substitution of A with $\varphi(A)$, where $\varphi(\lambda)$ is some simple function [8]. This transformation serves to map interior or clustered eigenvalues of A to dominant, well separated eigenvalues of $\varphi(A)$. The method used here is the shift-invert spectral transformation

$$\varphi_{SI}(\lambda) = \frac{1}{\lambda - \sigma} \tag{4.7}$$

which emphasises the eigenvalues around the shift σ. The IRAM provides a numerically stable way to extract the desired eigenvalues and eigenvectors form a high-dimensional krylov subspace. Further information on this method can be found in [6].

Since one of the most crucial points concerning the self-pulsation simulation is that the electric field needs to be updated 5000 times over a 5ns simulation, an LU factorisation of the first matrix in the sequence is used to compute the eigenvalues and eigenvectors of the banded matrix. This is then employed as a preconditioner for all of the subsequent matrices in the sequence. Using shift-invert with ARPACK (the public domain software based on the IRAM), the LU factorisation is used to apply the inverse of the banded matrix. This is an exact shift-invert strategy. A fixed polynomial operator was used to approximate the spectral transformation but this was later discarded since there was no resulting increase in efficiency in this particular case. A more thorough explanation of this method can be found in [9].

The time taken for a standard simulation running on a pentium IV, 2.2GHz, 256MB RAM computer is 21 hours and 12 minutes. The shortest time for which the optical field is updated is 1ps and the simulation calculates the first 5ns of the laser diode emission. It is not possible to make a comparison of the considerable improvement in the use of the implicitly restarted Arnoldi method over the standard QR based algorithm since for matrices of the size 3060x3060, the standard method requires vast amounts of memory to store the whole matrix and this is not possible on a personal computer. This emphasises the advantage of the method employed in it's execution on a personal computer resulting in simulations extending for a reasonable time period.

4.6 A Two-Dimensional Perspective

Apart from the inaccuracies of the effective index method in regard to its representation of the two-dimensional field for weakly guided structures, there are other weaknesses in this type of approach. By separating the device into two main regions; region A under the current stripe and region B under the blocking layers, has often resulted in discontinuities in the confinement factor at the boundary between these regions. This comes about as a result of not treating the waveguide as a whole. The databases that are used within the effective index method are comprised of the real and imaginary effective index as well as the transverse confinement factors variation with carrier density. The wavelength variation due to the shift in peak gain with carrier densities is neglected since the difference between its inclusion or omission is negligible. The full two-dimensional treatment on the other hand has one

waveguide and one wavelength for the whole structure offering a clearer picture of the important parameters.

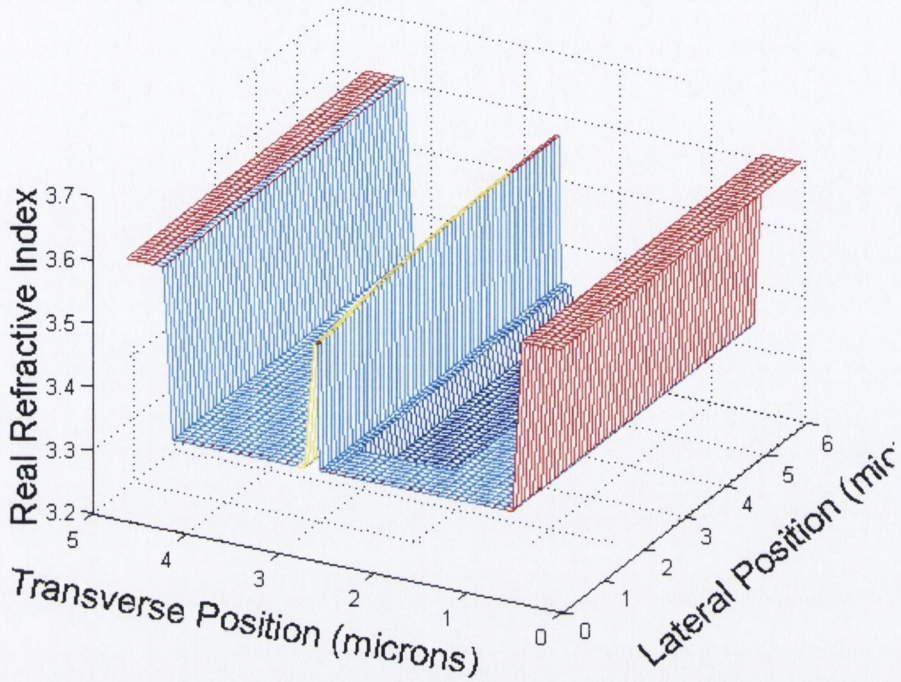


Figure 4-4 A two-dimensional perspective of the real refractive index within the waveguide including the effect of carrier density within the active region. The parameters of which are defined in table 3-1.

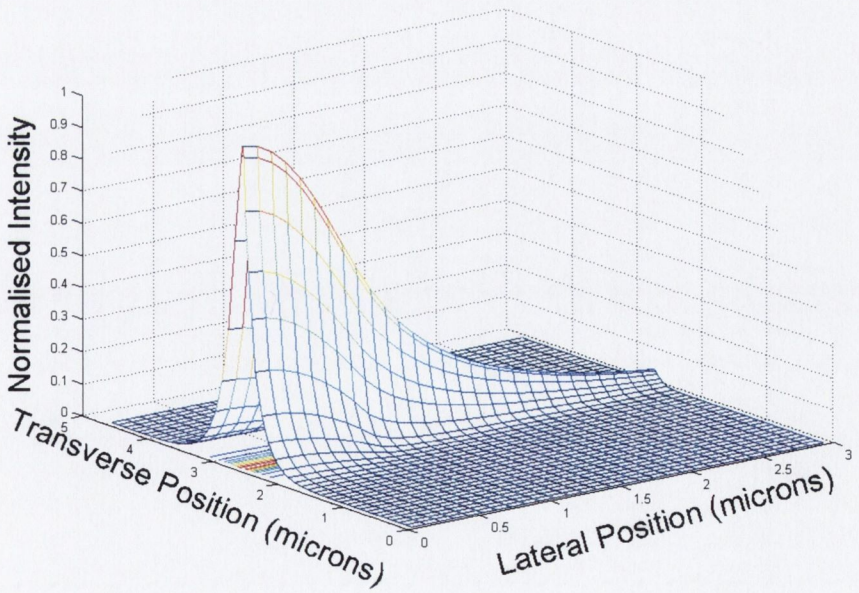


Figure 4-5 Normalised intensity distribution for the waveguide shown in figure 4. The lateral position has been curtailed to 3μm to give a better perspective of the profile.

If we start by considering the two-dimensional waveguide as shown in figure 4-4 we can see the high refractive GaAs substrate and top contact regions in brown. The cladding region is shown in light blue and the asymmetry in the waveguide brought about by the low index $Al_{xb}Ga_{1-xb}As$ blocking layer regions are shown in dark blue. The line for which the transverse position is zero corresponds to the top contact, and the line for which the lateral position is zero represents the line of symmetry through the device and also the centre of the current stripe.

Due to the presence of the current stripe at the axis of symmetry boundary, the active layer refractive index is lower and increases as one moves away from the current stripe along the lateral direction. The normalised intensity profile for this waveguide at the peak modal gain point is shown in figure 4-5. The peak of the intensity profile coincides with the position of the active layer as shown in figure 4-4. It is clear from this profile that through the correct application of the symmetry line boundary conditions, the field profile behaves as though the whole waveguide were present.

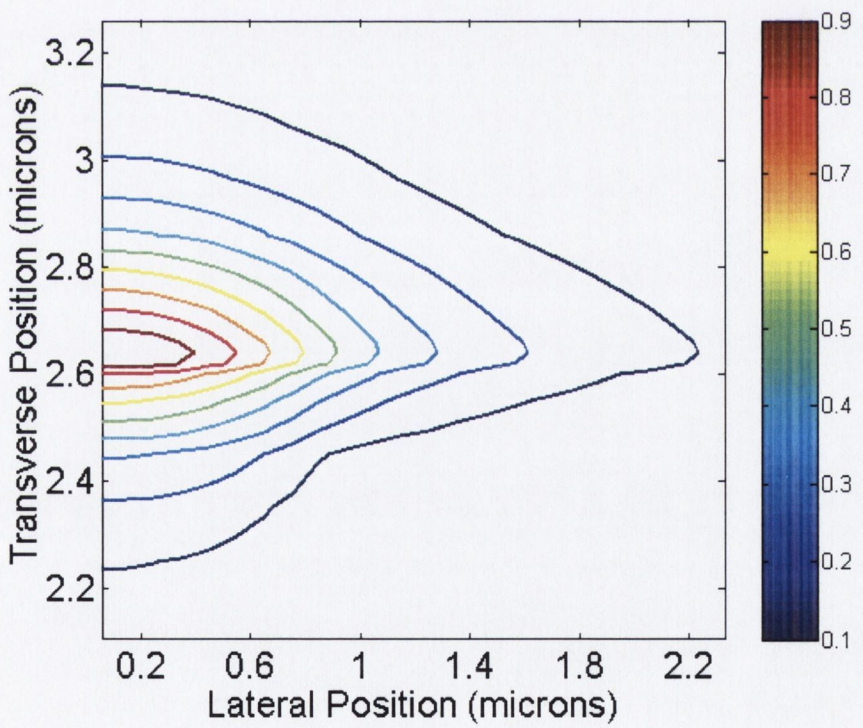


Figure 4-6 Contour plot of the normalised intensity profile, reflecting the asymmetry of the waveguide

A contour plot of the field profile is required in order to obtain a perspective as to how the lower refractive index asymmetry due to the blocking layer affects the mode profile. In figure 4-6, we can see that the light is confined strongest in the high refractive index cladding regions in comparison with the lower refractive index cladding layers.

4.7 Temporal Dynamics

The two-dimensional field calculation is incorporated into the carrier density and photon rate equations through the confinement factor as has been described in equation (1.28) and (1.30). For a device of length 250μm and 1.2μm stripe width, self-pulsation has been achieved as seen from the front facet output energy shown in figure 4-7. The spreading of the field profile into the absorption sections is predominantly dependent on the carrier density in the active regions under the stripe. Figure 4-8 illustrates that as the carrier density increases so to does the FWHM of the field within the active region. This occurs as a result of a reduction in the active later refractive index with increasing carrier density.

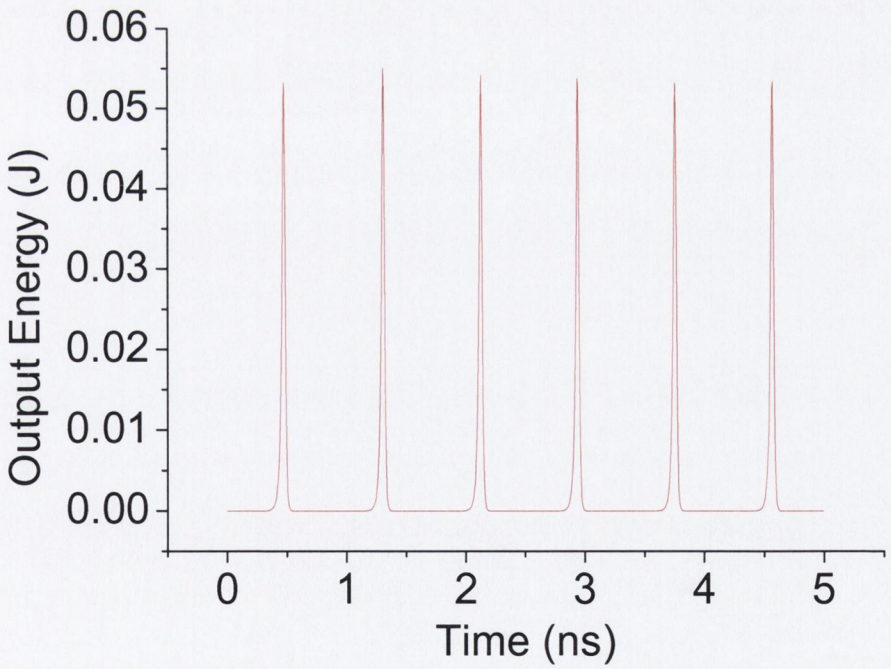


Figure 4-7 Temporal evolution of the output energy emitted from the front facet. The threshold current is 25.6mA. The bias current was set to 30mA giving a self-pulsation frequency is 2.23GHz

As the pulse is emitted, the loss of carriers due to stimulated emission results in a contraction of the FWHM, a term known as self-focusing. This focusing and defocusing of the electric field enhances the self-pulsating mechanism.

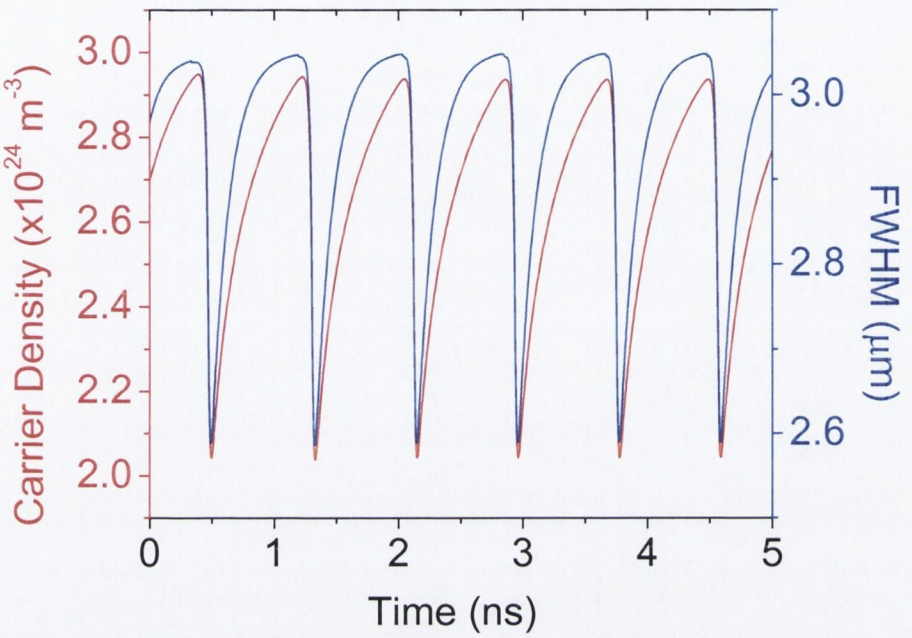


Figure 4-8 The direct relationship between the carrier density of the centremost section and the FWHM can be seen. The maximum variation is 0.45μm

Both the peak operating carrier density as well as the FWHM values were larger in the case of the effective index methods in figure 3-21 and 3-22 respectively. This is a result of the artificially large optical confinement under the blocking layers in the effective index method resulting in a larger amount of modal loss in these regions (figure 3-26) accounting for the higher carrier density and FWHM value seen there. Another key parameter that is correlated to the peak carrier density is the lasing wavelength. Apart from the case of spatial hole burning in which there is a depletion in the carrier density profile directly under the stripe due to the increased stimulated emission in this region, the central peak carrier density can normally be represented by the carrier density in the centremost section. As has been described within the theory section, the calculated wavelength is determined from the energy at which the gain profile is a maximum. The absorption values for carrier densities below transparency are determined for this energy also. Since the wavelength shift between the maximum and minimum carrier density value is just 0.55nm, the effect that this

has on the optical field profile is quite small. We can see that the wavelength decreases with higher carrier density due to the shift in the gain peak to higher energies.

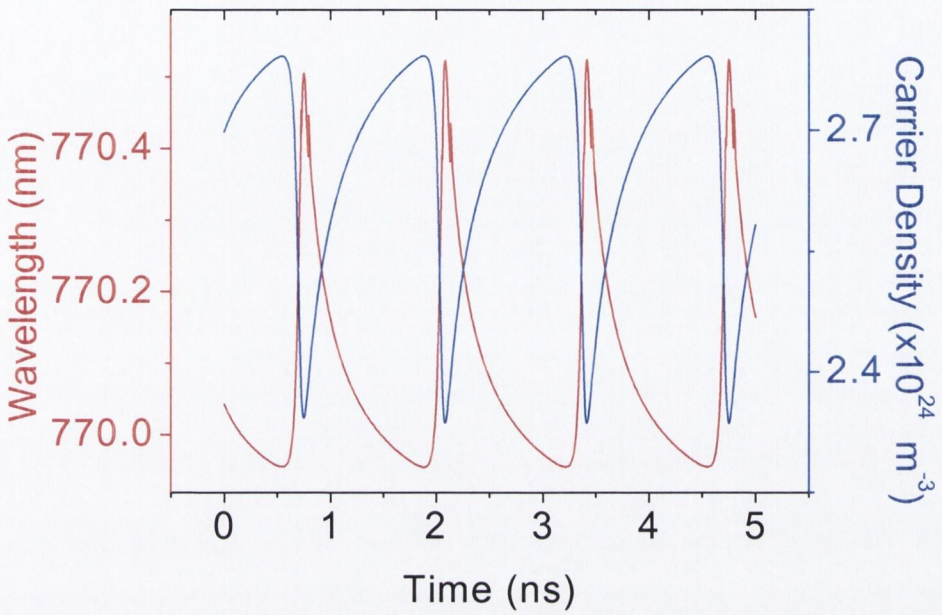


Figure 4-9 Variation in wavelength with and peak (centre most section) carrier density over time. The bias current was set at 27mA.

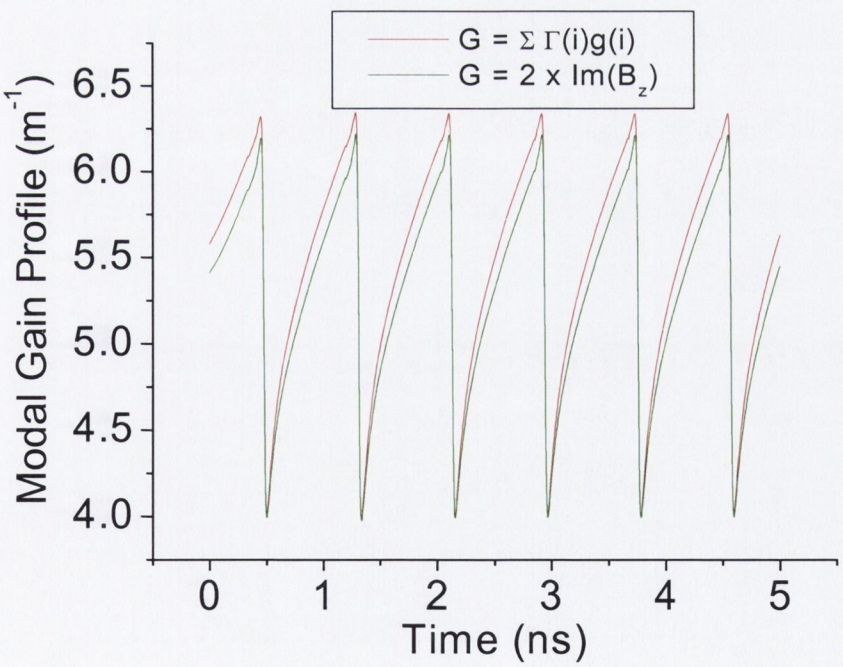


Figure 4-1 Comparison of the modal gain calculated from the imaginary component of the propagation constant and the sum of the material gain and confinement factor in each section.

Previously, it was not possible to make an accurate comparison between the modal gain as calculated from the imaginary component of the longitudinal propagation constant $\mathrm{Im}(B_z)$, with the sum of the product of the material gain and the confinement factor in each section, see equation (4.9). The calculation of the two dimensional field allows this comparison to be made and it also serves as a means of testing the validity of the eigenvalues calculated from the IRAM.

$$G = 2 \times \mathrm{Im}(B_z) \tag{4.8}$$

$$G = \sum_{i=1}^{N_y} \Gamma(i) g(i) \tag{4.9}$$

Figure 4-10 shows that there is a close agreement between the modal gain calculated from the imaginary component of the longitudinal propagation constant, equation (4.8), depicted here in green, and the modal gain calculated from the sum of the products of the material gain and confinement factor in each section, equation (4.9), shown here in red.

4.8 Spatial Dynamics

By combining the temporal and spatial information we can examine the behaviour of the laser at the maximum and minimum modal gain. These points are chosen since they give the largest contrast in parameters and occur just before and after the output of a pulse.

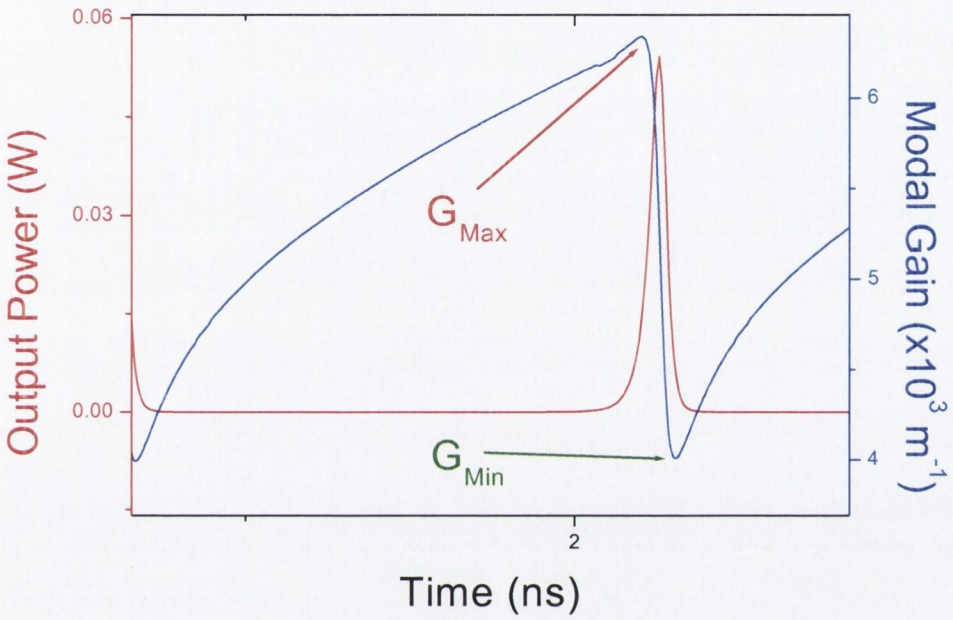


Figure 4-11 Output energy and modal gain profiles over the emission of a pulse, showing the maximum and minimum modal gain points.

As can be clearly seen in figure 4-11, before the emission of the laser pulse G_{Max}, the carrier density is at its maximum value and there is modal absorption within the side regions, brought about by the material absorption and enhanced by the defocusing of the optical field as seen by the increase in the confinement factor within these regions. As the pulse begins to be emitted, this absorber region saturates due to the creation of the photo-generated carrier and there is a rapid increase in the photon number due to the increased modal gain. Once the pulse is emitted, G_{Min} the carrier density level has been depleted due to the stimulated emission and the self-focusing of the light can be seen from the confinement factor. This process is repeated giving the self-sustained pulsation. This process could not be sustained without the use of the saturable absorber since its presence requires the modal gain to reach a higher threshold value than would be the case without it.

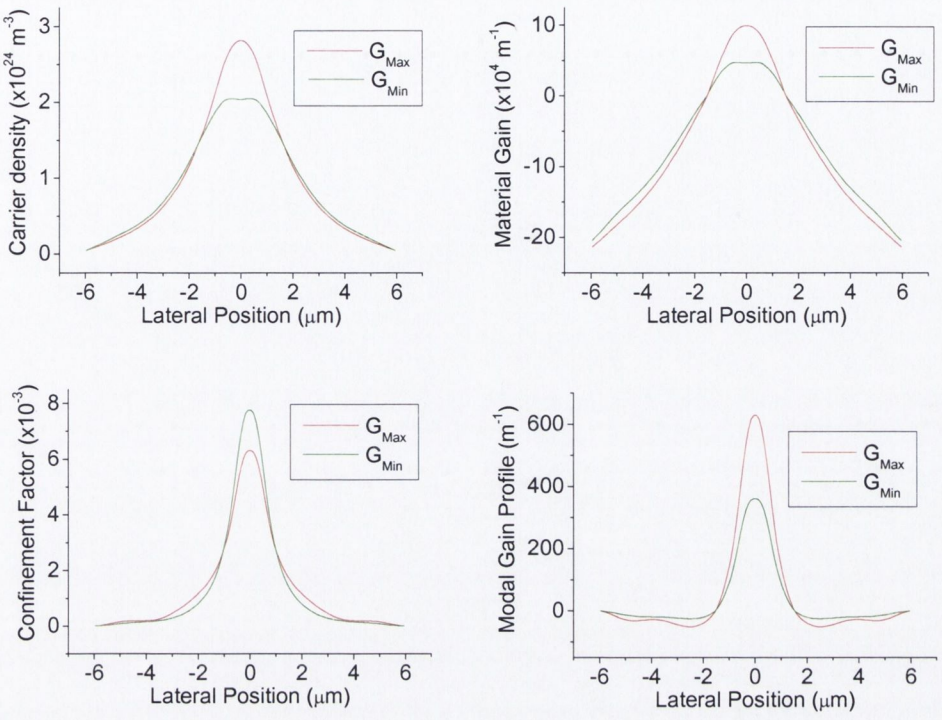


Figure 4-12 The lateral profiles of clockwise carrier density, material gain, confinement factor and modal gain profile taken for the maximum and minimum modal gain.

Then as it suddenly saturates with the beginning of the emission the photon number increase rapidly giving the pulse. Without the enhancement that is provided in this process by the self-focussing and defocusing, this process would not be possible. The true behaviour of the optical field can only be observed within the framework of a fully two-dimensional calculation.

Direct experimental evidence of the self-focusing effect during the emission of a pulse was shown in [10]. The normalised intensity profile along the plane of the active region was recorded using a ccd camera. From these results the ordinary definition of the FWHM was not applicable due to the asymmetric intensity profile distributions. A quantity $\bar{x}$ was defined as weighted central position, weighted by the intensity distribution as

$$\bar{x} = \frac{\int xI(x)\,dx}{\int I(x)\,dx} \tag{4.10}$$

The standard deviation of x from this weighted central position was defined by the quantity σ where,

$$\sigma = 2\sqrt{\frac{\int (x-\bar{x})^2 I(x)\,dx}{\int I(x)\,dx}} \tag{4.11}$$

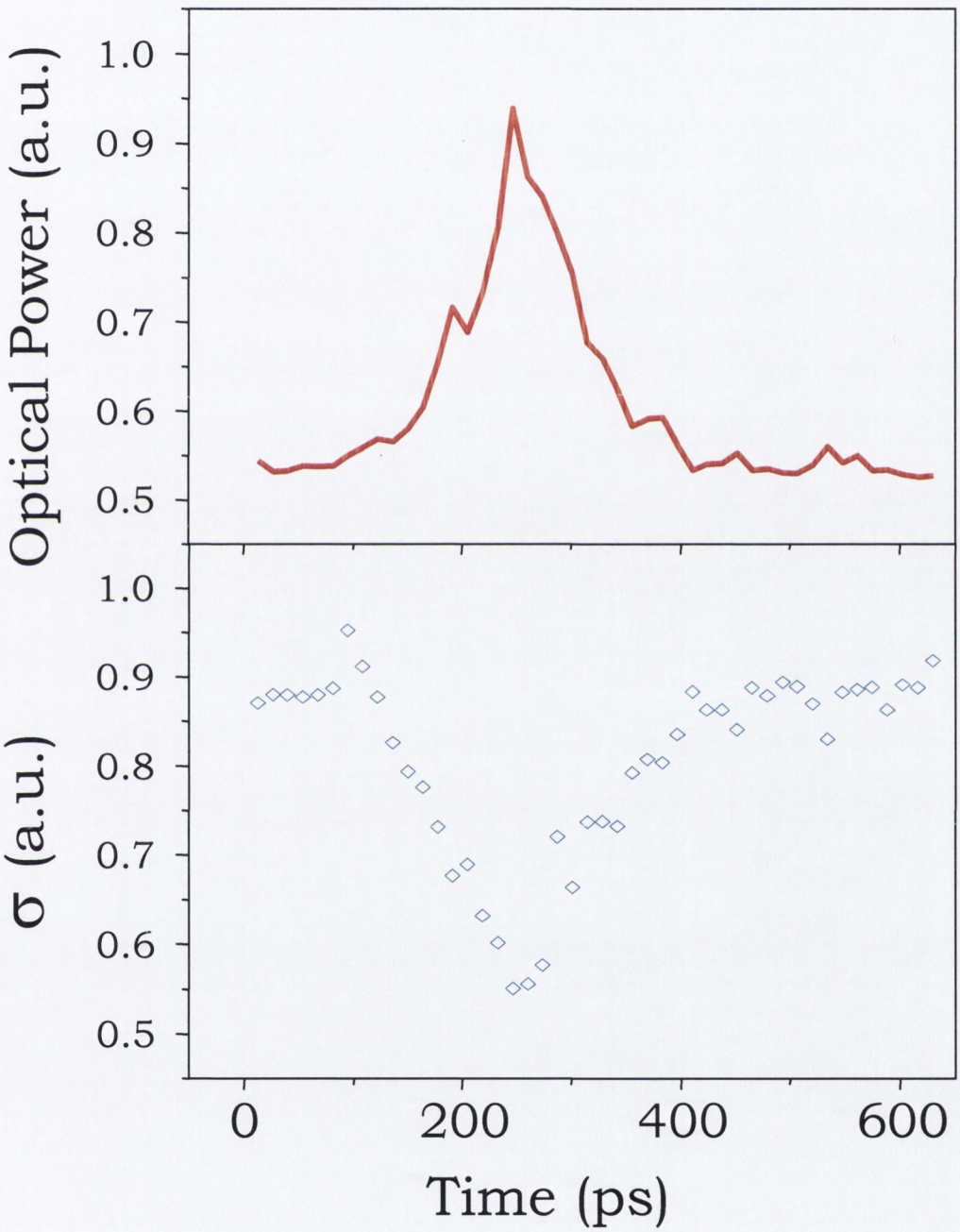


Figure 4-13 Experimental verification of self-focusing, showing the evolution of σ with time for a Sharp LT022MD Laser Diode.

The quantity $\bar{x}$ was used as a convenient reference point. In figure 4-13 $\bar{x}$ was assigned a value of zero. As we can see in this figure it was possible to extract the standard deviation of the of the intensity distribution of the near field waist, σ, with time. The evolution of the optical pulse is shown on the time axis for comparison. It is clear that as the pulse is emitted the optical field becomes focused as seen by the reduction in the standard deviation of the near field intensity distribution. As the pulse is extinguished the field becomes defocused and the standard deviation of the intensity profile waist becomes larger. The reduction in the standard deviation is also evident in the calculated value as seen in figure 4-14 thereby showing direct agreement between experiment and simulation.

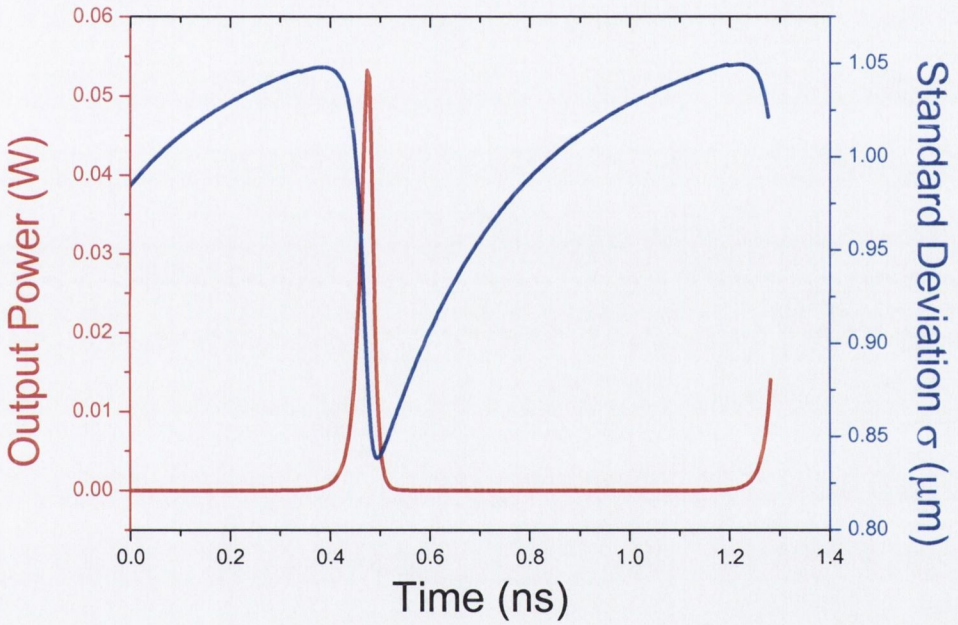


Figure 4-14 Evidence of self-focussing as seen through a reduction in the calculated standard deviation of the position of the field intensity over the emission of a pulse.

4.9 Self-pulsation Variation with Current

Through the calculation of the two-dimensional field, simulations can be performed at currents far in excess of the threshold value. This had not been possible with the effective index method since for higher currents the carrier density rises rapidly on turn on. The optical field is no longer guided for these higher carrier densities within the effective index approximation.

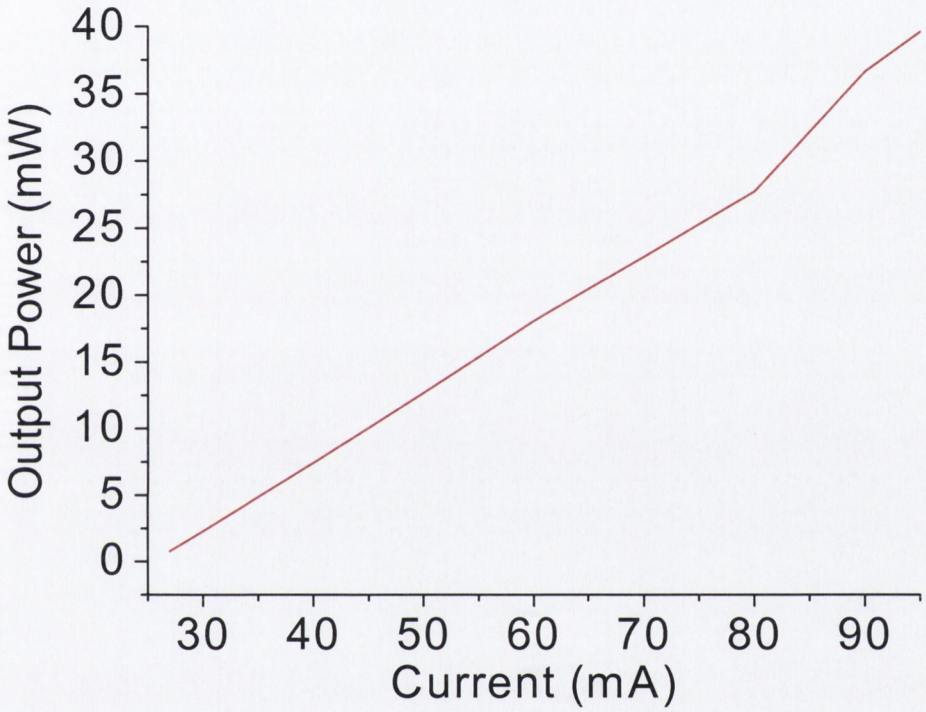


Figure 4-15 Between 27mA and 80mA the LI curve exhibits a linear behaviour whose slope efficiency is 0.51 mW/mA.

The LI curve for the device is shown in figure 4-15. Since the carrier density profiles are initialised to their threshold values, in this case 25.6mA, there are no points on the curve below 27mA. Below 80mA the LI curve exhibits a linear behaviour and the slope efficiency is 0.51 mW/mA.

In order to determine the output power from the front facet the self-pulsation energy is integrated over time. Below 80mA the output energy emitted from the front facet between the pulses due to spontaneous emission is negligible compared with the peak energy emitted from the pulse. As the current is increased the amount of energy

emitted between the pulses increases and since the self-pulsation frequency is higher at these larger currents, the overall contribution of the spontaneous emission between pulses becomes significant. This can be clearly seen in figure 4-16. Even over this 0.2ns timescale there is a large contribution to the integrated output power between the pulses for the 95mA case.

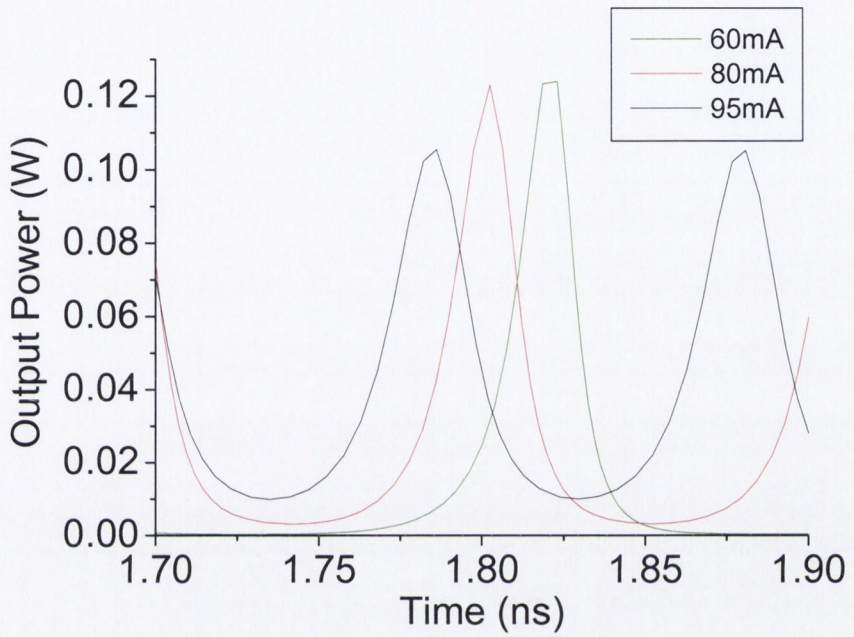


Figure 4-16 Increase in the output power between pulses with increasing current. Increase in self-pulsation frequency can also be observed.

This accounts for the increase in the slope of the LI curve above 80mA. As has been shown experimentally in [10], the self-pulsation oscillation is not simply a destabilised relaxation oscillation since the relaxation oscillation frequency shows a square root dependence on the normalised bias current whereas there is an approximately linear relationship between the bias current and the self-pulsation frequency as seen in figure 4-16. For currents above 95mA, the results of the model are no longer valid. This is a result of the initial boundary conditions within the model. The initial carrier density is set at the value for which the modal gain is zero. On the first iteration of the rate equation, the current injection is set to the bias value. For currents close to the threshold current this causes a rapid increase in carrier density and the initial pulse is emitted faster (time) than the self-pulsation frequency (1/time). At much higher current, closer to 100mA the carrier density rapidly

increases beyond the steady state carrier density rising to $1x10^{25}$ m^{-3}. At this carrier density level, the light in the waveguide is no longer confined. Therefore a method in which the current is increased to 100mA over a longer time period would need to be considered to determine the spatial and temporal behaviour above 95mA.

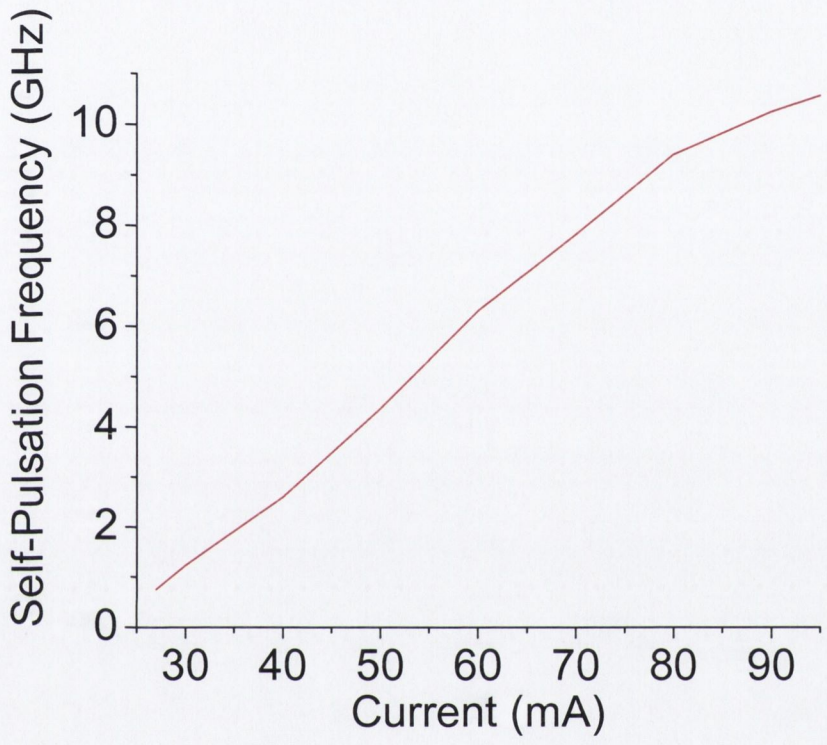


Figure 4-17 The linear relationship between the self-pulsation frequency and the applied current is observed below 80mA

It is clear from the behaviour above 80mA that the laser is going through a transition that if unchanged, would lead to relaxation oscillations at higher currents. Firstly as we can see in figure 4-17 the modal gain variation decreases with current.

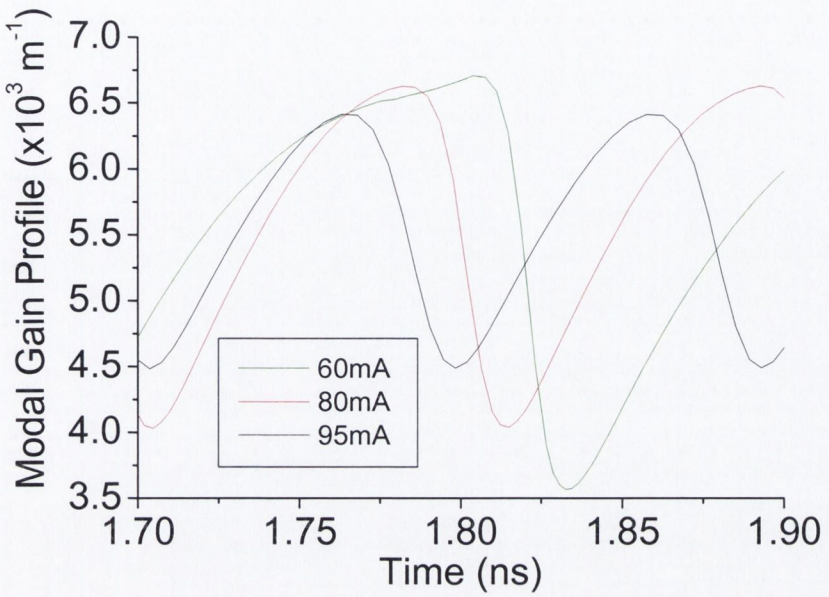


Figure 4-18 Decrease in the range of modal gain variation with current

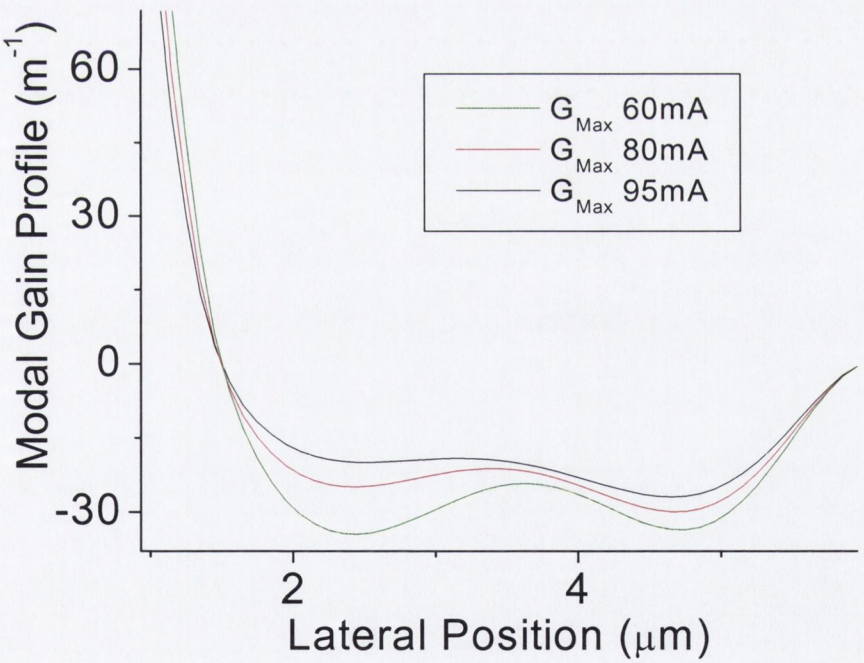


Figure 4-19 Decrease in the modal absorption within one of the absorber regions, with increasing current, taken at the maximum modal gain point.

The modal gain variation at 60mA is 3200m^{-1}, while this decreases to 2380m^{-1} at 95mA. The greater difference between the modal gain at varying currents can be seen

from the modal gain minimum. This behaviour is to be expected, since the modal gain minimum occurs after the emission of the pulse, at a time when the absorbing regions under the blocking layers have saturated. With increasing current the material gain under the current stripe will be larger, accounting for this behaviour. Instead we examine the point in time at which each current reaches its modal gain maximum, just before the emission of a pulse. We can see from figure 4-19 that the amount of modal absorption decreases with increasing current. This can be attributed to the smaller amount of material absorption within this region for higher currents. This comes as a direct result of the larger carrier density for the higher currents in the absorber regions (figure 4-20).

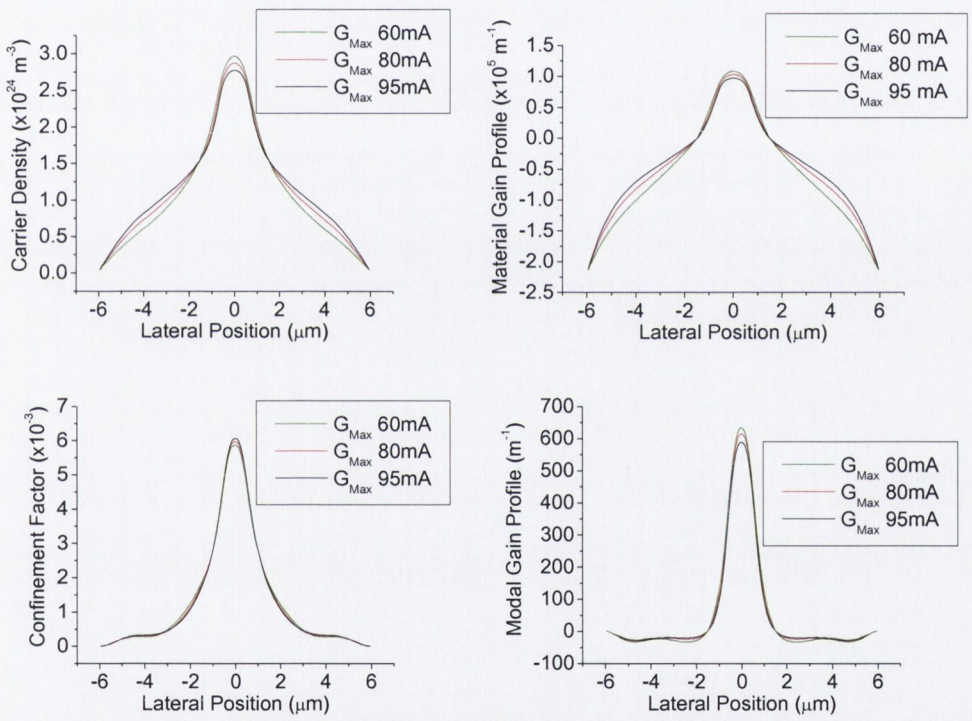


Figure 4-20 Lateral profiles contributing to the modal gain profile. The plots are taken at the point in time when the modal gain is maximum for 60mA, 80mA and 95mA.

Two possible mechanisms can be attributed to the higher carrier density within the absorber sections at higher currents. Firstly the larger amount of spontaneous emission at the higher currents as seen from the significant output power between pulses at 95mA will be absorbed within these sections, prematurely beginning to saturate the absorber sections. Secondly since after the emission of a pulse the

absorbers are saturated the carrier density within these regions is much higher. Since the pulsation frequency is higher and increases with the current, these carriers may not have enough time to be removed through diffusion before the start of the next pulse. The reduction on the range of the modal gain variation is also reflected in the FWHM variation with current as seen in figure 4-21. We see that just above threshold at 30mA the FWHM minimum is close to the value at 60mA but that the maximum value of the FWHM is lower at 30mA. This can be attributed to the fact that at 60mA the peak lateral current value is larger causing the field to spread out widely into the lateral direction. The FWHM variation at 90mA is much lower and this can be attributed to the lowering in the range of the modal gain variation and hence also, the carrier density variation is lowered. This therefore gives rise to the lowering of the FWHM variation as seen in figure 4-22, for current above 40mA. The lowering of the FWHM variation shows that the self-focusing and defocusing effect decreases with current. Since this process enhances the self-pulsation mechanism, this continued trend with current would result in a transition to relaxation oscillations.

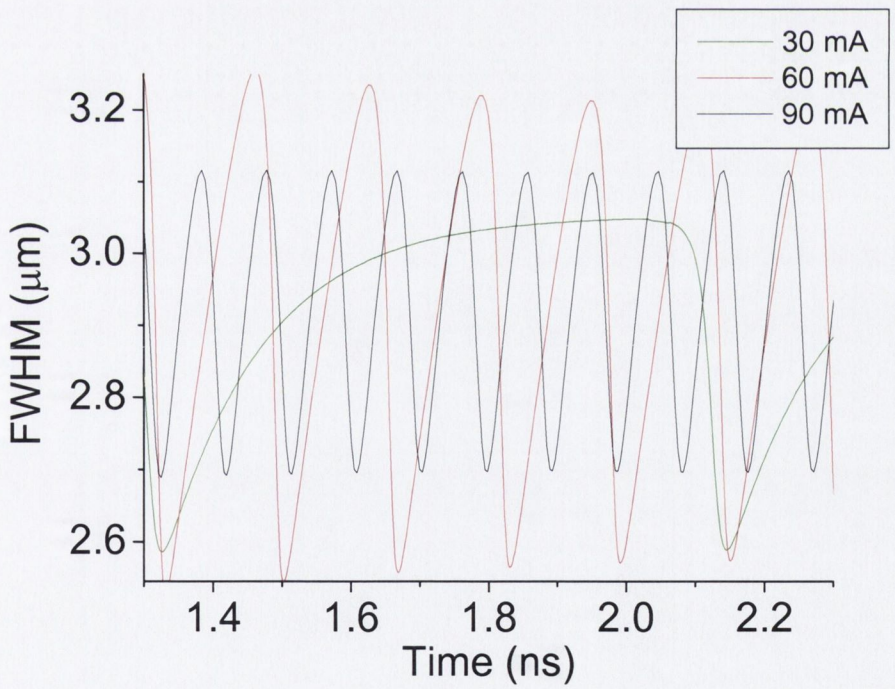


Figure 4-21 Variation in the FWHM of the electric field profile at 30, 60 and 90mA

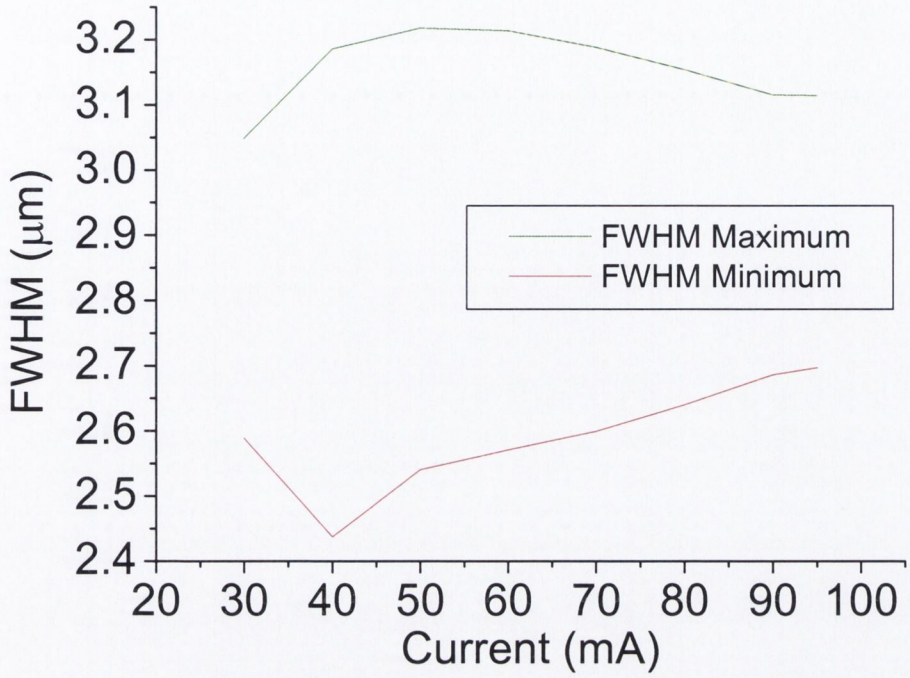


Figure 4-22 The range of the FWHM variation initially increases until 50mA and then decreases consistently with bias current.

In summary we have shown that a fully two-dimensional solution of the weakly guided wavguide is needed to accurately describe the self-pulsation mechanism close to threshold. Also it has been show that this approach is robust enough to determine the effect of current variation on the self-pulsation process and predictions have been made as to the possible causes of the transition to relaxation oscillations at high currents.

References

1 "Lapack Users Guide", E. Anderson, Z. Bai, C. Bishof, S. Blackford, J. Demmel, J. Dongarra, J.Du Croz, A. Greenbaum, S. Hammarling, A. McKenney, D. Sorensen, Third Edition; Society for Industrial and Applied Mathematics 1999.

2 "Eigenvalue computation in the 20th Century", G. H. Golub, and H. A. van der Vorst, J. Comp. Appl. Math. **123,** (1), p 35, 2000.

3 "Simultaneous iteration for computing invariant subspaces of non-Hermitian matrices", G Stewart, Numer. Math. , **25**, p123, 1976.

4 "A look-ahead Lancoz algorithm for unsymmetric matrices" B.N. Parlett, D.R. Taylor, and Z.A. Liu, Math. Comp, **44,** p105, 1985.

5 "Variations of Arnoldi's method for the computing eigenelements of large unsymmetric matrices", Y. Saad, Linear Algebra and Its Applications, **34**, p 269, 1980.

6 "Implicit application of polynomial filters in a k-step Arnoldi method", D. C. Sorensen, SIAM J. Matrix. Anal. Applic, **13,** (1), p357, 1992.

7 "The principle of minimised iteration in the solution of the matrix eigenproblem", W. E. Arnoldi, Quart.Appl. Math, **9,** p 17, 1951.

8 "Accelerating the Arnoldi Iteration-Theory and Practice", H. Thornquist, PhD thesis Rice University, Houston, Texas 1998.

9 "Fixed Polynomial Approximate Spectral Transformations for Preconditioning the Eigenvalue Problem", H. K. Thornquist, Masters Thesis, Computational and applied mathematics department Rice University, Houston, Texas 2003.

10 "Pulse formation and dynamics in Self-Pulsating Semiconductor Laser Diodes", S. A. Lynch, PhD Thesis, Trinity college Dublin

Chapter 5 Self-Pulsation at 1.55μm

5.1 Motivation for Self-pulsation at 1.55μm

Applying the success of the lateral waveguiding self-pulsation design technique in the AlGaAs/GaAs material system to that of the InGaAsP/InP system presents an intriguing challenge. The effects of Auger recombination and inter-valence band absorption on the self-pulsation phenomena as have been described in chapter 2, now need to be considered in this new material system. Lasers operating at 1.55μm are of commercial and technological interest due to their use for long distance fiber optic communication, since silica fibre has a minimum in loss at 1.55μm [1]. As the demand for data bandwidth increases, driven by the phenomenal growth of the Internet, the move to all optical networks is the focus of new technologies. These demands have led to the search for devices that can carry out certain signal processing tasks entirely in the optical domain. Self-pulsating laser diodes have emerged as promising candidates for the implementation of a selection of these functions.

The potential for optical clock extraction and clock distribution by the synchronisation of a self-pulsating laser diode has already been demonstrated [2][3]. Both of these devices were twin section devices the later demonstrated all optical clock recovery from a 5Gb/s RZ data at 1.56 μm in which the self-pulsation was attributed to saturable absorption in the absorber section created through Zn ion doping. The fundamental bandwidth limitations and bit error rates of optical clock extraction for conventional cd laser diodes has been examined in [4]. More recently 80GHz all-optical clock recovery based on the self-pulsating "PhaseComb"(phase controlled optical mode beating) laser has been demonstrated with timing jitter of less than 300fs [5]. The mechanism of self-pulsation in these Distributed Feedback (DFB) lasers differs from those shown here. In one particular design the DFB wavelengths of two of the two DFB sections are spectrally detuned by nearly the stopband width using two gratings with different grating periods. If both DFB sections are operated at lasing conditions and an appropriate phase is chosen through biasing the central phase tuning section, beating type self pulsation with a frequency given by the spectral separation of the two lasing modes is achieved [6]. Another mechanism has been proposed [7] based on the idea that the optical gratings introduce a structurally

dependent differential gain which when negative causes positive feedback and induces self-pulsation. Although single-section self-pulsation lasers in which the self pulsation mechanism is derived from the combination of saturable absorption enhanced by lateral field variation are incapable of producing frequencies to compete with their DFB counterparts they may offer more cost effective lower frequency clock extraction as they are a much simpler design and do not require detuned Bragg gratings or multi-sections with precise etching requirements. Of course single-section self-pulsation lasers have been reported in the earlier years of InGaAsP/InP double heterostructure lasers growth. But as was the case for the initial growth of AlGaAs/GaAs lasers, the self-pulsation can be attributed to the presence of dark-line defects acting as regions of saturable absorption [8][9].

Another key application is the use of self-pulsation laser diodes as fast-tuneable ($\leq 1ns$) frequency-shift keyed (FSK) microwave subcarrier transmitters. It has been shown in the AlGaAs/GaAs system that self-pulsating lasers can be used to transmit frequency-shift keyed data at a rate exceeding 800Mb/s [10]. They were used to construct a local area subcarrier frequency-division multiple access (SFDMA) network supporting 4 users with an optical power margin of 8 dB. Each user can electronically tune in less than 1ns to any of the available subcarrier channels, and can transmit data at a rate of ≥ 150MB/s FSK. In FSK data transmission, the binary digits are represented by two pulse repetition frequencies. These are obtained by biasing the laser to yield a desired self-pulsating frequency, the microwave subcarrier, and then frequency modulated using a small ac signal about this frequency. The advantage of this scheme is that complex and costly electrical superposition circuitry is no longer required to provide the microwave subcarrier. The original benefit for using self-pulsation lasers in optical data storage is still valid, that is the self-pulsating laser shows a high tolerance, low relative intensity noise to optical feedback. This advantage is applicable in these new applications at 1.55μm since it removes the need for including optical isolators within the system to reduce optical feedback and as described in [11] the problem of optical beat interference diminishes as the laser becomes less coherent.

5.2 Consideration Factors for 1.55μm Self-Pulsation Laser Design

5.2.1 Material Properties of the InGaAsP/InP System

AlGaAs/GaAs	InGaAsP/InP
780nm	1.55μm
Large Refractive Index Ratio	
Differential Index $\frac{dn}{dN}$ ($x10^{-26}$) m^{-3}	
-1.2	-2.8
	Auger Recombination and IVBA

Table 5-1 A comparison of the contrasting properties of the AlGaAs material with GaAs substrate and the InGaAsP material with the InP substrate

Currently the material of choice for this type of long wavelength emission is InGaAsP lattice matched to InP substrates although new materials offering lower threshold and higher differential gain such as InGaNAs/GaAs have been demonstrated theoretically [12]. The use of these novel materials in which the benefits are a result of the incorporation of nitrogen giving a larger electron effective mass, is not yet widespread mainly due to the difficulties with the growth of the materials. In designing a structure based on the principles learned in the AlGaAs/GaAs system some notable differences need to be considered. Unlike the GaAs substrate, InP has a wider bandgap than the active region and therefore has the advantage that none of the lasing light is absorbed within the substrate. The refractive index ratio between InGaAsP/InP is much lower than the ratio in the AlGaAs/GaAs material system, as has been discovered by researchers in trying to obtain high reflectivity mirrors in VCSEL's [13]. One other important factor in waveguide design is that the differential index $\frac{dn}{dN}$ in InGaAsP is over twice that of AlGaAs at $-2.8\times10^{-26}m^{-3}$ [14]. Taking these considerations into account InP represents an ideal material to be used in the blocking layer since it has the highest refractive index difference to that of the active region $In_{0.532}Ga_{0.468}As$ allowing one to vary the cladding layer index while at the same time ensuring that the

optical field will be confined sufficiently. The In content in the cladding region will be adjusted so that the refractive index step in the lateral direction is low enough to ensure that the carrier density dependent optical field fluctuations will enhance the saturable absorption effect for that particular design. High differential gain contrast between the gain and absorption regions is a desirable trait that enhances the saturable absorption effect. Since the differential absorption is higher than the differential gain, an increase in carrier density dN will result in a larger decrease in absorption than an increase in gain. The advantage of using quantum well over bulk active region are that the differential gain is increased [15], and there is a reduction in the Auger coefficient and inter-valence band absorption for quantum well structures [16].

There were two types of structure considered for obtaining self-pulsation and they differ in the placement of the saturable absorption region. The structure shown in figure 5-1(a) is an example of a design that has been applied successfully in the AlGaInP/GaAs material system for self-pulsating visible lasers operating at 650nm [17]. Since the diffusion constant for AlGaInP is much lower than either AlGaAs or InGaAsP the lateral diffusion of carriers into the absorption regions of the lateral structure with be considerably reduced, reducing the saturable absorption effect and hence a quantum well region was placed the spacing-layer distance above the active region so that the transverse field overlaps this region. The lateral effective index step is much larger than in figure 5-1(b) since the lateral field is no longer required to spread out laterally. Thus the transverse guiding is enhanced and the astigmatism in the optical field is reduced as can be seen from the schematic in figure 5-1(a).

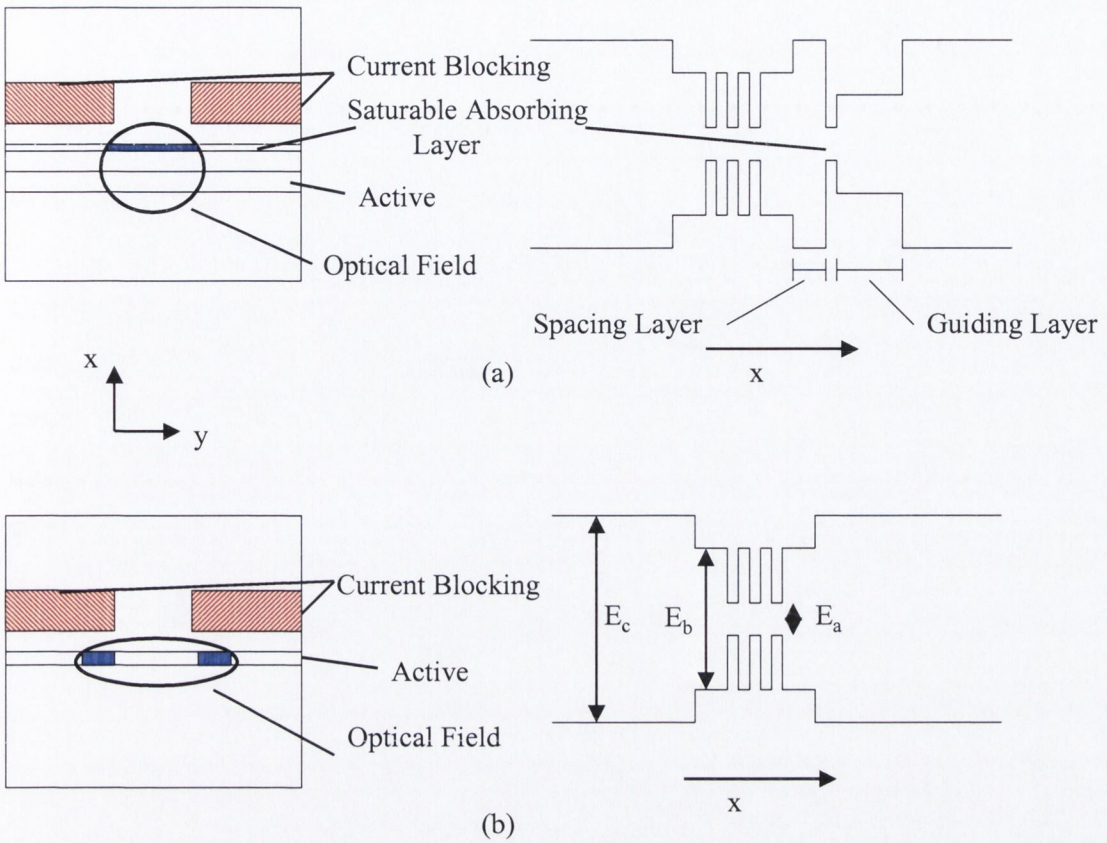


Figure 5-1 Schematic structure and band diagram along the transverse direction for (a) comprising a layer above the active layer in which the saturable absorbers are located and (b) the same triple quantum well structure but in which the saturable absorbers are formed within the active region.

Once the design is optimised, the enhancement of the saturable absorption as a result of the carrier dependent field variation has the potential to offer self-pulsation by a more effective means than for the saturable absorbing layer design. Within the transverse absorber structure, self-pulsation can be controlled by varying the spacer and guiding layer distance to ensure enough modal absorption is present. This is not enough to ensure self-pulsation, the carrier lifetime within the absorption layer must be low and this is achieved through the doping of this layer [18][19]. Although achieving self-pulsation in the lateral absorber structure presents a greater challenge since the effective index profile needs to be controlled to the accuracy of $1x10^{-3}$ and the self-pulsation will vary with the current stripe width, the advantages of the lower threshold carrier density warrant such an investigation. The rest of this chapter investigates the spatial and dynamic effects that arise from the lateral absorber design as shown in figure 5-1(b).

5.3 Optimisation of the Active Region

The quantum well design consists of 5.5nm $In_{0.532}Ga_{0.468}As$ well/wells lattice matched to InP with a bandgap wavelength of λ_g = 1.55μm, lattice matched to 20nm thick $In_{0.735}Ga_{0.265}As_{0.575}P_{0.425}$ barriers of band gap wavelength of λ_g = 1.3μm. Our aim in choosing the number of quantum wells within the device is to have a low operating carrier density profile, thereby reducing the losses due to Auger recombination. As can be seen in figure 5-2 the single quantum well offers the highest differential gain and lowest transparency carrier density $N_o = 1.9x10^{24}$ m^{-3}. But a single 5.5nm quantum well offers very little optical confinement, so although the peak gain is larger at low carrier densities the modal gain is not sufficient to overcome the losses of a standard 250μm laser. The threshold condition is given by,

$$G = G_{th} = \frac{1}{2L}\ln\left(\frac{1}{R_f R_r}\right) + \frac{\iint_{Active}(c_n + c_p)N|\phi|^2\,dxdy}{\iint_{Total}|\phi|^2\,dxdy} + \frac{\iint_{Active}|\phi|^2\frac{d\alpha}{dN}Ndxdy}{\iint_{Total}|\phi|^2\,dxdy} \qquad (5.1)$$

The first and second terms on the right hand side are the same in the AlGaAs/GaAs system, representing the mirror loss and free carrier absorption respectively. The final term represents the loss due to intervalence band absorption (IVBA), where $\frac{d\alpha}{dN}$ is the intervalence band coefficient. But unlike the case for the AlGaAs/GaAs system there is no loss term due to absorption with in the top-contact and substrate layers. What is evident from the intervalence band absorption term is that as the confinement factor increases, so too will the intervalence band contribution as has been shown experimentally in [20]. This is something that needs to be borne in mind when considering the use of a large number of quantum wells.

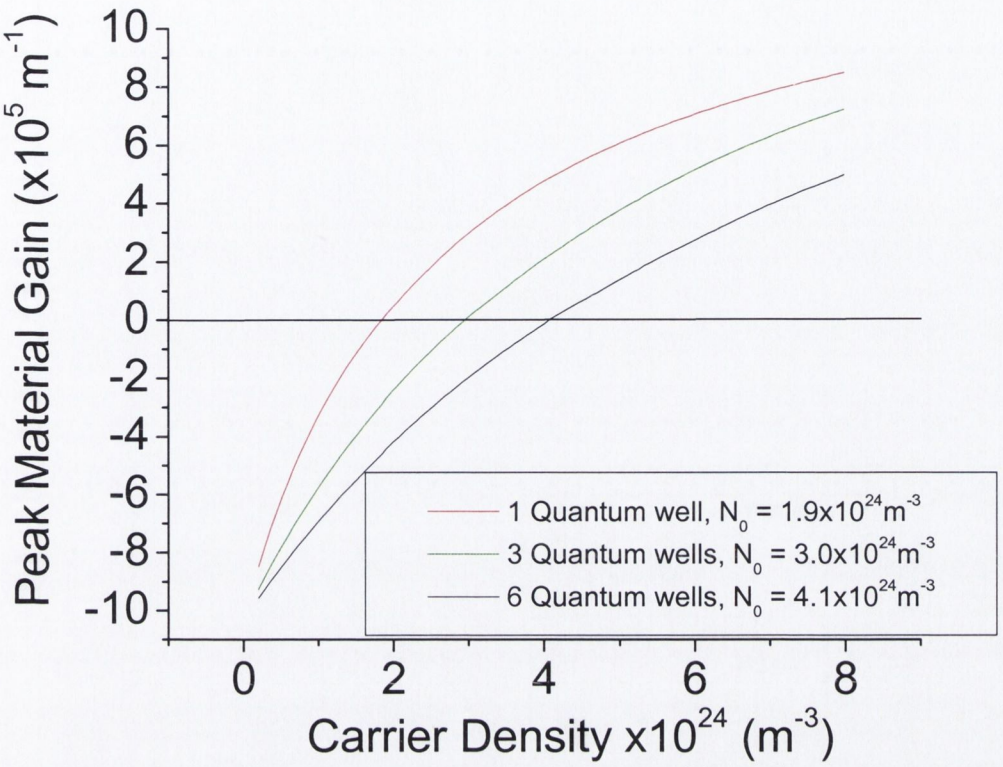


Figure 5-2 Variation in peak material gain with carrier density for single, triple, and 6 quantum wells. All three gain profiles are taken for at a wavelength of 1.54 μm where N_0 represents the transparency carrier density.

What is noticeable from figure 5-2 is that there is an increase in the transparency carrier density with quantum well number. Since the quantum wells are 5.5nm wide and the barriers are 20nm thick we can treat the quantum wells as separate entities and ignore the coupling of the electron and hole wavefunctions between the wells. If we assume that all wells have uniform injection, then for a given injection current, the same number of carriers is divided between a greater number of wells increasing the overall transparency carrier density with well number. As mentioned previously, the material gain should not be considered in isolation. The variation of the coupling with the optical field is important when considering laser performance. For section A (under the current Stripe) of the waveguide, the transverse optical confinement has been calculated in order to compare the confinement factor of the single, triple, and six quantum wells.

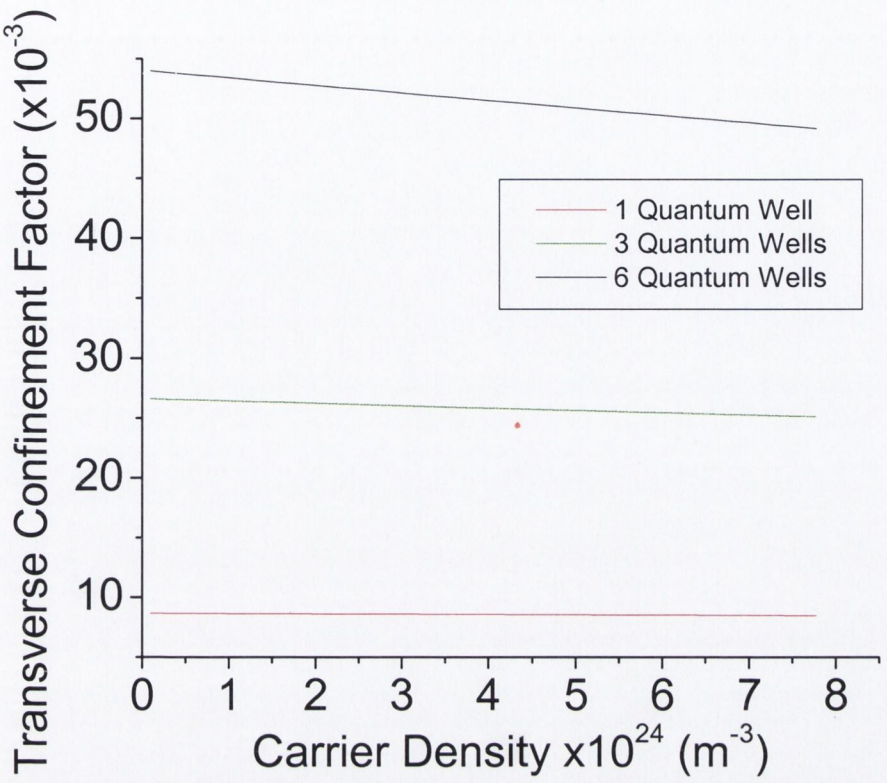


Figure 5-3 Transverse confinement factor variation with carrier density for the three quantum well cases

We can see from figure 5-3, there is a linear increase in the transverse confinement factor with quantum well number. This is understandable since the optical field can be assumed to be constant over the width of the quantum well region. The rate of change of the confinement factor with carrier density is also greater for the larger number of quantum wells. The reduction in refractive index with carrier density is only calculated in the well regions; therefore for the larger the number of wells the greater active area that can be influenced by the carriers. This can be seen more clearly from the rate of change of the effective index with carrier density for the three quantum well cases, see figure 5-4.

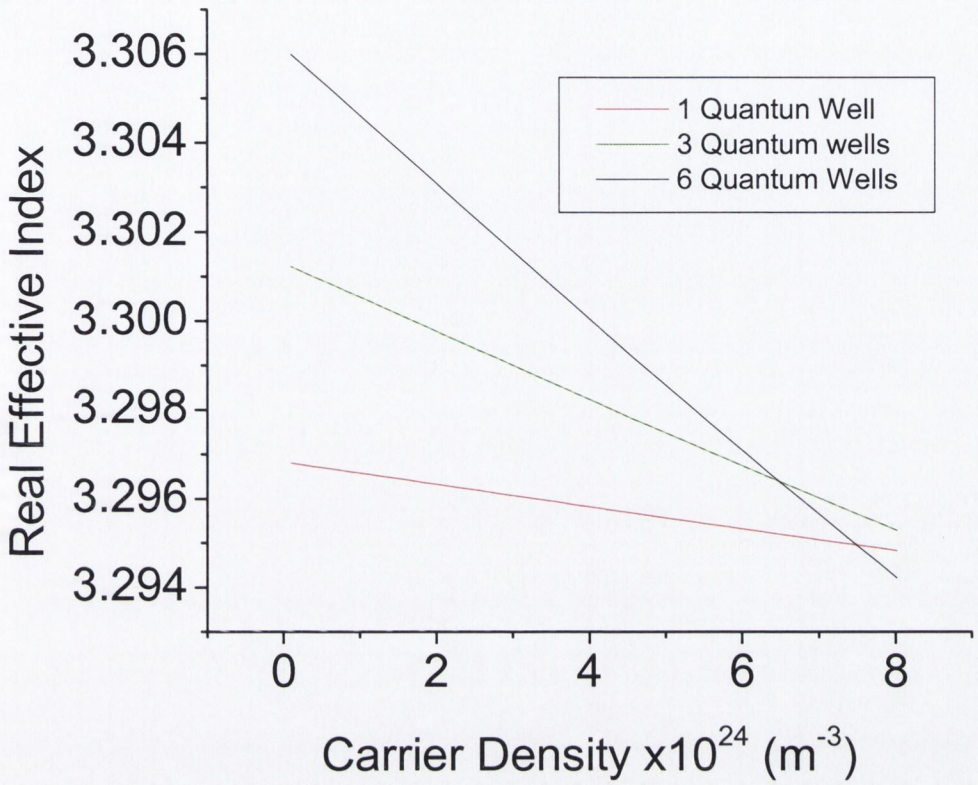


Figure 5-4 Real effective index variation with carrier density in region A for the three quantum well cases

Another consequence of the increase in effective index with quantum well number is that the lateral field variation with carrier density will also increase with quantum well number. Thus, the saturable absorption enhancement will be greater for the larger well numbers. In order to examine the spatial and dynamic effects of the various structures the carrier density rate equation needs to be adjusted to account for the non-radiative Auger effects, the cubic term in equation (5.2). As Auger recombination is a non-radiative effect, it results in a decrease in the number of carriers available for radiative transitions.

$$\frac{dN}{dt} = \frac{J(y)}{qd_a} - R_{sp}(y) - C_{Auger}N(y)^3 - \frac{N(y)}{\tau_{nr}} + D_a\frac{\partial^2 N}{\partial y^2} \qquad (5.2)$$

Due to the very low confinement factor of the single quantum well, lasing can only be achieved by increasing the length of the device, thereby reducing the mirror loss term. The operating current of the single quantum well device in figure 5-5 is 65mA and it is clear that self-pulsation has not been achieved. This can in part be attributed to the weak lateral field variation as can bee seen from the 0.15μm change in the FWHM lateral field profile.

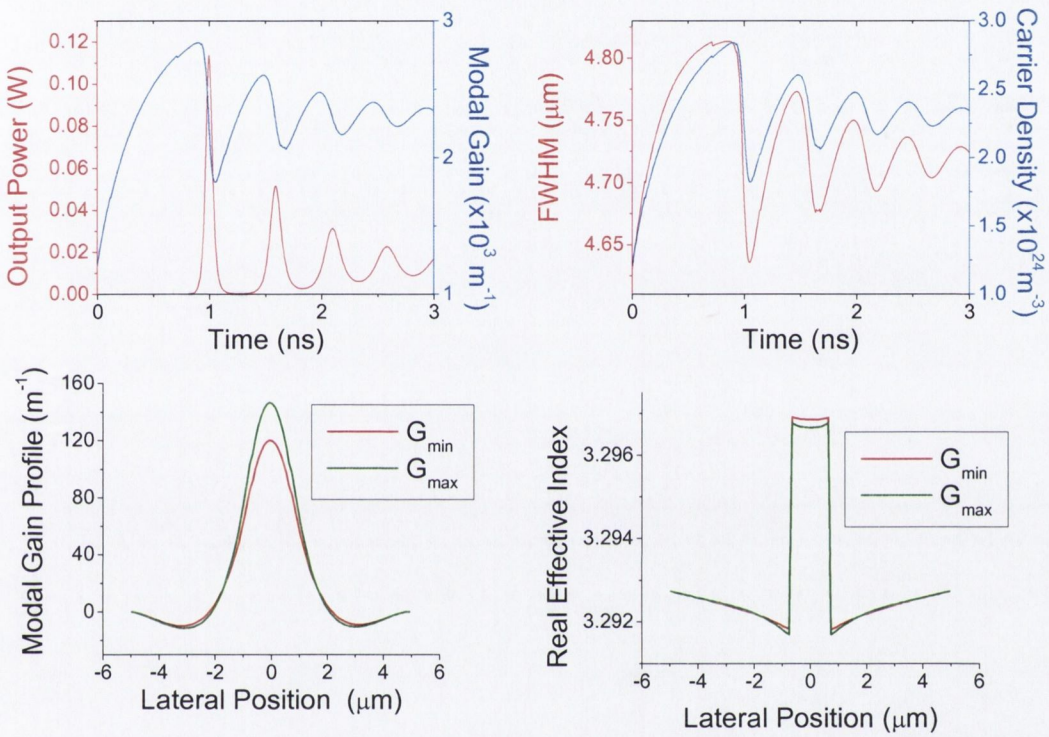


Figure 5-5 For the single QW structure at a current of 65mA and device length of 500μm. Top Left: The transient behaviour of the output power and modal gain. Top Right: FWHM and carrier density variation. Bottom Left: The modal gain profiles, and Bottom Right: Real effective index profile. They are shown at the points in time for which the modal gain is at its maximum and minimum.

The benefit of the lower transparency carrier density value for the single quantum well is that a peak operating carrier density of 2.8×10^{24} m^{-3} for the device is achieved and so Auger recombination is relatively weak. If one was interested in optimising a device for the lowest threshold current then a long device with a single quantum well would best meet those requirements [21]. Since in that case the frequency behaviour would not be of prime consequence and there would be no modal absorption lowering

the modal gain value. In order to achieve self-pulsation in these devices the effective index profile would need to be further reduced in order to enhance the saturable absorbers. This increase in absorption would require a further increase in the device length and perhaps the operating current making these devices unattractive as self-pulsators.

In the six quantum well case, although the confinement factor is six times larger than the single quantum well, the large transparency carrier density of 4.1×10^{24} m^{-3} means that the peak operating carrier density is close to the value at which the transverse waveguide no longer guides light in the separate confinement heterostructure region. That is for carrier densities > 8.0×10^{24} m^{-3}. As Auger recombination is proportional to the cube of the carrier density the losses are too great for this type of structure. Therefore a compromise is needed between the low transparency, high differential gain, offered by the single quantum well and the increased confinement offered through the use of multi-quantum wells. The triple quantum well structure offers a low enough operating carrier density due to a transparency carrier density of 3.1×10^{24} m^{-3}. The optical confinement is large enough that the length of the device does not need to be increased beyond 450μm in order to overcome the mirror losses. The optimisation of the waveguiding parameters for the triple well design will now be described.

5.5 Design Parameters for the Triple Quantum Well Active Region

5.5.1Transverse Waveguiding

As has been outlined for the single quantum well case, it is important to confine the optical field in such a manner that the maximum interaction of the field with the quantum well active region can be achieved. Certain parameters have already been fixed by the choice

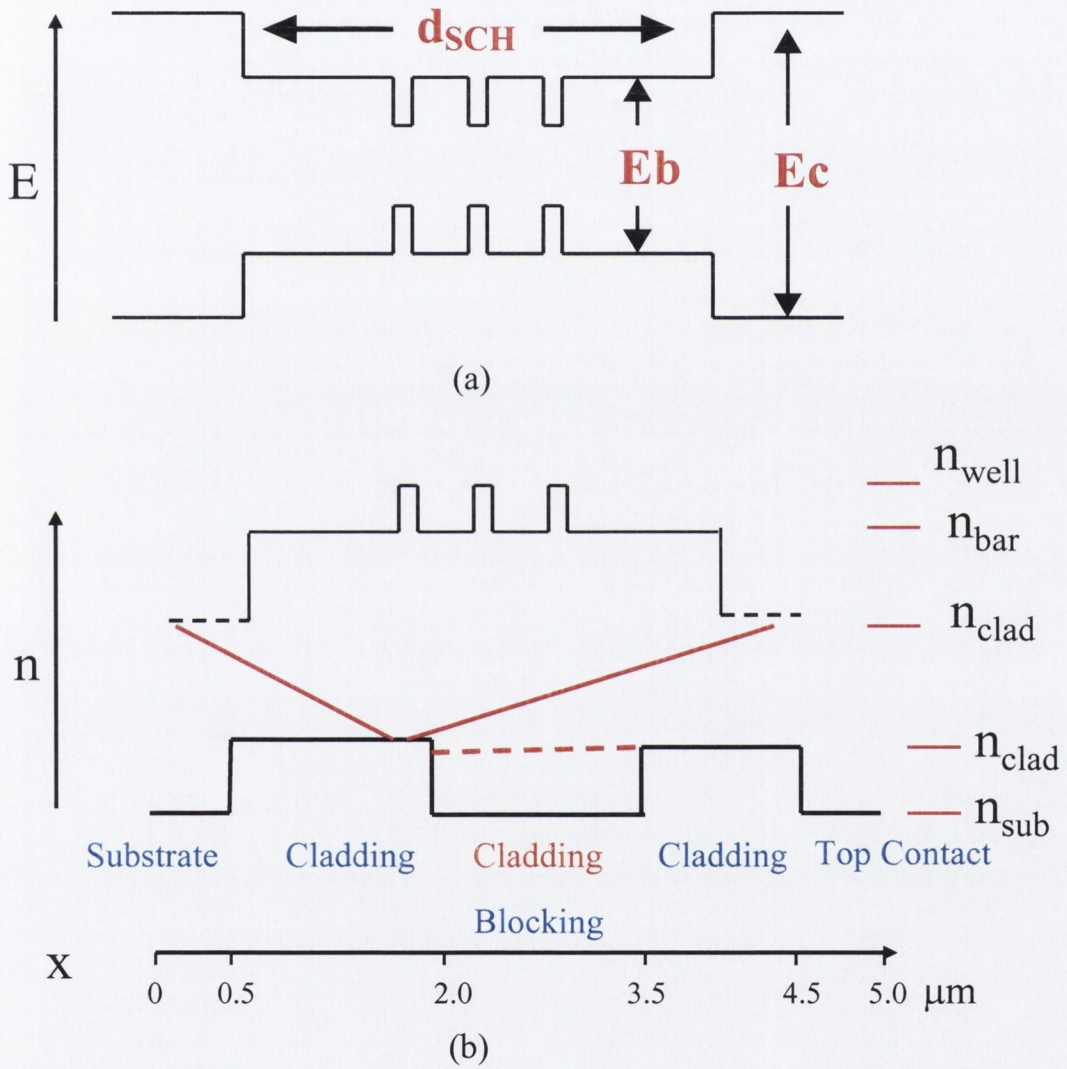


Figure 5-6 Band diagram of the triple quantum well Separate Confinement Heterostructure (SCH) (a), and the transverse refractive index profile, with an enlarged profile of the SCH region, in which the dotted red line indicates the refractive index profile in region A (under the stripe)

of a latticed-matched triple quantum well structure emitting at 1.5μm. These include the quantum well widths, barrier widths, and energy gaps. In order to ensure that the epitaxial layers are lattice matched to InP there is a relationship between the gallium and arsenide mole fractions in $Ga_xIn_{1-x}As_yP_{1-y}$ [22], namely,

$$x = \frac{0.1894y}{0.4184 - 0.013y} \tag{5.3}$$

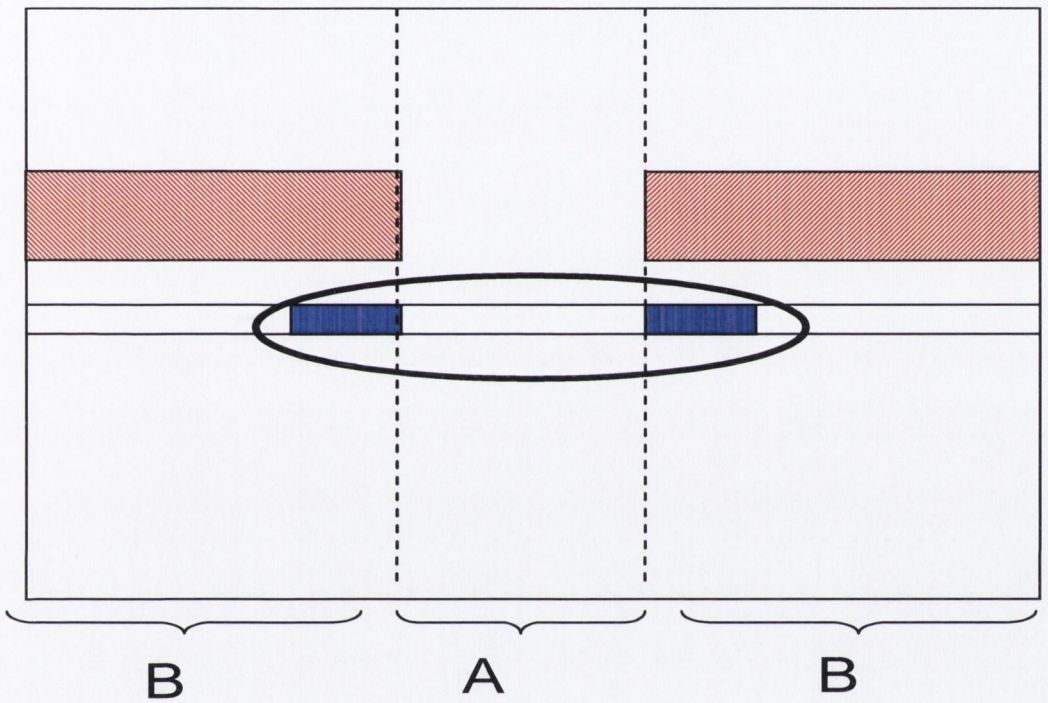


Figure 5-7 Schematic structure of the chosen design in which the saturable absorption regions lie within the active region. The area directly under the current stripe id denoted as A and that under the current blocking layers is donated as B.

Using equation (5.3), the Ga fraction within the cladding layer can be varied to raise or lower the refractive index between region A, under the current stripe, and region B, which includes the current blocking layer. The remaining parameter that can be varied in order to maximize the transverse confinement is the width d_{SCH} of the separate confinement hererostructure (SCH) region. As seen in figure 5-6(b) the SCH region is composed of three quantum wells of refractive index n_{well} and two barrier regions 20nm in width of refractive index n_{bar}. The surrounding barrier regions length can be adjusted to maximize the confinement of the optical field within the well region. Initially, the outermost barriers were set at the width of 20nm. This resulted in a combined width of d_{SCH} = 0.0965 μm.

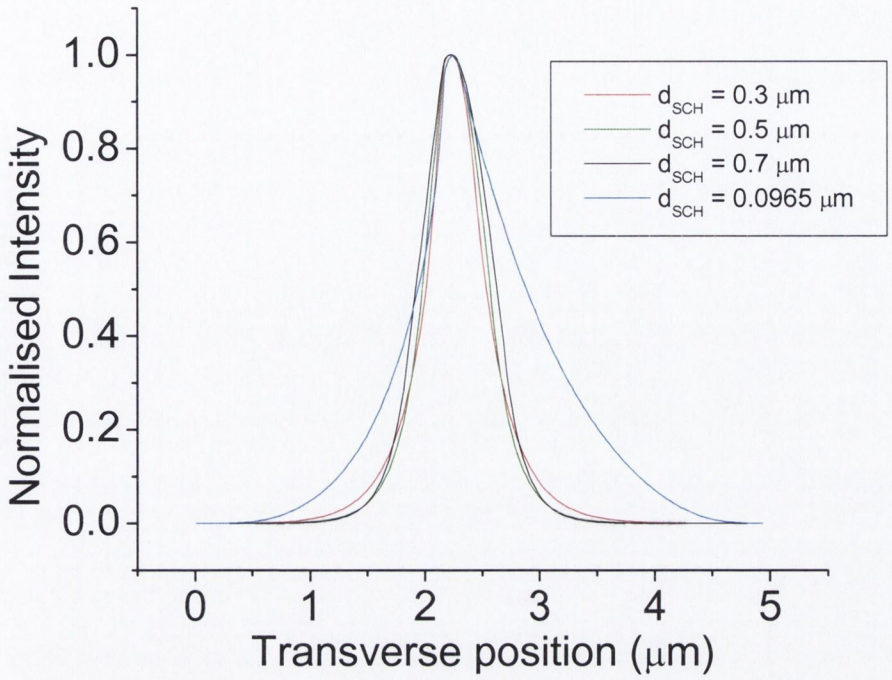


Figure 5-7 Variation in the transverse intensity profile with the length of the separate confinement heterostructure region d_{SCH} in region A.

This value gives the poorest confinement of the field in the transverse direction as seen from the normalised intensity profiles for region A, as shown in figure 5-7. As the width of the SCH region is increased the field intensity is concentrated towards the well regions. This is a result of the modal confinement provided by the higher and now wider SCH refractive index region. A similar effect appears for region B, but what is clearly evident is the asymmetry in the intensity profile. The light is confined more strongly within the cladding region above the substrate than in the lower refractive index InP blocking layer and the field becomes more confined as d_{SCH} increases. The variation in the field intensity between d_{SCH} = 0.3μm and 0.7μm is much less than between the narrow d_{SCH} = 0.0965μm and the 0.3μm case. To analyse the optimum SCH width it is necessary to compare the transverse confinement factors for these structures.

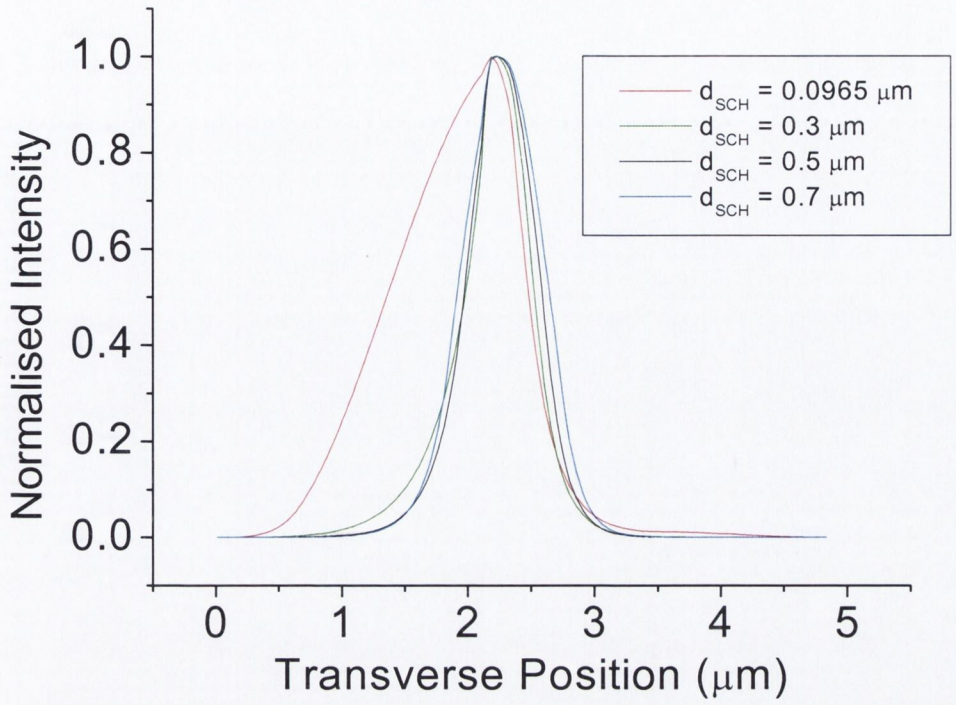


Figure 5-8 Variation in the transverse intensity profile with the length of the separate confinement heterostructure region d_{SCH} for region B

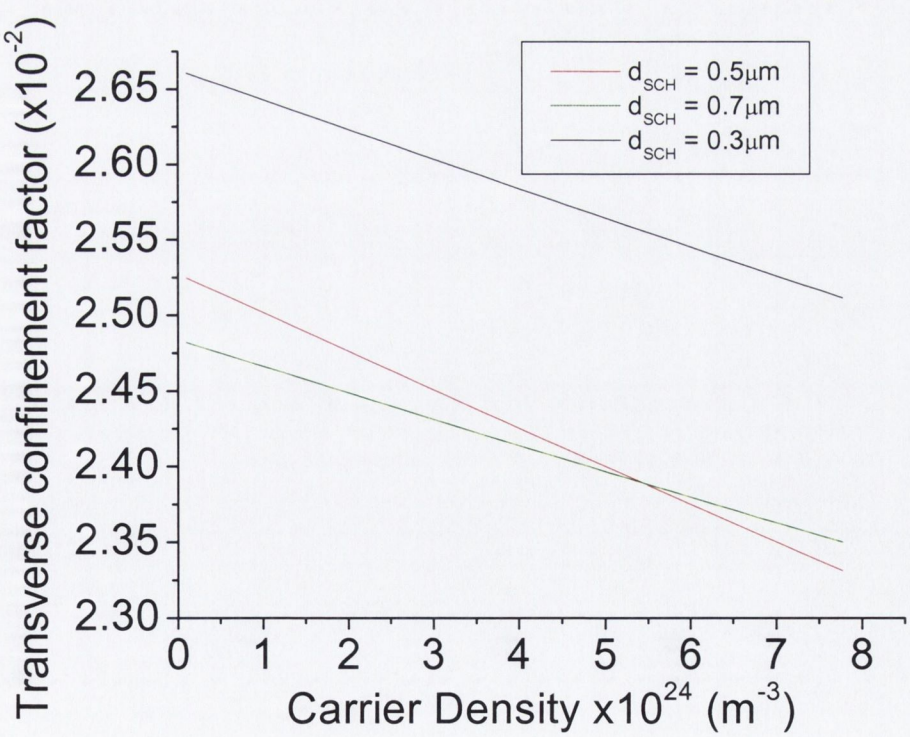


Figure 5-9 Transverse confinement factor variation with carrier density in the well regions

As is shown in figure 5-9, a SCH width of 0.5μm is the optimum value for the transverse confinement factor for the triple quantum well case. The increase in carrier density in the active region reduces the refractive index thereby causing the field to spread out reducing the transverse confinement factor. The Ga mole fraction within the cladding layer is adjusted so that the effective step is large enough to remain above cutoff for the operating carrier density levels of the device while allowing the field spread into the lateral absorption regions, where the saturation is enhanced through the lateral field variation. An effective index step of $6x10^{-3}$ is required to overcome the larger differential index in the InGaAs system (see figure 5-10). This step is considerably larger than in the AlGaAs case.

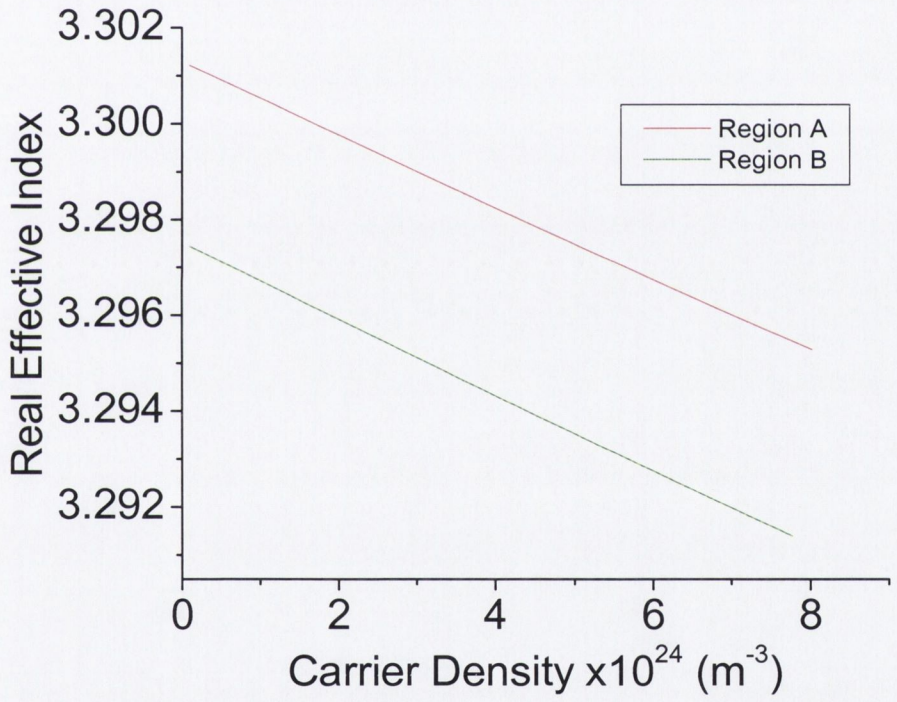


Figure 5-10 Effective index variation with carrier density for the optimised d_{SCH} structure giving an effective index step of $6x10^{-3}$.

5.6 Temporal and Spatial Dynamics

5.6.1 Consideration of Loss Mechanisms (IVBA and Auger Recombination)

Within the computational algorithm, the optimised transverse waveguide parameters for the d_{SCH} = 0.5μm structure was saved within a database so that through polynomial interpolation, the real and imaginary effective index variation, as well as the transverse confinement factor could be determined for a carrier density (N) where, $1\times10^{23}m^{-3} \leq N \leq 8\times10^{24}m^{-3}$. It was found that for carrier densities $>8\times10^{24}m^{-3}$ the reduction in refractive index within the well regions was such that the zeroth order mode could no longer be sustained. This places an upper limit on the current density that can be injected into the active region while maintaining single transverse mode operation. The IVBA profile across the active region has been plotted in figure 5-11 using the IVBA term in equation (5.1). The summation of which gives the intervalence band absorption loss at the minimum (1396.91m^{-1}) and maximum (1583.67m^{-1}) modal gain points.

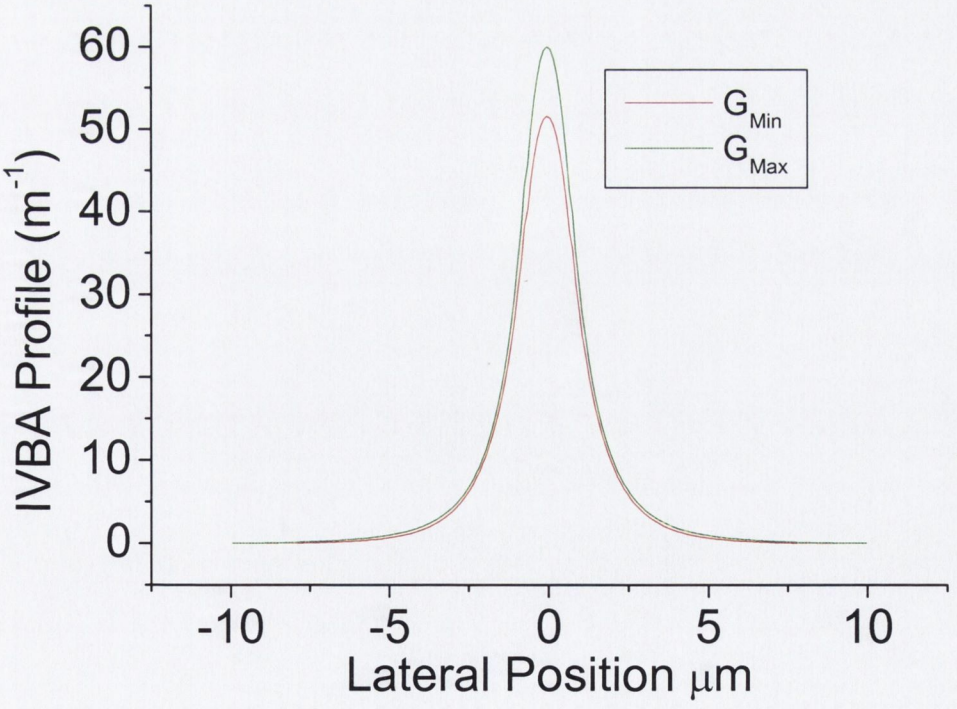


Figure 5-11 The IVBA profiles taken at the modal gain minimum and maximum points.

Originally self-pulsation was simulated with the omission of the IVBA effects. The device length was 275μm. The threshold current was found to be 27mA. At an operating current of 30mA the self-pulsation frequency was 1.71GHz. The IVBA losses at threshold were found to be $1400m^{-1}$. The device length was increased to 450μm in order to reduce the mirror loss contribution. Maintaining the same level of current injection due to the increased length the threshold current increased to 42mA. The value used for the Auger coefficient in equation (5.2) is $C_{Auger} = 3.0x10^{-41}m^6s^{-1}$ which lies within the experimental bounds for a 5.5nm well [23]. It was found that there is a slow decrease in the Auger coefficient with quantum well width. It has been proposed that if the leading Auger contribution is due to a valence band process, the reduction in the Auger coefficient with decreasing well width may be attributed to an increase of the ratio of the fundamental band-gap energy E_g over the split-off gap Δ_0 due to different quantisation of the conduction and split-off valence bands.

Symbol	Description	Value	Unit
L	Device Length	450	μm
W	Stripe Width	1.2	μm
d_{Well}	Well Width	5.5	nm
n_{well}	Well Number	3	
d_{Bar}	Barrier Width	210	nm
d_p	Spreading Layer Width	0.15	μm
D_{ab}	Ambipolar Diffusion	$1.464x10^{-3}$	m^2s^{-1}
C_{Auger}	Auger Coefficient	$3.0x10^{-41}$	m^6s^{-1}
α_{IVBA}	IVBA Coefficient	$1.4x10^{-20}$	m^2
X_{well}	Quantum Well In Mole fraction	0.53	
X_{clad}	Cladding Layer In Mole Fraction	0.9	
X_{bar}	Barrier Layer In Mole Fraction	0.74	
α_{GaAs}	GaAs Absorption Coefficient	$1.0x10^6$	m^{-1}

Table 5-2 List of parameters for the InGaAsP 1.55μm structure all the remaining parameters are the same as that shown in table 3-1.

5.7 Validity of the Effective Index Method

As has been outlined in chapter 3 the effective index approach to the solution of the two-dimensional wave equation is only valid for guided modes that decay to zero at infinity. The effect of applying this method for waveguides bordering on an anti-guiding effective index profile are that artificial side lobes begin to appear due to the constraint that the electric field at the computational boundary is zero. As can be seen from the effective index profile in figure 5-12 the central effective index step in the region under the current stripe rises significantly above the highest boundary values in the regions under the blocking layers.

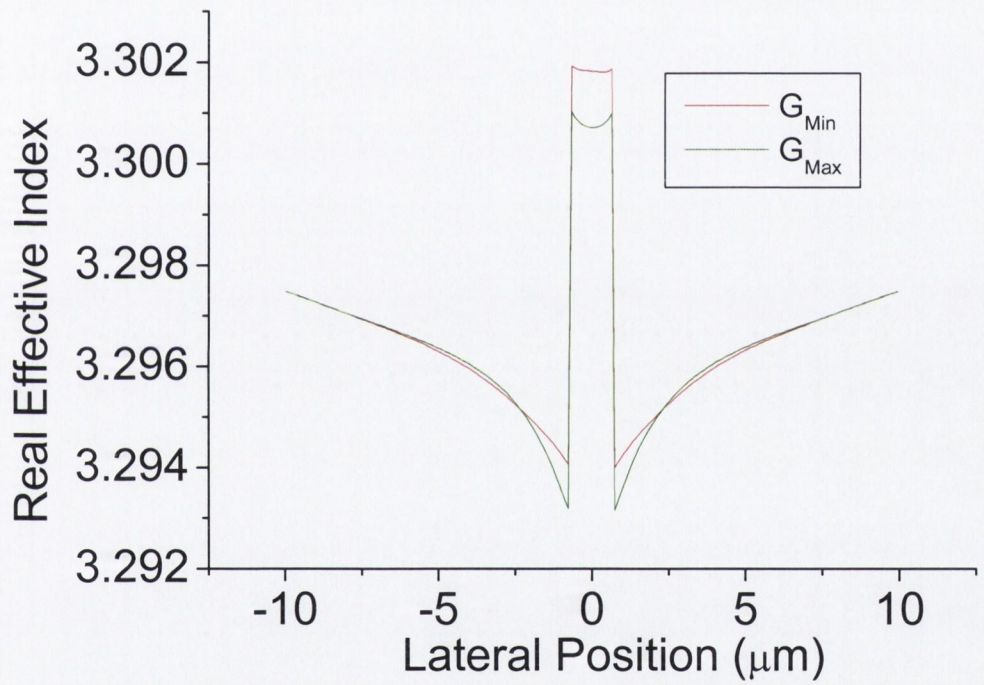


Figure 5-12 The real effective index variation for the InGaAsP laser with a stripe width W = 1.4μm and an operating current of 30mA.

The requirement that the effective index central step rises above the maximum effective index in the side region is not enough to ensure a decaying lateral electric field profile as can bee seen from figure 5-13. Initially, the simulations were carried out with a lateral width L_y = 10μm. This had the effect of forcing the field to zero at the boundaries of the waveguide. This meant that a much larger modal absorption was created due to the high confinement factor in these lateral regions. By extending the lateral waveguide to 20μm while maintaining the same lateral section spacing Δ, it

was found that the field decays to zero at the boundaries. Therefore the use of the computationally efficient effective index method could be successfully applied to the simulation of the 1.55μm structure.

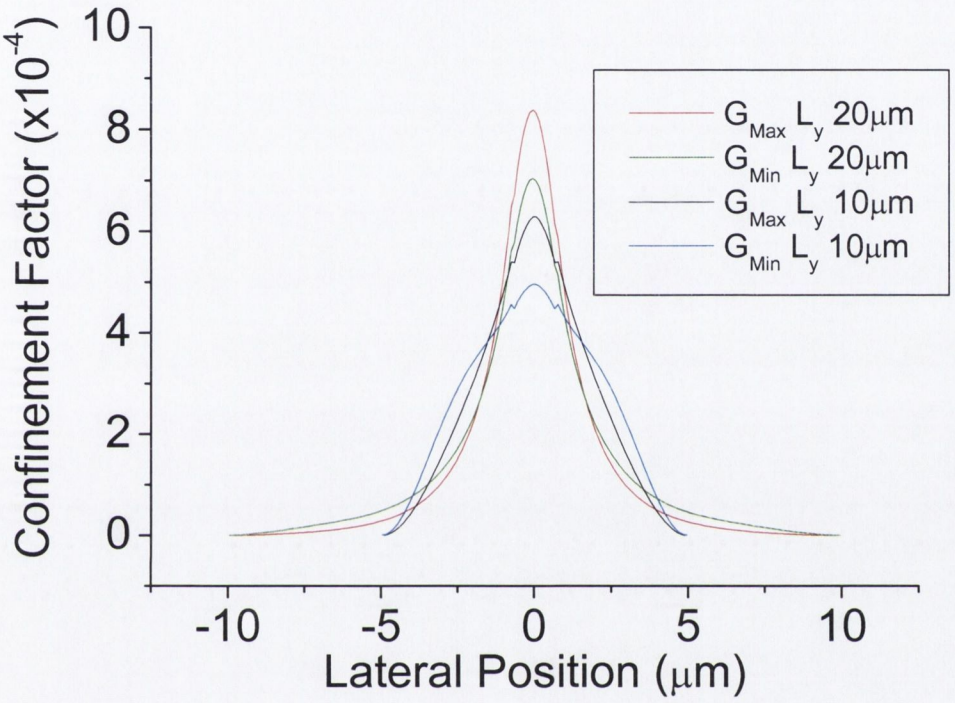


Figure 5-13 Comparison of the confinement factors for the L_y = 20μm and L_y = 10μm lateral waveguides. In both cases the confinement factor for the maximum and minimum modal gain are shown.

5.8 Results and Discussion

Self-pulsation is clearly evident in the evolution of the output energy from the front facet in figure 5-14. The diode bias current is set at 50mA and the self-pulsation frequency is 1.52GHz. In order to examine the spatial and dynamical behaviour, a shorter timescale from 1.51ns to 2.40ns is chosen. This represents the time taken for the modal gain to return to its minimum value. In contrast to the modal gain behaviour seen in the AlGaAs/GaAs system seen in chapter one and two, the modal gain recovers from its minimum value at 1.51ns very rapidly until around 1.7ns at this

point the rate of change of modal gain with time has decreased considerably. The rapid increase in the carrier density followed by a slowdown around 1.8ns is evident.

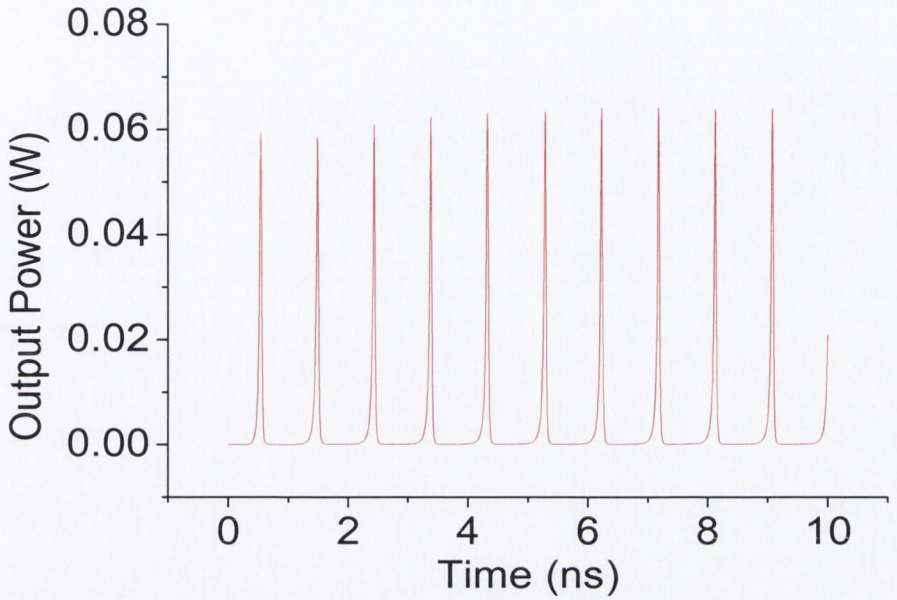


Figure 5-14 Output energy from the front facet of the triple quantum well design including the effects of IVBA and Auger Recombination. The

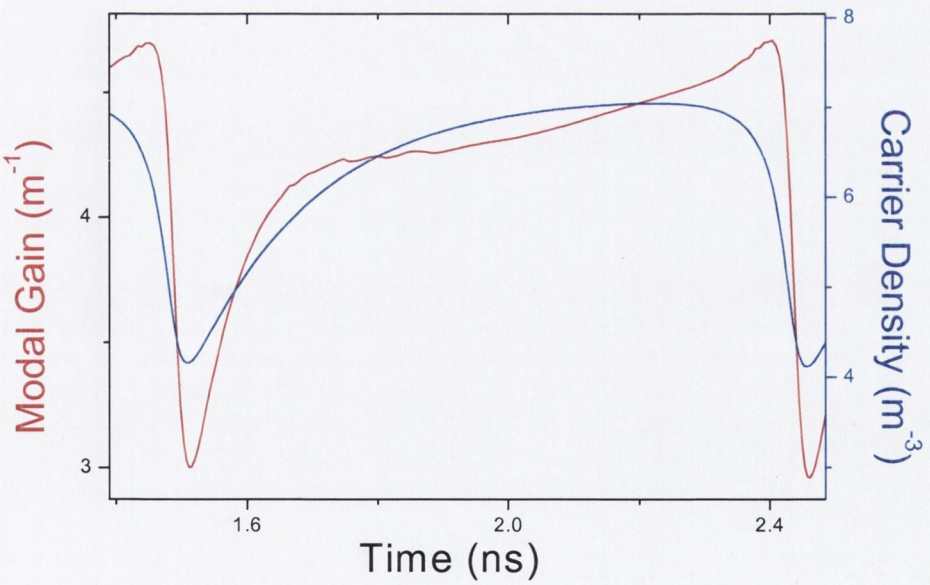


Figure 5-15 Modal gain and carrier density variation within the centremost section over the evolution of one pulse

This effect can be attributed to the non-radiative Auger recombination.

$$\frac{dN(i)}{dt} = \text{.....} - C_{AUGER} N(i)^3 \text{.....} \tag{5.4}$$

The rate of increase of the carrier density decreases rapidly due to the Auger terms cubic dependence on the carrier density. Initially the dominant term is the current injection term $\frac{J(i)}{qd_a}$. This causes a rapid increase in the carrier density, but the Auger term becomes dominant around 1.8ns. At this point the photon number begins to increase as the modal gain overcomes the threshold value, which is 4230 m^{-1} at that point in time. It should be noted also that the threshold modal gain value varies over time since the IVBA and free carrier absorption vary with the carrier density and confinement factor. The rise in modal gain value beyond this point is due to the saturation of the absorber regions. The carrier density within the centremost section begins to decrease around 2.3ns, which is earlier than would be the case if Auger recombination had not been included.

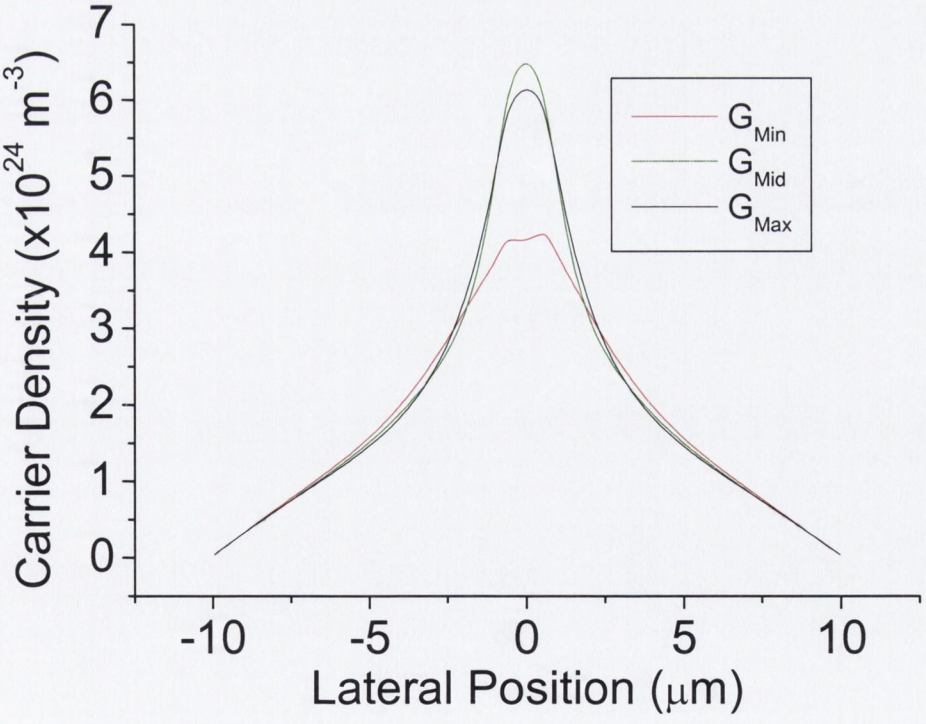


Figure 5-16 Lateral carrier density profile taken at the maximum and minimum modal gain point. G_{Mid} corresponds to the levelling off point at 1.8ns

The carrier density profile in figure 5-16 is taken at three times, corresponding to the minimum modal gain point at 1.51ns (G_{Min}), the levelling off point at 1.8ns (G_{Mid}) and the maximum modal gain point at 2.40ns (G_{Max}). The peak in the carrier density profile of those shown appears at 1.8ns due to the reduction in carrier density with stimulated emission at the modal gain peak. The corresponding modal gain profiles show that the absorption regions saturates around 1.8ns. The G_{Min} point occurs after the emission of the previous pulse. The modal absorption is now much less due to the photo-generated carrier increase in this region. As was outlined for within the 780nm device, the variation of the lateral field is indispensable to the creation of self-pulsation within these lateral absorber type devices. The full-width half-maximum of the lateral electric field varies by as much as 0.7um over the period of a pulse as seen in figure 5-18.

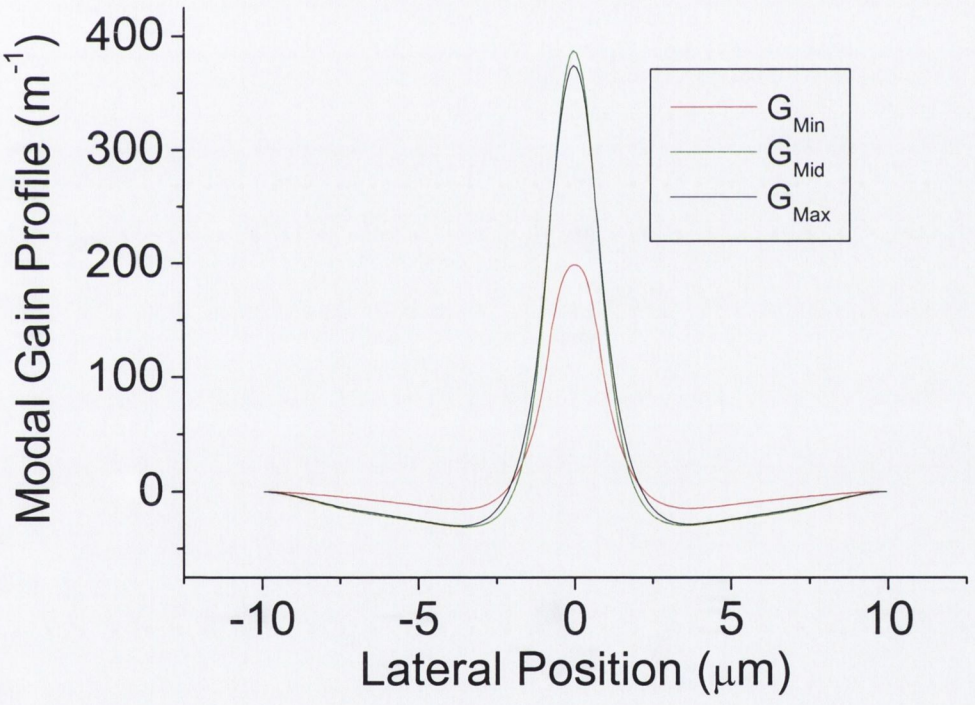


Figure 5-17 The lateral Modal gain profile illustrating the saturation of the modal absorption for the G_{Mid} profile at 1.8ns.

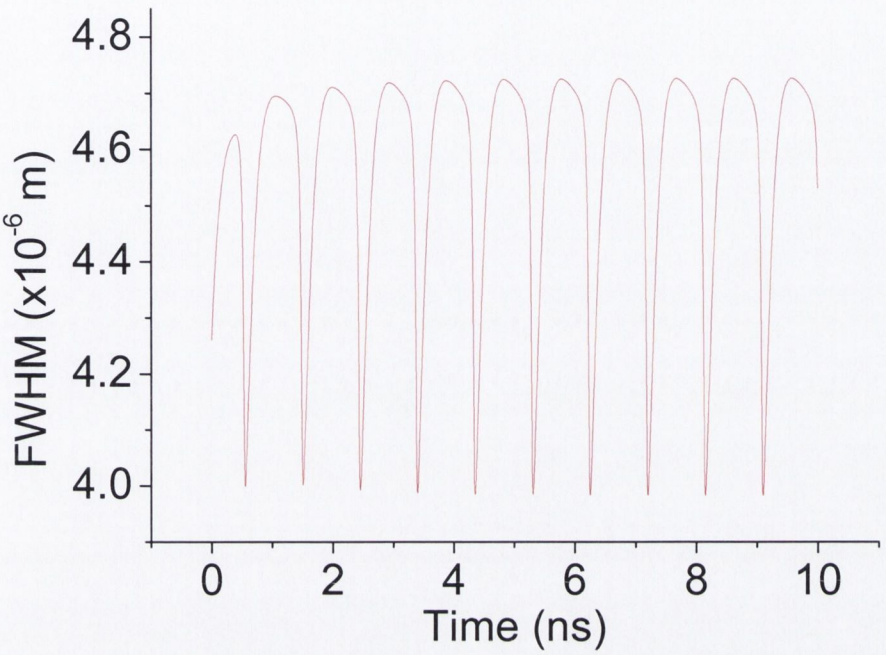


Figure 5-18 The full-width half-maximum variation (FWHM) of the lateral electric field.

In conclusion, we have demonstrated for the first time that self-pulsation can be achieved at a wavelength of 1.55μm with an optimised structure composed of three 5.5nm $In_{0.532}Ga_{0.468}As$ quantum wells lattice matched to InP with a bandgap wavelength of 1.55μm. The barriers were composed of 20nm wide $In_{0.735}Ga_{0.265}As_{0.575}P_{0.425}$ with a band gap wavelength of λ_g = 1.3μm. This has been possible due to the creation of lateral absorption regions within the active layer. An optimised device design has been presented that takes into account the important effects of intervalence band absorption and Auger recombination. The two-dimensional optical waveguide as well as the active region structure has been designed to provide the maximum confinement while meeting the constraints of a lower transparency carrier density imposed by Auger recombination. Further improvements in the device design will be discussed in the future work section.

References

1 "Very-high-speed optical signal processing", S Shimada, K Nakagawa, S Masatoshi and T Matsumoto, IEEE Proc, **81,** (11), p 1633, 1993.

2 "All-optical clock recovery from a 5GB/s RZ data signal using a self-pulsating 1.56μm laser diode", P Barnsley, G Wickens, H Wickes and D Spirit, IEEE Photon. Technol. Lett, **3,** p 942, 1991.

3 "All-optical timing and extraction with frequency division using a twin section laser diode", G. Farrell, P. Phelan, J. Hegarty, and J.Shields, IEEE Photon. Technol. Lett, **5,** p 718, 1993.

4 "A theoretical Analysis of Optical Clock Extraction Using a Self-Pulsating Laser Diode", P Rees, P McEvoy, A Valle, J O'Gorman, S Lynch, P Landais, L Pesquera and J Hegarty, IEEE J.Quant.Electron **35,** (2), 1999.

5 "Application of a 80 GHz all-optical clock in a 160km transmission experiment", C Bornholdt, J Slovak, M Mohrle and B Sartorious, OFC IEEE/Lasers & Electro-Opt. Soc. America. March 2002.

6 "Detuned Grating Multisection-RW-DFB Lasers for High-Speed Optical Signal Processing", M Mohrle, B Sartorius, C Bornholdt, S Bauer, O Brox, A Sigmund, R Steingruber, M Radziunas and H-J Wunsche. IEEE J.Sel.Topic.Quant.Electron. **7,** (2), 2001.

7 "Self-Pulsation in Multielectrode Distributed Feedback Lasers", G. H. Duan, and P Landais, IEEE Photon. Tech. Lett. **7,** (3), p 1041, 1995.

8 "Self-Sustained Pulsation Appearance in InGaAs/InP DH Lasers during Accelerated Operation" M Fukuda, K Wakita and G Iwane, Jpn.J.Appl.Phys **20,** (2), 1981.

9 "Self-Sustained pulsations in GaInAsP diode lasers", J Walpole, T Lind, J Hsieh and A Foyt. Appl. Phys. Lett **36,** (4), p240, 1980.

10 "800 Mb/s microwave FSK using a self-pulsation compact-disk laser diode", J Georges, K Lau. IEEE Photon.Technol. Lett, **3**, p 662, 1992.

11 "450 Mb/s BPSK and 1Gb/s QPSK throughput subcarrier multiple-access networks using 790nm self-pulsating laser transmitter network for computer applications", R Bates and S Walker, Electron. Lett, **27,** (12), p 1014, 1991.

12 "Linewidth enhancement factor of lattice matched InGaNAs/GaAs quantum wells", W Seo, J Donegan, Appl. Phys. Lett, **82,** (4), p 505, 2003.

13 " Vertical-Cavity Surface-Emitting Lasers, Design, Fabrication, Characterization, and Applications", C Wilmsen, H Temkin, L Coldren, Cambridge University Press 1999.

14 "The Carrier-Induced Index Change in AlGaAs and 1.3μm InGaAsP Diode Lasers", J Manning, R Olshansky, C B Su, IEEE J. Quant. Electronics, **19,** (10), 1983.

15 "Quantum Well Lasers", P Zory, Academic Press 1993.

16 "Effect of Auger recombination and differential gain on the temperature sensitivity of 1.5μm quantum well lasers", Y Zou, J Osinski, P Grodzinski, P Dapkus, W Rideout, W Sharfin, F Crawford, Appl. Phys. Lett. **62,** (2), p 175, 1993.

17 "Monolithically Integrated Dual-Wavelength Self-Sustained Pulsating Laser Diodes with Real Refractive Index Guided Self-Aligned Structure", T Onishi, O Imafuji, T Fukuhisa, A Mochida, Y Kobayashi, M Yuri, K Itoh and H Shimizu, Jpn.J.Appl.Phys. **40,** p 6401, 2001.

18 "Stable operation of self-sustained pulsation in 650-nm-band AlGaInP visible lasers with highly doped saturable absorbing layer", I Kidoguchi, H Adachi, T Fukuhisa, M Mannoh, and A Takamori, Appl.Phys.Lett, **68,** (25), p 3543, 1996.

19 "Doping Level and Type of GaInP Saturable Absorbing Layers for Realizing Pulsating 650-nm-Band AlGaInP Laser Diodes", T Onishi, H Adachi, I Kidoguchi, M Mannoh, A Takamori, Y Narukawa, Y Kawakami, and Shigeo Fujita, IEEE Photon.tech.lett. **10,** (10), p1368, 1998.

20 "Threshold current analysis of Compressive Strain (0-1.8%) in Low-Threshold, Long-Wavelength Quantum well Lasers", J Osinski, P Grodzinski, Y Zou, and P Dapkus, IEEE. J. Quant. Electron. **29,** (6), p 1576, 1993.

21 "Analysis and application of theoretical gain curves to the design of multi-quantum-well lasers", P McIlroy, A Kurobe, and Y Uematseu, IEEE. J. Quant. Electron. **21,** (12), p 1958, 1985.

22 "Landolt-Bornstein Numerical Data and Functional Relationships in Science and Technology, New Series, Group III-V, **22a**" Springer, Berlin, 1986.

23 "Auger Recombination in bulk and quantum well InGaAs" S Hausser, G Fuchs, A Hangleiter, and K Streubel, Appl.Phys.Lett. **56,** (10), p913, 1990.

Chapter 6 Conclusions

6.1 General Overview

The main focus of this thesis has been concerned with the carrier density dependent spatial and temporal modifications of the self-pulsation laser waveguide and their effects on the self-pulsation behaviour. Some of the earliest attempts to model the dynamics of self-pulsation for narrow stripe semiconductor were based on coupling three rate equations. We have shown that for the requirements of device design, it is necessary to have knowledge of the spatial distributions of some of the key parameters such as carrier density, gain and effective index. The use of such a model has allowed the understanding of the relevant spatial effects that a three section lumped model cannot provide. The accurate determination of threshold current through the inclusion of the effects of current spreading and diffusion was possible. Some of the earlier held assumptions that the appearance of self-pulsation was solely due to saturable absorption as a result of the photo-generation of carriers in the absorption regions are shown to be quantitatively inaccurate. By calculating the optical field and confinement factor over short time intervals throughout the evolution of the pulse, the effects of variations in the optical field were examined.

The fundamental limitations of the use of the effective index method for weakly guided waveguides were presented. Although the saturable absorption regions were created as a direct result of the failure of the effective index method, the mechanism of self-pulsation and its enhancement with the contribution of self-focussing and defocusing is still valid. The use of the effective index method was an important first step, in that it allowed one to identify the degree to which the structure was weakly guided. It also provided a criterion for measurement of the lateral effective index step and the variation with aluminium mole fraction within the blocking layer material. Within the effective refractive index framework it was possible through the calculation of the full width half maximum (FWHM) of the lateral field, to show that by keeping the field fixed at its threshold value throughout the simulation would result in relaxation oscillation behaviour. This key result shows that the variation of

the FWHM was crucial to achieving self-pulsation from the model in this type of structure.

The breakdown of the effective index method for weakly complex index guided structures prompted the development of various numerical techniques for the solution of the Helmholtz equation. Initially expansion methods using various basis functions were attempted based on the Galerkin formalism. There was a need to balance a numerical method that could provide an accurate representation of the weakly guided two-dimensional field while at the same time providing computationally efficient solutions that were capable of delivering the results in a reasonable time period. The development came on two fronts. Firstly the waveguide was solved accurately using a non-uniform finite difference grid availing of the symmetry of the waveguide. Secondly, the resulting non-hermitian sparse matrix was solved through collaboration with Heidi Thornquist, of Sandia National Laboratories Albaquerque, using a method based on the implicitly restarted Arnoldi method. The accurate determination of the optical modes was shown through the agreement of the modal gain determination based on the imaginary component of the longitudinal propagation constant and its determination as the sum of product of the material gain and confinement factor in each lateral section. Incorporating this method into the existing model offered a more robust solution of the self-pulsation dynamics. It provided the basis for a transition from a model that was accurate close to threshold current, to one in which the current could be varied to the point where insight into the effects of the cessation self-pulsation could be gained. It was found that with increasing current, the overall contribution of the spontaneous emission between pulses becomes significant and with the increasing self-pulsation frequency, the time given to depopulate the absorber sections had decreased. This resulted in a reduction in the FWHM of the lateral field profile and a reduction in the modal gain variation. Both mechanisms present probable causes for the transition between self-pulsation and continuous wave (CW) emission at high currents (>80mA in this case).

The success of the model in determining the mechanisms of self-pulsation within the AlGaAs/GaAs material system and to produce results in agreement with experiment was essential before the transition could be made to a new material system. The motivating factors for a self-pulsation laser emitting at the commercially important

1.55μm were threefold. There is the potential for optical clock extraction and clock distribution by the synchronisation of a self-pulsating laser diode. Benefiting from the fact that the self-pulsation laser has a low relative intensity noise on feedback negates the need for optical isolators, thereby reducing the cost in short distance fiber communication. Another possible application is the use of self-pulsation laser diodes as fast-tuneable ($\leq 1ns$) frequency-shift keyed (FSK) microwave subcarrier transmitters. The advantage of this scheme is that complex and costly electrical superposition circuitry is no longer required to provide the microwave subcarrier. But in order to progress toward these goals it was first necessary to design a laser that would incorporate the effects of Auger recombination and inter-valence band absorption within this wide bandgap material system. Since the differential index is larger in the InGaAsP system it was found that an effective index step of $6x10^{-3}$ was required to overcome this effect. This meant that provided the lateral waveguide was chosen to be wide enough to ensure the decay of the field towards the lateral boundaries, the effective index method provided an accurate solution of the lateral field.

InP was chosen as the blocking layer material for two reasons. Firstly the refractive index contrast between InGaAsP and InP is much lower than for the case of AlGaAs and GaAs substrate. Choosing InP as the blocking layer provided the largest index contrast between the cladding layer and the blocking layer. This meant that a higher effective index step was possible. Secondly since InP is transparent to the light emitted at the lasing wavelength, there was no optical loss in this region allowing the field to spread out in the lateral direction. As the intervalence band absorption scales with the confinement factor it was necessary to consider this in the choice of the optimum number of quantum well. Through the analysis of the transverse waveguide for various numbers of quantum well it was found that the lateral field variation with carrier density increased with quantum well number. In choosing the optimum number of quantum wells a compromise between the low transparency, high differential gain, offered by the single quantum well and the increased confinement offered through the use of multi-quantum wells was required. The triple quantum well met these. The thickness of the separate confinement heterostructure layer was varied until maximum overlap of the optical field with the quantum wells was achieved. To

our knowledge this represents the first theoretical evidence of the achievement of self-pulsation at 1.5μm for narrow stripe complex refractive index guided lasers.

6.2 Future Work

As we have mentioned in chapter 2 the introduction of strain into the active layer of the multi-quantum wells can enhance the operating performance of laser diodes considerably. We have shown in chapter 5 that the effect of including the Auger recombination effects with its cubic dependence on the carrier density has the effect of increasing the threshold and hence the operating carrier density of the device. It was demonstrated in [1] that Auger recombination can account for up to 80% of the threshold current in 1.55μm lasers. In order to compensate for the effect of the intervalence band absorption (IVBA) loss, it was found necessary to increase the length of the device thereby reducing the mirror loss term. The use of a compressively strained multi-quantum well could reduce both these effects considerably.

In the case of IVBA, it was reported in [2] that there was a considerable reduction in the IVBA coefficient $\frac{d\alpha}{dN}$, from a value of $1.4\text{x}10^{-20}$ m^2 for unstrained multi-quantum well to $3.5\text{x}10^{-21}$ m^2 for strained multi-quantum well structures. This in turn results in a fourfold reduction in IVBA contribution to the modal loss. The reduction in Auger coefficient within the carrier density range $1.0\text{x}10^{24} < N < 1.5\text{x}10^{24}$, was found experimentally [3] to vary from $4.15\text{x}10^{-41}$ $s^{-1}m^6$ to $2.58\text{x}10^{-41}$ $s^{-1}m^6$ for quantum well widths of 70 and 85 Angstroms respectively. It should be noted that for our particular case with a smaller well width, the Auger coefficient should be lower as explained in section 5.7. The introduction of strain effects into future designs would have the effect of reducing the modal loss through the reduction in the IVBA. This would allow the device length to be shortened increasing the self-pulsation frequency. By lowering the Auger coefficient, the operating carrier density and the threshold current can both be reduced. This allows the possibility for possible improvement in the current operating self-pulsating range of the laser. Comparing the calculated material gain for the compressed structure with the unstrained case in figure 6-1 we can see that the transparency carrier density is higher in the case of the strained quantum well. The

transparency value for the latticed matched triple quantum well is $2.8x10^{24}$ m^{-3} and is $3.5x10^{24}$ m^{-3} in the compressively strained case. Although the transparency carrier density is higher for the compressively strained structure the contribution to non-radiative recombination is reduced by the lower Auger coefficient for strained structures. The operating carrier density profile is therefore not expected to increase but to show a decrease for a properly optimised structure.

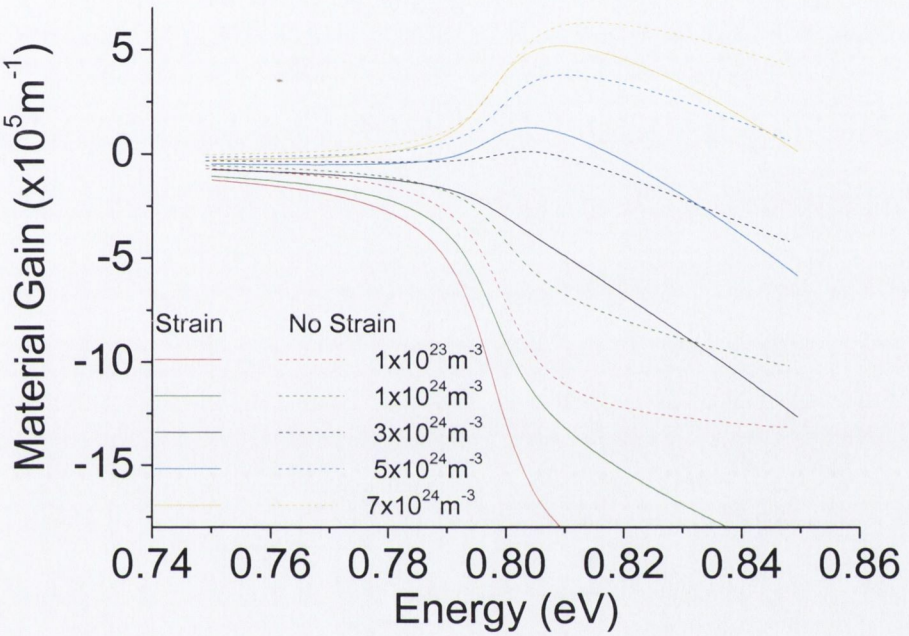


Figure 6-1 Calculated material gain profiles for 0.33 % compressively strained triple quantum well structures (solid line) and for the lattice matched case (dashed Line) for Carrier densities in the range of $1x10^{23}m^{-3}$ to $7x10^{24}m^{-3}$.

There will still be situations where the need for a full two-dimensional analysis of the field will be needed, for instance, at high current levels where the effective index step is reduced. This would also provide a means of comparison of the two methods identifying the regime in which the computationally more efficient, effective index approximation is applicable.

Through the incorporation of strain into the laser design and the comparison of the effective index approach with the two-dimensional calculations it is our intention to

design a 1.55μm self-pulsating laser that will then be manufactured and characterised. Experimental findings can be utilised to further improve the laser design.

References

1 "The Temperature Dependence of 1.3- and 1.5 μm Compressively Strained InGaAs(P) MQW Semiconductor Lasers", A Phillips, S Sweeney, A Adams, and P Thijs, IEEE J. Select. Topics Quantum Electron. **5,** (3), p 401, 1999.

2 "Intervalance band absorption coefficient measurements in bulk multi-quantum well 1.55μm semiconductor lasers", I. Joindot, and J. L. Beylat, Electron. Lett. **29,** (7), p 604, 1993.

3 "Experimental Study of Auger Recombination, Gain, and Temperature Sensitivity of 1.5μm Compressively Strained Semiconductor Lasers", Y. Zou, J. S. Osinski, P. Grodzinski, P. D. Dapkus, W. C. Rideout, W. F. Sharfin, J. Schlafer, and F.D. Crawford, IEEE J. Quant. Electron. **29,** (6), p 1565, 1993.